Design and Characterization of Silicon Photonic Devices for Data-Center Optical Interconnects

Deng Mao

Department of Electrical & Computer Engineering
McGill University
Montreal, Canada

October 2022

A thesis submitted to McGill University in partial fulfillment of the requirements for the degree of Doctor of Philosophy.

Abstract

The past decade has witnessed the prosperity of online communication and commercial activities, including video streaming services, cloud-based storage and services, and machine-to-machine applications. The exponentially increased internet traffic drives the development of high-speed and low-cost intra- and inter-data center optical interconnects (DCIs). Integrated optical transceivers have been realized on different platforms, including indium phosphide and lithium niobate. Compared to those platforms, the Silicon Photonic (SiP) platform is advantageous in complementary metal-oxide-semiconductor compatibility, reduced cost, optoelectronics integration, and high integration density. SiP, using the mature microelectronics fabrication process, enables high precision, high yield, and low-cost volume manufacture and simplifies the monolithic integration of both optical and electronic devices. Also, because of the physical properties of silicon, the dimension of the waveguide could be reduced to a micro-meter level, decreasing the footprint of optical devices and increasing the integration density.

In this thesis, we explore SiP devices for optical DCIs. This thesis can be divided into three parts. In the first part, we demonstrate the design and characterization of optical adiabatic couplers (OACs). The analytical relationship between splitting ratios (SRs) and waveguide properties is developed. Experiments demonstrate OACs with SRs from 7%/93% to 50%/50% for the fundamental transverse electric (TE) mode from 1260 to 1360 nm. The variances of SRs for different wavelengths across the Original band (O-band) are within 1.3% when the chip temperature increases from 20 °C to 50 °C. To further decrease the footprint of OACs and the SR variance from 1500 nm to 1600 nm, we propose a time-efficient method to analyze and design the OACs. The measured SRs of the targeted 3-dB OAC are between 47%/53% from 1500 nm - 1600 nm with a mode-evolution region of 110 µm. The same mode-evolution method presents imbalanced OACs with SRs from 8%/92% to 42%/58%.

The second part of the thesis presents a CMOS-compatible and temperature insensitive 1×4 wavelength (de-)multiplexer covering the entire Conventional band (C-band), partial Short-wavelength band (S-band) and Long-wavelength band (L-band). The (de-)multiplexer design is based on cascaded Mach-Zehnder interferometers (MZIs). The waveguide widths of the MZI delay lines are matched to decrease the overall thermo-optic coefficient (TOC). The proposed device is measured from 20 °C to 50 °C, and the measured

TOC is 4.8 pm/°C.

The last part of the thesis demonstrates the design, analysis, and characterization of a compact Mach-Zehnder modulator (MMZM) with meandered phase shifters on the SiP platform. With a footprint of 432×260 μm^2, the MMZM has an insertion loss of 2.1 dB. Using −0.5 V bias, the measured V_π and 3-dB EO BW are 6.4 V and 7.7 GHz, respectively. Using the fabricated MMZM, we experimentally demonstrate 53 Gbaud PAM-4 transmission over 2 km of standard single-mode optical fiber at a bit error rate (BER) below the hard-decision (HD) forward error correction BER threshold of 3.8×10^{-3} having 6.7% overhead.

Résumé

Cette dernière décennie a amenée la prospérité des communications en ligne et des activités commerciales, y compris les services de streaming vidéo, le stockage et les services basés sur le cloud et les applications de machine à machine. L'augmentation exponentielle du trafic Internet entraîne le développement d'interconnexions optiques au sein et entre les centres de données (DCI) à haute vitesse et à faible coût. Des émetteurs-récepteurs optiques intégrés ont été réalisés sur différentes plates-formes, notamment le phosphure d'indium et le niobate de lithium. Comparée à ces plates-formes, la plate-forme de photonique sur silicium (SiP) présente des avantages en termes de compatibilité complémentaire métal-oxyde-semi-conducteur, de coût réduit, d'intégration optoélectronique et de densité d'intégration élevée. SiP permet une fabrication en volume de haute précision, à haut rendement et à faible coût et simplifie l'intégration monolithique des dispositifs optiques et électroniques grâce à l'utilisation du processus de fabrication de la microélectronique mature. De plus, en raison des propriétés physiques du silicium, la dimension du guide d'ondes pourrait être réduite à un niveau micrométrique, diminuant l'encombrement des dispositifs optiques et augmentant la densité d'intégration.

Dans cette thèse, nous explorons les dispositifs SiP pour les DCI optiques. Cette thèse peut être divisée en trois parties. Dans la première partie, nous démontrons la conception et la caractérisation des coupleurs optiques adiabatiques (OACs). La relation analytique entre les rapports de séparation (SR) et les propriétés des guides d'ondes est développée. Des OAC avec des SR de 7%/93% à 50%/50% sont démontrés de 1260 à 1360 nm pour le mode électrique transversal fondamental (TE) par des expérimentations. Les variances des SR pour différentes longueurs d'onde sur la bande original (bande O) sont inférieures à 1,3% lorsque la température de la puce passe de 20 °C à 50 °C. Pour réduire davantage l'empreinte des OAC et la variance SR de 1500 nm à 1600 nm, nous proposons une méthode efficace pour analyser et concevoir les OAC. Les SR mesurés des OAC de 3 dB se situent entre 47%/53% de 1 500 nm à 1 600 nm avec une région d'évolution de mode de 110 um. La même méthode d'évolution de mode présente des OAC déséquilibrés avec des SR de 8%/92% à 42%/58%.

La deuxième partie de la thèse présente un 1×4 (dé-)multiplexeur de longueur d'ondes compatible avec CMOS et insensible à la température température couvrant complètement la bande conventionnelle (bande C), partiellement la bande de longueur d'onde courte (bande S) et longue (bande L) . La conception du (dé-) multiplexeur est basée sur des interféromètres Mach-Zehnder (MZI) en cascade. Les largeurs des guides d'ondes des lignes à retard MZI sont assorties pour diminuer le coefficient thermo-optique global (TOC). L'appareil proposé est mesuré de 20 °C à 50 °C, et le TOC mesuré est de 4,8 pm/°C.

La dernière partie de la thèse démontre la conception, l'analyse et la caractérisation d'un modulateur Mach-Zehnder compact (MMZM) avec des déphaseurs méandrés sur la plateforme SiP. Le MMZM a une perte d'insertion de 2,1 dB avec une empreinte de 432×260 μm^2. En utilisant un biais de $-0,5$ V, les V_π et 3-dB EO BW mesurés sont respectivement de 6,4 V et 7,7 GHz. À l'aide du MMZM fabriqué, nous démontrons expérimentalement une transmission PAM-4 de 53 Gbauds sur 2 km de fibre optique monomode standard à un taux d'erreur sur les bits (BER) inférieur au seuil de BER de décision finale (HD) de 3,8 $\times 10^{-3}$ ayant une surcharge de 6,7 %.

Acknowledgments

First, I would like to express my sincere gratitude to my supervisor, Professor David V. Plant. I am incredibly fortunate to have met a fabulous supervisor who is very good at guiding students through the confusing and challenging Ph.D. career. Dave is always generous with his time to support us unconditionally. His encouragement, patience, enthusiasm, and immense knowledge have guided me through the research and thesis preparation. We received a lab training course during my first year at McGill University. To this day, I still vividly remember Dave telling us that it is a privilege to work in this world-class lab. During my Ph.D. journey, I have always remembered his words by heart and cherished every moment I spent in the lab. It was only later that I slowly came to understand this statement. The equipment, fabrication opportunities, and industrial collaborations are only available to a handful of research groups and even the industry worldwide. Thank you, Dave, for your time and effort in getting us the best equipment and creating the best working environment. It is a great honour to be Dave's student.

I would like to express my deep respect and appreciation to my committee members: Professor Lawrence Chen and Professor Ioannis Psaromiligkos. I took the photonics devices and applications course and random process course from Professor Chen and Professor Psaromiligkos. The enthusiasm and knowledge they demonstrate during the classes impact me profoundly. Both lectures laid a solid foundation for my Ph.D. career. I am also grateful for the time Professor Chen and Professor Psaromiligkos spent on my qualification exam, proposal, and seminar.

I would like to thank my supervisor from undergraduate studies, Professor Songnian Fu. He accepted me in his lab during my first year in college when I had no idea what research was but was full of curiosity. I have accumulated tremendous research experience from Professor Fu and his research group. His patience with students, devotion to science, and knowledge in optics fiber communication has impacted me profoundly. I would not have started my Ph.D. study without his guidance and support. I appreciate that he accepted me as his student nine years ago.

I would like to express my profound gratitude to our industrial collaborators for the projects and opportunities they gave me. I would like to thank the valuable layout suggestions that researchers from CMC Microsystems gave us: Dan Deptuck, Jessica Zhang, Susan Xu, Neng Liu, and Luhua Xu. I would like to thank the engineers from Ciena for their insightful suggestions and discussions: Mahdi Parvizi, Ahmad Abdo, and Naim Ben-Hamida. I would like to thank professors and researchers from the University of British Columbia for their guidance and support: Professor Lukas Chrostowski, Professor Sudip Shekhar, Mustafa Hammood, and Alex Tofini. I would also like to thank Ping-Chiek Koh from Lumentum for his constructive suggestions.

I would like to express my appreciation to my dear friend, my lovely colleague, Md Samiul Alam, with whom I worked throughout my Ph.D. I still remember when I first entered the lab, Sami greeted me with a warm smile and made me feel welcome in the new environment. I consider myself extremely lucky to be his friend and colleague. I appreciate the enormous time he spent training me in the lab. I will never forget the depressing time we spent in the lab when every simple thing went wrong. Even though things never go as smoothly as we expected, we can always cheer each other up and make fun of the situation. To quote from one of my favourite novels, *Harry Potter*, "Happiness can be found in the darkest times if one only remembers to turn on the light." I wish Sami all the luck in the world for his bright future.

Also, I would like to thank my mentor, colleague, and friend, Oscar Yun Wang. Oscar is the person who introduced the world of Silicon Photonics to me. Oscar has laid a solid foundation for my Ph.D. career by sharing with me the priceless layout, simulation, and experiment experience. Furthermore, he has spent enormous time helping me revise my manuscripts. I appreciate Oscar's knowledge and the industrial opportunity he presented to me. I consider it a great honour to have the chance to be his colleague again shortly.

I would like to thank my colleague Eslam El-Fiky for his helpful discussions. He has been very patient with lots of my questions and helped me edit my manuscripts. I would like to thank David Patel, Maxime Jacques, Yannick D'Mello, Luhua Xu, and Alireza Samani for their constructive suggestion and discussions. Furthermore, I would like to express my gratitude to Adam Helmy, Santiago Bernal, Amar Kumar, and Jinsong Zhang for the delight they brought in the challenging experimental process. I would also like to thank all the people that helped me along the journey: Reza Maram, Abdelkader Zerfaine, Meng Xiang, Zhenping Xing, Md Ghulam Saber, Minh Thang Hoang, Fangyuan Zhang, Olivier Carpentier, Siddiqui Hakim, Ka Wai Michael Hui, Rui Li, Weijia Li, Zixian Wei, and Yixiang Hu.

I would like to express my profound appreciation and respect for my family. I miss my grandfather every day since he left us this February, and I wish he could have witnessed my graduation. I will never forget the life lessons and the unconditional love he showed me. I would like to thank my grandmother, Yian Zhang, my father, Jun Mao, and my mother, Lin Deng, for the optimism, encouragement, perseverance, and devotion they demonstrated during the best and worst times. My parents brought me up as an independent, strong, diligent, and caring person. I hope I have not failed their expectation. I would like to thank Hong Deng for his in-person and virtual company over the past eight years. Our relationship always reminds me of the book *Love in Time of Cholera*. Life is full of changes. No matter what arrangement life has for us, I appreciate the memory we share.

Associated Publications

This thesis represents my original research, and it has not been submitted for a degree or diploma at any other institution. The original contributions presented in this thesis are based on the following six first-authored publications: four journal articles [1–4] and two conference papers [5, 6]. In addition, I also have one first-authored conference proceeding that is not directly reflected in this thesis [7]. Through the collaboration with my colleagues in the Photonic Systems Groups at McGill University and other industrial researchers, I have co-authored seven journal papers [8–14] and three conference proceedings [15–17].

Journal Articles Directly Related to This Thesis

1. **D. Mao**, M. S. Alam, M. Parvizi, E. El-Fiky, A. Abdo, N. Ben-Hamida, and D. V. Plant, "Design, Analysis, and Characterization of A Compact Silicon Photonics Modulator with Meandered Phase Shifters," *Optics Express*, **30**(18), pp. 32990-33002, 2022.

   I conceived the idea, performed the device design and simulations, conducted the experiment, and wrote the paper. The co-authors contributed in building the experimental setup and revising the manuscript.

2. **D. Mao**, Y. Wang, L. Xu, J. Zhang, E. El-Fiky, M. S. Alam, Y. D'Mello, S. Lessard, and D. V. Plant, "CMOS-Compatible and Temperature Insensitive C-band Wavelength (De-)Multiplexer," *IEEE Photonics Technology Letters*, **34**(14), pp. 769-772, 2022.

   I conceived the idea, performed the device design and simulations, conducted the experiment, and wrote the paper. The co-authors contributed in building the experimental setup and revising the manuscript.

3. **D. Mao**, Y. Wang, L. Xu, E. El-Fiky, M. Jacques, J. Zhang, M. S. Alam, A. Kumar, Y. D'Mello, and D. V. Plant, "Adiabatic Coupler with Nonlinearly Tapered Mode-Evolution Region," *IEEE Photonics Technology Letters*, **33**(16), pp. 840-843, 2021.

   I conceived the idea, performed the device design and simulations, conducted the experiment, and wrote the paper. The co-authors contributed in building the experimental setup and revising the manuscript.

4. **D. Mao**, Y. Wang, E. El-Fiky, L. Xu, A. Kumar, M. Jacques, A. Samani, O. Carpentier, S. Bernal, M.S. Alam, J. Zhang, M. Zhu, P.-C. Koh, and D. V. Plant, "Adiabatic coupler with design-intended splitting ratio," *Journal of Lightwave Technology*, **37**(24), pp. 6147-6155, 2019.

   I discussed the idea with Yun Wang. I performed the device design and simulations, conducted the experiment, and wrote the paper. The co-authors contributed in discussing the idea, building the experimental setup, and revising the manuscript.

Conference Articles Directly Related to This Thesis

5. **D. Mao**, M. S. Alam, M. Parvizi, E. El-Fiky, A. Abdo, N. Ben-Hamida, and D. V. Plant, "Compact Silicon Photonics Meandered Mach-Zehnder Modulator," in *Conference on Lasers and Electro-Optics*, San Jose, CA, USA, SF4M-3, 2022.

   I conceived the idea, performed the device design and simulations, conducted the experiment, and wrote the paper. The co-authors contributed in building the experimental setup and revising the manuscript.

6. **D. Mao**, Y. Wang, L. Xu, E. El-Fiky, M. Jacques, J. Zhang, Y. D'Mello, S. Lessard, and D. V. Plant, "Nonlinearly Tapered 3-dB Adiabatic Coupler," in *IEEE Photonics Conference*, pp. 1-2, 2020.

   I conceived the idea, performed the device design and simulations, conducted the experiment, and wrote the paper. The co-authors contributed in building the experimental setup and revising the manuscript.

Journal Articles Not Directly Related to This Thesis

7. J. Zhang, L. Xu, **D. Mao**, Z. Xing, Y. D'Mello, M. Jacques, Y. Wang, S. Lessard, and D. V. Plant, "High-Extinction-Ration and Compact 1310/1550 nm Wavelength Diplexer on SOI Platform Based on an SWG-Structured Two-Mode Interference Coupler," *IEEE Photonics Journal* **14**(2), pp. 1-6, 2022.

8. J. Zhang, L. Xu, **D. Mao**, Y. D'Mello, W. Li, S. Lessard, and D. V. Plant, "All-silicon multi-band TM-pass polarizer on a 220 nm SOI enabled by multiplexing grating regimes," *Optics Express* **30**(1), pp. 326-335, 2022.

9. M. G. Saber, L. Xu, R. H. Sagor, Y. Wang, A. Kumar, **D. Mao**, E. El-Fiky, D. Patel, A. Samani, Z. Xing, M. Jacques, Y. D'Mello, and D. V. Plant, "Integrated polarization handling devices," *IET Optoelectronics*, **14**(3), pp. 109-119, 2020.

10. L. Xu, Y. Wang, **D. Mao**, J. Zhang, Z. Xing, E. El-Fiky, M. Saber, A. Kumar, Y. D'Mello, M. Jacques, and D. V. Plant, "Ultra-broadband and compact two-mode multiplexer based on subwavelength-grating-slot-assisted adiabatic coupler for the silicon-on-insulator platform," *Journal of Lightwave Technology*, **37**(23), pp. 5790-5800, 2019.

11. L. Xu, Y. Wang, **D. Mao**, E. El-Fiky, Z. Xing, A. Kumar, M. Saber, M. Jacques, and D. V. Plant, "Broadband 1310/1550 nm wavelength demultiplexer based on a multimode interference coupler with tapered internal photonic crystal for the silicon-on-insulator platform," *Optics Letters*, **44**(7), pp. 1770-1773, 2019.

12. L. Xu, Y. Wang, E. El-Fiky, **D. Mao**, A. Kumar, Z. Xing, M. G. Saber, M. Jacques, and D. V. Plant, "Compact broadband polarization beam splitter based on multimode interference coupler with internal photonic crystal for the SOI platform," *Journal of Lightwave Technology*, **37**(4), pp. 1231-1240, 2019.

13. L. Xu, Y. Wang, A. Kumar, E. El-Fiky, **D. Mao**, H. Tamazin, M. Jacques, Z. Xing, M. G. Saber, and D. V. Plant, "Compact high-performance adiabatic 3-dB coupler enabled by subwavelength grating slot in the silicon-on-insulator platform," *Optics Express*, **26**(23), pp. 29873-29885, 2018.

Conference Proceedings Not Directly Related to This Thesis

14. **D. Mao**, M. Parvizi, M. S. Alam, A. Abdo, N. Ben-Hamida, E. El-Fiky, and D. V. Plant, "Electrode Design for Slow-Light based Mach-Zehnder Modulator in Silicon Photonics," in *Advanced Photonics Congress*, IW1B-4, 2021.

15. L. Xu, **D. Mao**, J. Zhang, Y. Wang, Z. Xing, M. S. Alam, M. Jacques, Y. D'Mello, S. Bernal, and D. V. Plant, "Broadband Polarization Beam Splitters Based on MMI Couplers with Internal Photonic Crystals Fabricated Using 193 nm Photolithography," in *Optical Fiber Communications Conference and Exhibition*, pp. 1-3, 2021.

16. M. S. Alam, A. Abdo, **D. Mao**, M. Parvizi, N. Ben-Hamida, and D. V. Plant, “Timing Phase Recovery in Digital Multi-Subcarrier Coherent Optical Communication,” in *Photonics North*, pp. 1-1, 2021.

17. L. Xu, Y. Wang, **D. Mao**, J. Zhang, M. S. Alam, Z. Xing, M. Jacques, Y. D’Mello, S. Bernal, S. Lessard, and D. V. Plant, “Broadband 2×2 Adiabatic 3-dB Coupler with Inversely-Tapered Mode-Evolution Region for the Silicon-on-Insulator Platform,” in *IEEE Photonics Conference*, pp. 1-2, 2020.

Contents

List of Figures

List of Tables

List of Acronyms

ADC	Analog-to-Digital Converter
ADS	Advanced Design System
AMF	Advanced Micro Foundry
AWG	Arrayed-Waveguide Grating
BG	Bragg Grating
BPD	Balanced Photodetector
BW	Bandwidth
B2B	Back-to-Back
C-band	Conventional Band (1530 - 1565 nm)
CMOS	Complementary Metal-Oxide-Semiconductor
CPS	Coplanar Strip
CVQKD	Constant Variable Quantum Key Distribution
CWDM	Coarse Wavelength-Division Multiplexing
DAC	Digital-to-Analog Converter
DC	Direct Current
D-C	Data Center
DCI	Data Center Interconnect
DSP	Digital-signal-processing
DVQKD	Discrete Variable Quantum Key Distribution
DWDM	Dense Wavelength-Division Multiplexing
EDFA	Erbium-Doped Fiber Amplifier
EME	Eigenmode Expansion
EO	Electro-Optic
ER	Extinction Ration

FAU	Fiber Array Unit
FDE	Finite Difference Eigenmode
FDTD	Finite-Difference-Time-Domain
FEC	Forward Error Correction
FIR	Finite-Impulse-Response
FOM	Figure-of-Merit
FPR	Free Propagation Region
FSR	Free-Spectral Range
GC	Grating Coupler
GSa/s	GSamples/s
HD	Hard-Decision
HFSS	High-Frequency Structure Simulator
IL	Insertion Loss
IoT	Internet of Things
IP	Internet Protocal
L-Band	Long-Wavelength Band
LCA	Lightwave Component Analyzer
MMI	Multimode Interference
MPW	Multi-Project-Wafer
MRM	Micro Ring Modulator
MRR	Micro-Ring Resonator
MUX	Multiplexer
MW	Microwave
MZI	Mach-Zehnder Interferometer
MZM	Mach-Zehnder Modulator
MMZM	Meandered Mach-Zehnder Modulator
OAC	Optical Adiabatic Coupler
O-band	Original Band (1260 - 1360 nm)
ODC	Optical Directional Coupler
OMA	Optical Modulation Amplitude
OOK	On-off Keying
PAM	Pulse-amplitude Modulation
P-C	Photonic Crystal

PD	Photo-detector
PDFA	Praseodymium-Doped Fiber Amplifier
PIC	Photonic Integrated Circuit
QAM	Quadrature Amplitude Modulation
Q-Factor	Quality-Factor
RC	Raised Cosine
RF	Radio Frequency
RTO	Real-Time Oscilloscope
S-Band	Short-wavelength Band
SiN	Silicon Nitride
SiP	Silicon Photonic
SOA	Semiconductor Optical Amplifier
SOI	Silicon-on-Insulator
SPP	Series-Push-Pull
SPS	Samples Per Symbol
SR	Splitting Ratio
SSMF	Standard Single Mode Fiber
SWG	Subwavelength Grating
TE	Transverse Electric
TEC	Thermoelectric Cooler
TIA	Trans-impedance Amplifier
TM	Transverse Magnetic
TOC	Thermo-Optic Coefficient
TW	Travelling-Wave
WDM	Wavelength-Division Multiplexing
XT	Crosstalk
2D	Two-Dimension
3D	Three-Dimension

Chapter 1

Introduction

1.1 Motivation

With the prosperity of online business, entertainment, and communications, including the internet of things (IoT), the 5G network, online gaming and video streaming platforms, and cloud-based applications, tremendous efforts are spent on improving the efficiency and transmission capacity of data centers (D-Cs). According to Cisco's estimation, by 2023, nearly two-thirds of the global population will have internet access, and the number of devices connected to internet protocol (IP) networks will be more than three times the global population [18]. For short-reach data center interconnects (DCIs), where many transceivers are deployed to enable high-speed, large-capacity transmission, cost per part, heat dissipation, and power consumption are also critical issues to be addressed [19]. Therefore, a low-cost and high-yield transmission solution with certain thermal controllability is in great demand.

For decades, many endeavours have been devoted to rearranging and reusing the modular process steps from complementary metal-oxide-semiconductor (CMOS) fabrication [20]. Therefore, well-established materials and techniques in the silicon microelectronics industry have been used to build complex photonic devices and circuits. By leveraging the billion-dollar modern CMOS infrastructures, the commercialization and mass-production of the photonic integrated circuits (PICs) on the silicon photonics (SiP) platform is feasible. Also, due to the large index contrast between the silicon core and its oxide cladding, photonic devices with high integration density are achieved on the SiP platform.

To enable high-speed and low-cost DCIs, researchers worldwide have been researching and demonstrating transceiver designs on the SiP platform [21–23]. A generic schematic of a transceiver with a wavelength (de-)multiplexer (MUX) is shown in Fig. 1.1. Because of the indirect bandgap of the silicon material, the integrated laser can not be realized directly on the SiP platform. Alternatively, externally modulated lasers can be connected to the rest of the PICs. Without considering the mode MUXs, transverse electric (TE) mode is ensured before interfacing with the edge couplers or vertical grating couplers (GCs). After information loading through the modulators, the modulated optical signals with different optical wavelengths are combined by a wavelength MUX. The merged optical signal is transmitted through standard single-mode fiber (SSMF). The optical signal is first separated by the wavelengths at the receiver end using a (de-)MUX. For each wavelength, the optical signal is translated into the electrical field by a photo-detector (PD) and amplified by a trans-impedance amplifier (TIA). The scope of this thesis is limited to the low-cost and low-power consumption transmitter design with high fabrication and temperature tolerance.

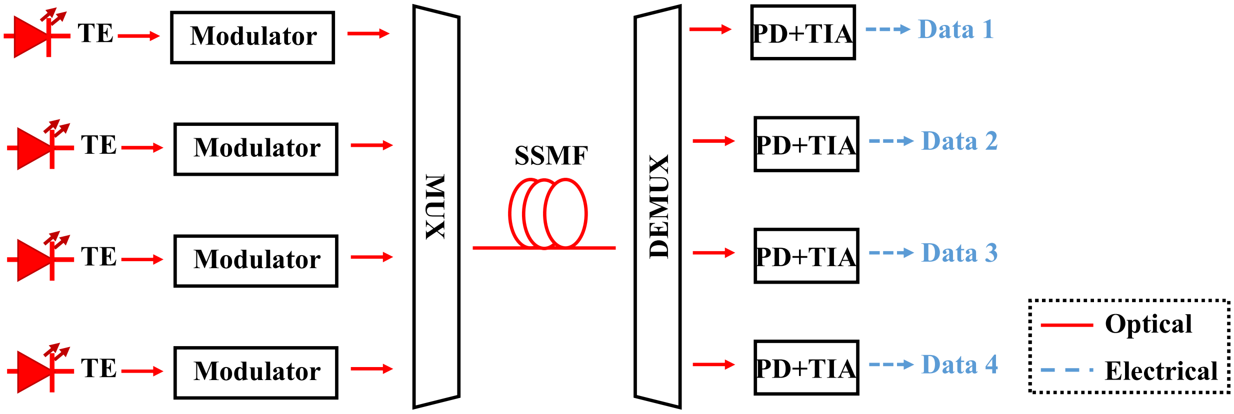

Fig. 1.1 Schematic of the transceiver design with wavelength (de-)multiplexers. TE: transverse electric, MUX: multiplexer, SSMF: standard single mode fiber, PD: photo-detector, TIA: transimpedance amplifier.

Power splitters, wavelength (de-)MUXs, and modulators are the three fundamental components of transmitter designs. Power splitters are frequently used to build Mach-Zehnder interferometers (MZIs), as shown in Fig. 1.2, which are widely used in optical switches [24], modulators [25], and integrated neural networks [26]. In those applications, imbalanced power splitters with specific splitting ratios (SRs) are often required. Imbalanced power splitters can be realized by mode interference couplers, including optical directional couplers (ODCs) and multimode interference (MMI) couplers for the silicon-on-insulator (SOI) platform [27–32]. However, the performance of those imbalanced couplers based on ODCs or MMI couplers needs precise control of the device dimensions. Also, for each SR, a new set of parameters must be determined to ensure a reproducible result that is tolerant to fabrication error. Compared to ODCs and MMI couplers, optical adiabatic couplers (OACs) involve only one mode [33]. The mode order stays the same through the adiabatic transition region even though the mode profiles at distinct locations are different. Thus, the OACs do not need precisely defined critical power transfer length. However, most research on OACs is focused on the ones with an SR of 3-dB, and imbalanced OACs are still open to being explored.

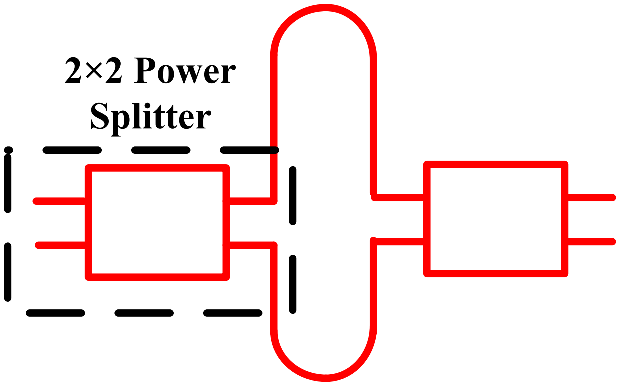

Fig. 1.2 Schematic of the Mach-Zehnder interferometer.

The major drawback of the OACs is the large footprint to achieve a flat SR over a broad optical bandwidth (BW). The length of an OAC can be up to 200 µm [34], dramatically deteriorating the simulation time and accuracy. Instead of using the straight waveguides in the mode evolution region, adopting subwavelength grating (SWG) slots can decrease the required mode-evolution region [14, 35]. However, SWG slots are sensitive to fabrication error, compromising the fabrication tolerance of the OACs. To further improve the performance of OACs, a time-efficient simulation method is worth exploring to optimize the constituent waveguides in the mode-evolution region without compromising the fabrication tolerance of the OACs.

Wavelength (de-)MUXs are frequently used to increase the transmission capacity in DCIs and optics communication networks [36]. SiP wavelength (de-)MUXs based on arrayed waveguide gratings (AWGs), ring resonators, and MZIs have been demonstrated over the past decades [37–41]. However, due to silicon waveguides' high thermo-optic coefficients (TOCs), their effective indices are sensitive to temperature variations. Therefore, the performance of SiP (de-)MUXs is temperature-dependent since their operational theories are based on phase interference which is directly related to effective indices. It is essential to address the thermal sensitivity issue.

SiP modulators are one of the enabling devices for optical communications, which requires optimization in two domains: higher BW and lower power consumption [42]. Modulators with large electro-optic (EO) BW, including travelling-wave (TW) Mach-Zehnder modulator (MZM) [25] and micro ring modulators (MRM) [43], have been reported to achieve high-capacity transmission. However, TWMZM and MRM are power-hungry because of the termination and wavelength stabilization circuitry, respectively. High integration density, slight optical loss, high thermal stability and fabrication tolerance drive the design of next-generation low-power SiP modulators. Some efforts have been made to develop lumped-element slow-light modulators with high modulation efficiency and small footprint, accompanied by shortcomings such as sensitivity to temperature variations and fabrication errors [44, 45]. Therefore, considering the above requirements, dual-drive meandered MZMs (MMZMs) have been proposed [46]. Still, there is room to simplify the driving and biasing circuitry while reducing the footprint further. Also, a systematic EO BW analysis for lumped modulators considering electrode, PN junction, and optical transit time is preferred.

In this thesis, we work on designing several significant components for low-cost and temperature-insensitive transceivers: the OACs, wavelength (de-)MUX, and modulator on the SOI platform. In the first part of the thesis, we present OACs with design-intended SRs. A time-efficient method is then proposed to analyze and further improve the performance of OACs. Then, a CMOS-compatible 1×4 Conventional band (C-band) wavelength (de-)MUX with low thermal sensitivity is demonstrated. Finally, a compact SiP MMZM with low optical loss and simplified driving and biasing circuitry is demonstrated.

1.2 Thesis organization

The remainder of this thesis is organized as follows.

In Chapter 2, we provide the research background for the SOI platform and the relevant photonic devices we designed for this platform. In Section 2.1, we introduce the basics of the SOI platform. Then, the research background of two types of power splitters are discussed in Section 2.2. Finally, the fundamentals of wavelength (de-)MUX and modulators are presented in Sections 2.3 and 2.4, respectively.

In Chapter 3, we report the operational theory, simulation, and characterization of the 2×2 OACs. In Section 3.1, we demonstrate OACs with design-intended SRs. In Section 3.2, we propose a time-efficient method to analyze and design the OACs on the SOI platform. Using this method, we demonstrate OACs with improved performance in terms of footprints and SRs.

In Chapter 4, we demonstrate a CMOS-compatible and temperature-insensitive C-band wavelength (de-)MUX on the SOI platform. Section 4.1 briefly introduce the structure of this chapter. Section 4.2 presents the detailed analysis and simulation results. Section 4.3 gives the fabrication and experimental results.

Chapter 5 focuses on designing, analyzing, and characterizing a compact SiP modulator with meandered phase shifters. The constitution of this Chapter is first introduced in Section 5.1. Section 5.2 introduces the device layout and simulation results. Then, the direct current (DC) and small-signal characterization are illustrated in Section 5.3. Finally, the results for the on-off keying (OOK) and different pulse-amplitude modulation (PAM) orders with basic digital-signal-processing (DSP) algorithms are displayed in Section 5.4.

Finally, Chapter 6 concludes the thesis by summarizing the key accomplishments and outlining some potential improvements and future work in the short and long terms.

1.3 Original contributions

In summary, the original contributions of this thesis are the analysis, simulation, and experimental characterization of three critical components of low-cost transmitter design: power splitters, wavelength (de-)MUXs, and modulators on the SOI platform. The contributions are summarized hereafter:

Temperature Insensitive Adiabatic Coupler Design with High Fabrication Error Tolerance

- First, we demonstrate the OACs with design-intended SRs for the SOI platform. The operational principle, numerical simulations, and experimental results on the designed

OACs are presented. To explain the operating principle, we derive the analytical relationship between the SR and the effective index difference, based on which we calculate the corresponding SRs under various output waveguide width differences at a central wavelength of 1310 nm. During the simulation process, a segmented optimization method is employed to analyze the adiabatic transition process through the OAC. For the experiment results, broadband OACs with design-intended SRs, from 7%/93% to 50%/50%, are fabricated and then tested over an optical BW of 100 nm, i.e. from 1260 to 1360 nm for the fundamental TE mode. Furthermore, the thermal stability of the OAC is investigated. When increasing the stage temperature from 20 °C to 50 °C, the variances of the SRs for different wavelengths across the O-band are within 1.3%, making the design a potential candidate for performance robustness against temperature variations.

- Then, we propose a time-efficient method to analyze and design the OACs on the SOI platform. By analyzing the OACs, we derive the boundary conditions and necessary constraints on the tapering functions to achieve optimized performance. Taking these conditions into consideration, we choose three common types of functions for comparison. Based on the width and separation of the constituent waveguide pair, the performance of OACs with different tapering functions is compared. The compared OACs are fabricated and measured. The SRs of the fabricated devices are characterized using unbalanced MZIs. We analytically and experimentally prove that, for a designed 3-dB OAC, a quadratic separation and exponentially varying width provides the slightest SR imbalance with the smallest footprint among the compared tapering methods. The extracted SRs of the designed 3-dB OAC using such a tapering method are between 47%/53% from 1500 nm to 1600 nm with a mode evolution length of 110 um. Using this tapering method, we also experimentally demonstrate imbalanced OACs with SRs of 8%/92%, 12%/88%, 15%/85%, 23%/77%, 30%/70%, and 42%/58% measured at 1550 nm.

CMOS-compatible and Temperature Insensitive C-band Wavelength (de-)Multiplexer

- We demonstrate a CMOS-compatible and temperature insensitive 1×4 C-band wavelength (de-)MUX on the 220-nm-thick SOI platform. The (de-)MUX design is based on cascading MZIs. The waveguide widths of the MZI delay lines are matched to decrease the overall thermo-optic coefficient (TOC). For comparison, an MZI-based (de-)MUX with uniform delay lines is also fabricated on the same chip. The transmission spectra of the proposed and reference devices are measured when the wavelength is swept from 1500 nm to 1600 nm, and the temperature is varied from 20 °C to 50 °C. The measured results show that the TOCs of the proposed and reference device are 4.8 pm/°C and 85 pm/°C, respectively. This power-efficient MUX with high integration density is promising for the D-C applications.

Compact Mach-Zehnder Modulator with Meandered Phase Shifter

- We present a C-band MZM with meandered phase shifters and a compact footprint of 432×260 μm^2 on the SOI platform. The electrode, p-n junction, and optical transit time are considered when performing the EO BW simulations. The simulation results prove that the dominant BW limiting factor for this type of modulator is the optical transit time. The insertion loss (IL) of the modulator without bias is 2.1 dB. The measured half-wave voltage (V_π) and 3-dB EO BW at -0.5 V bias are 6.4 V and 7.7 GHz, respectively. 53 Gbaud PAM-4 transmission over 2 km of SSMF is achieved at a bit error rate (BER) below the 6.7% overhead hard-decision (HD) forward error correction (FEC) BER threshold of 3.8×10^{-3}.

Chapter 2

Background

This Chapter introduces the background of the SiP platform and the devices discussed in this thesis. In Section 2.1, we briefly introduce the SOI platform and the critical properties of the silicon waveguide used in this platform. Section 2.2 presents the research background of the two power splitters: MMI couplers and OACs. Section 2.3 demonstrates the state-of-the-art (de-)MUXs and focuses on the development of temperature-insensitive designs. Section 2.4 introduces the fundamentals of SiP modulators.

2.1 Silicon photonic platform

The typical composition of the wafers used for SiP PICs is shown in the Fig. 2.1. It comprises a 220 nm silicon layer, a cladding oxide layer on top of the 220 nm silicon layer, a buried oxide layer underneath the 220 nm silicon layer, and a silicon substrate on the bottom. The 220 nm silicon layer is used to define photonic devices and has become a standard since 2003 [47]. However, silicon waveguides with different thicknesses have been reported for various applications [48]. A cladding layer is deposited on top of the 220 nm silicon layer to provide protection and isolation of the photonic devices. In addition, this top oxide layer can be removed to realize polarization manipulation devices [28]. A buried oxide layer enables tight light confinement and high integration density. The bottom silicon substrate serves as mechanical support.

To design photonic devices on the SOI platform in different wavelength ranges, the wavelength dependence of the refractive index for silicon is a critical consideration when performing simulations [20]. A Lorentz model is used for the silicon refractive index to en-

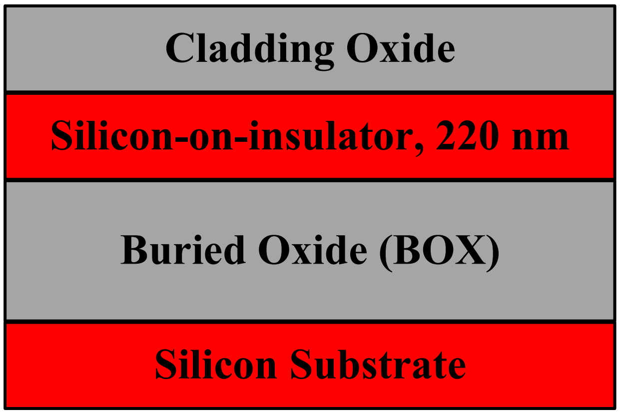

Fig. 2.1 Cross-section view of the silicon-on-insulator (SOI) wafer.

sure consistent simulation in Ansys Lumerical MODE and Finite-Difference-Time-Domain (FDTD) solvers [49]:

$$n_{\mathrm{Si}}^2(\lambda) = \epsilon + \frac{\epsilon_{\mathrm{Lorentz}}\omega_0^2}{\omega_0^2 - 2i\delta_0 2\pi c/\lambda - (\frac{2\pi c}{\lambda})^2} \tag{2.1}$$

where n_{Si} is the silicon refractive index, ϵ is the permittivity, $\epsilon_{\mathrm{Lorentz}}$ is Lorentz permittivity, ω_0 is the Lorentz resonance in units of rad/s, δ_0 is Lorentz linewidth in units of rad/s, λ is the wavelength, and c is the speed of light in vacuum.

A constant index model often models the refractive index of silicon dioxide. First, silicon dioxide has an almost constant refractive index around 1550 nm, and the material dispersion of silicon dioxide is about six times lower than in silicon [20]. In addition, most of the light is confined in the silicon layer, making the oxide dispersion insignificant in the performance of SiP devices. One exception is when the waveguide widths are intentionally small, and the evanescent fields are used for different applications, including sensing. Since light would be loosely confined in the silicon waveguide, the effect of dioxide should be considered for the accuracy of simulation results. For simulations performed for typical devices when the light is strongly confined in the waveguide, a constant index model for dioxide is preferred for fewer convergence issues and faster simulation time.

After choosing the appropriate models for both silicon and dioxide, the effective and group indices could be calculated. For SiP devices and system designs, the effective and group indices are frequently used to determine critical characteristics. The definitions of effective and group indices are briefly summarized in the following paragraphs.

From the perspective of wave optics, a necessary condition for a guided mode in a waveguide, as shown in Fig. 2.2, is $n_{\mathrm{SiO2}} < \frac{\beta}{k_0} < n_{\mathrm{Si}}$, where n_{SiO2} and n_{Si} are the refractive indices of silicon dioxide and silicon, respectively, β is the propagation coefficient, and k_0 is the vacuum wavevector. The effective index can be understood as the average index seen by the mode and can be calculated using the mode amplitude as the weighting function. Therefore, the effective index of a mode is defined as $n_{\mathrm{eff}} = \frac{\beta}{k_0}$ [50].

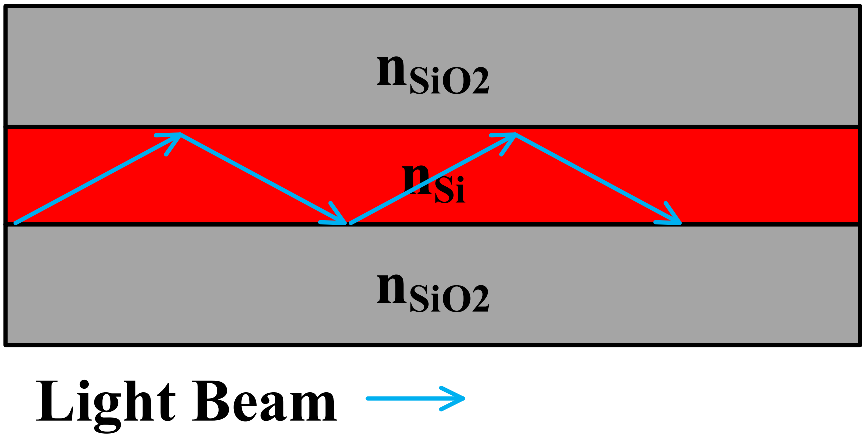

Fig. 2.2 Total internal reflection for a guided mode in a section of silicon waveguide.

To properly illustrate the definition of group index, we first introduce the definitions of phase velocity, group delay, and group velocity [50]. The phase term of the sinusoidal electromagnetic wave is expressed as $e^{-j(kz-wt)}$ traveling in the $\hat{z}$ direction, where k is the wavevector in certain material and ω is the angular frequency of the wave in units of rads/sec. A point is attached to this electromagnetic wave. The speed of this point has to satisfy the following condition so that its phase stays the same:

$$z(t) = \frac{\omega t}{k} + \text{constant} \tag{2.2}$$

Therefore, the phase velocity v_{p} is defined by taking the first-order derivative of Eqn. 2.2 with respect to the time t:

$$v_{\mathrm{p}} = \frac{dz}{dt} = \frac{\omega}{k} \tag{2.3}$$

Frequently, light travels as a package because the modulation of lightwave will unavoidably expand the frequency spectrum of the original carrier. The group velocity v_{g}

describes the propagation of this light package. We introduce a superposition of two waves with different frequencies to develop an expression for the group velocity: $\omega_1 = \omega + \Delta\omega$, $\omega_2 = \omega - \Delta\omega$, where ω_1 and ω_2 are the angular frequencies of the two waves, and $\Delta\omega$ is the frequency difference from central frequency ω. The electric field superposition can be written as follow:

$$E_1 + E_2 = 2E_0 \cos(\omega t - kz) \cos(\Delta\omega t - \Delta kz) \tag{2.4}$$

where E_1 and E_2 are the electric field of the two waves, E_0 are the amplitude of the two waves, and Δk are the wavevector difference of the two waves. The group velocity v_{g} describes the speed of the wave envelope, which is described by $\cos(\Delta\omega t - \Delta kz)$. Similarly, assuming that there is a point attached to the envelope, the speed of this point has to satisfy the following condition so that its phase stays the same:

$$z(t) = \frac{\Delta\omega t}{\Delta k} + \text{constant} \tag{2.5}$$

Therefore, the group velocity v_{g} is defined by taking the first-order derivative of Eqn. 2.5 with respect to time t:

$$v_{\mathrm{g}} = \frac{dz}{dt} = \frac{\Delta\omega}{\Delta k} = \lim_{\Delta\omega \to 0} \frac{\Delta\omega}{\Delta k} = \frac{d\omega}{dk} \tag{2.6}$$

Group delay τ_{g} is defined as the time it takes for a wave package to travel a unit distance. With the definition of v_{g}, τ_{g} can be expressed as follows:

$$\tau_{\mathrm{g}} = 1/v_{\mathrm{g}} = \frac{dk}{dw} \tag{2.7}$$

To relate Eqn. 2.7 to the effective index n_{eff}, $k = \frac{n_{\mathrm{eff}}\omega}{c}$ is substituted into Eqn. 2.7 and the group delay can be expressed as follows:

$$\tau_{\mathrm{g}} = \frac{\mathrm{d}(\frac{n_{\mathrm{eff}}\omega}{c})}{\mathrm{d}\omega} = \frac{n_{\mathrm{eff}} + \omega\frac{\mathrm{d}n_{\mathrm{eff}}}{\mathrm{d}\omega}}{c} \tag{2.8}$$

By inverting Eqn. 2.8, we acquire a new expression for v_{g}:

$$v_{\mathrm{g}} = \frac{c}{n_{\mathrm{eff}} + \omega\frac{dn_{\mathrm{eff}}}{d\omega}} \tag{2.9}$$

Therefore, the group index n_g is expressed as follows:

$$n_\mathrm{g} = n_\mathrm{eff} + \omega \frac{dn_\mathrm{eff}}{\omega} = n_\mathrm{eff} - \lambda \frac{dn_\mathrm{eff}}{d\omega} \tag{2.10}$$

With the introduction of effective and group indices, we perform simulations on the two commonly used waveguides for C-band and O-band using Ansys Lumerical MODE finite difference eigenmode (FDE) solver. Within the scope of this thesis, only the fundamental TE mode is considered. Therefore, the simulation results focus on the fundamental TE mode. The width of a strip waveguide with a standard height of 220 nm must be less than 440 nm to enable a single TE and transverse magnetic (TM) mode [20]. However, when injecting the fundamental TE mode from the laser to the fiber array unit (FAU) interfaced by on-chip vertical GCs, most of the light would still be coupled into the fundamental quasi-TE mode without exciting higher-order modes. In addition, another benefit of utilizing larger width is to reduce optical loss and phase noise. Most of the optical loss and phase noise come from the side-wall roughness. With a larger waveguide width, the optical mode would concentrate more in the central region of the waveguide and interface less with the side wall, reducing the propagation loss and phase noise. Therefore, the strip waveguide with a 500 nm width is adopted and simulated. The mode profile captured at 1550 nm is shown in Fig. 2.3(a). The calculated effective and group indices from 1500 nm to 1600 nm are shown in Fig. 2.3(b) and 2.3(c), respectively.

Similarly, the single TE mode operation requests the waveguide width to be less than 320 nm for O-band operation. Therefore, a waveguide width of 350 nm is used. The mode profile captured at 1300 nm is shown in Fig. 2.4(a). The calculated effective and group indices from 1260 nm to 1360 nm are shown in Fig. 2.4(b) and 2.4(c), respectively.

2.2 Power splitter

2.2.1 2×2 Multimode interference coupler

Recently, there has been a growing interest in employing the MMI effect in SiP devices. The MMI effect has been utilized to realize power splitters [51–59], optical hybrids which are frequently used in coherent receiver designs [60–68], and polarization beam splitters [69–73]. The theoretical analysis demonstrated in this Section is based on [74]. The fundamental principle of MMI couplers is the self-imaging principle. Some early explorations of utilizing the self-imaging principle on the uniform waveguide platform were demonstrated in [75,76].

The schematic of an MMI waveguide fabricated on the silicon layer is shown in Fig. 2.5. The width and length of the MMI waveguide are denoted as W_{MMI} and L_{MMI}, respectively. The guided mode is transmitted along the z-direction. The number of guided modes is finite for a given waveguide [50], and the total number of supported modes for the MMI waveguide is labeled as m. For the ν_{th}-order mode, the dispersion relationship between the lateral wavevector $k_{y,\nu} \approx \frac{(\nu+1)\pi}{W_{\mathrm{MMI}}}$ and propagation constant β_ν is expressed as follows:

$$k_{y,\nu}^2 + \beta_\nu^2 = k_0^2 n_{\mathrm{eff},\nu}^2 \tag{2.11}$$

where $n_{\mathrm{eff},\nu}$ is the effective index of the ν_{th}-order mode and k_0 is the the vacuum wavevector.

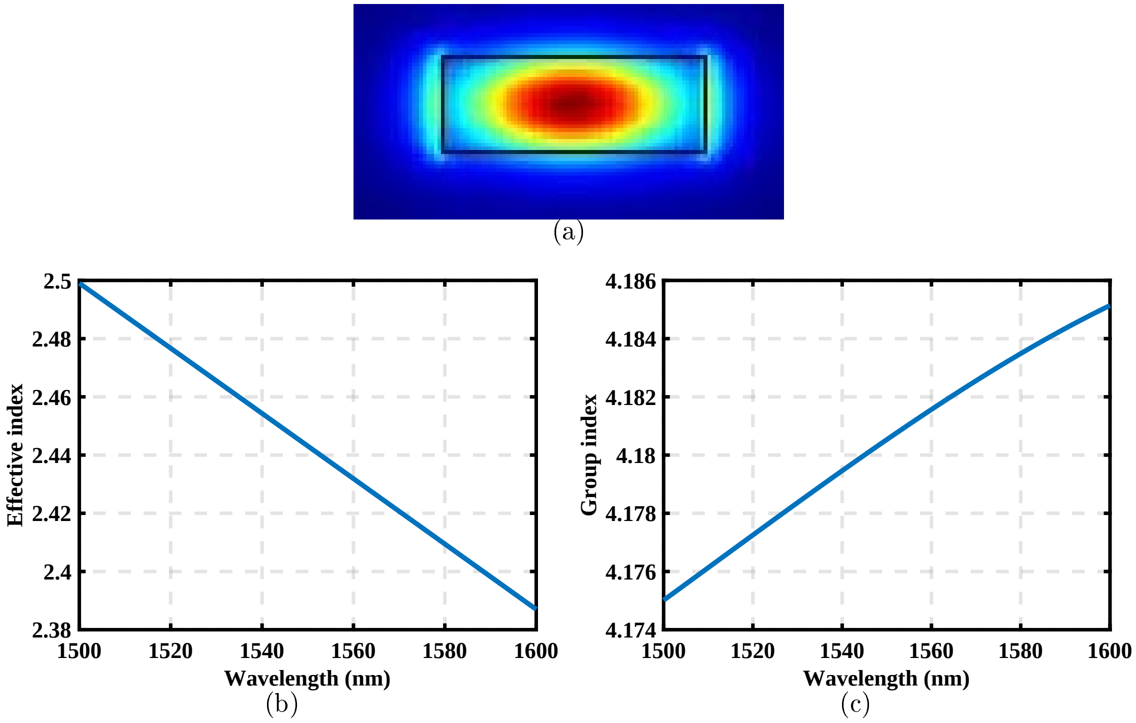

(a)

(b)

(c)

Fig. 2.3 (a) The mode profile, (b) effective index, and (c) group index of a waveguide with 220 nm height and 500 nm width.

The propagation constant can be expressed as follows from Eqn. 2.11:

$$\beta_\nu = k_0 n_{\text{eff},\nu} \sqrt{1 - (\frac{k_{y,\nu}}{k_0 n_{\text{eff},\nu}})^2} \tag{2.12}$$

For a real function $f(x)$ that is infinitely differentiable at a real number a, its Taylor series is the power series as expressed below:

$$f(x) = \sum_{n=0}^{\infty} \frac{f^{(n)}(a)}{n!}(x-a)^n \tag{2.13}$$

When $f(x) = \sqrt{1-x^2}$, its second-order Taylor series at $a = 0$ can be approximated as follow:

$$f(x) \approx 1 - \frac{x^2}{2} \tag{2.14}$$

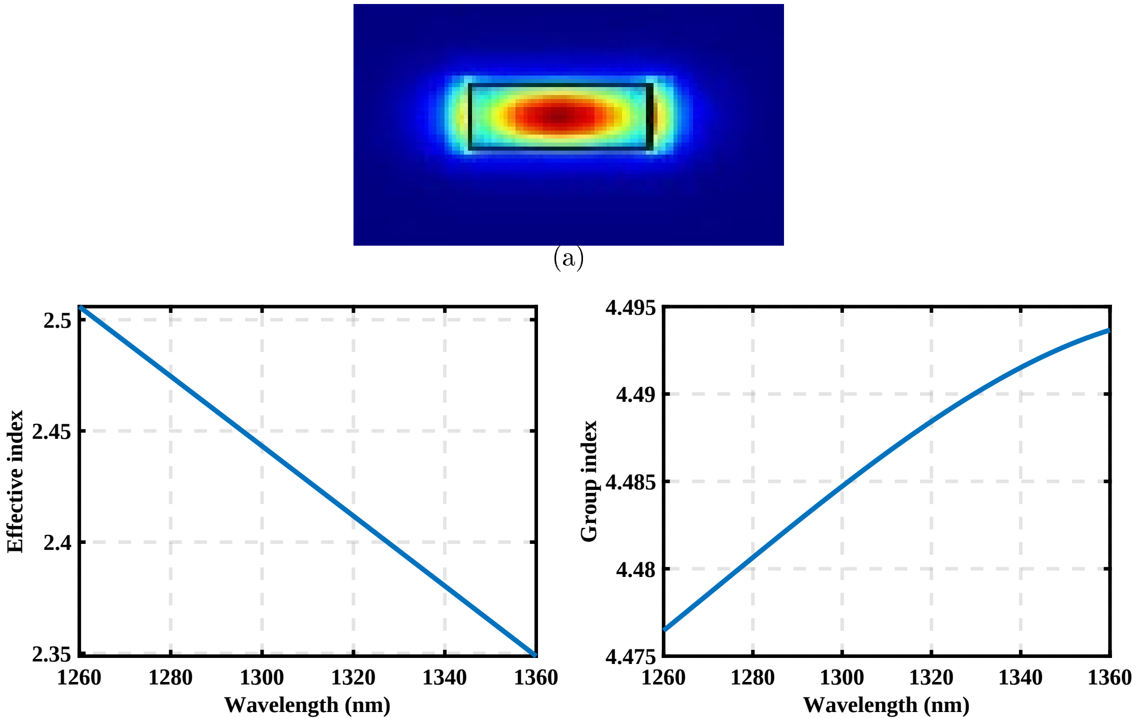

(a)

(b)

(c)

Fig. 2.4 (a) The mode profile, (b) effective index, and (c) group index of a waveguide with 220 nm height and 350 nm width.

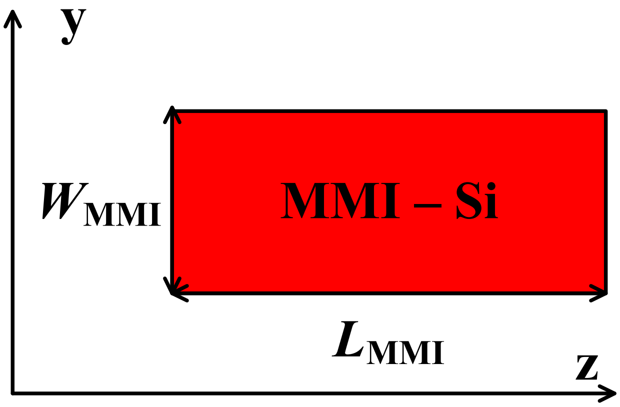

Fig. 2.5 Schematic of an MMI waveguide.

Therefore, when $x = \frac{k_{y,\nu}}{k_0 n_{\mathrm{eff},\nu}}$ and $k_{y,\nu} << k_0 n_{\mathrm{eff},\nu}$, the second Taylor approximation of Eqn. 2.12 is expressed as follows:

$$\beta_\nu \approx k_0 n_{\mathrm{eff},\nu} - \frac{k_0 n_{\mathrm{eff},\nu}}{2}\left(\frac{k_{y,\nu}}{k_0 n_{\mathrm{eff},\nu}}\right)^2 \tag{2.15}$$

When taking $k_0 = \frac{2\pi}{\lambda_0}$ and $k_{y,\nu} \approx \frac{(\nu+1)\pi}{W_{\mathrm{MMI}}}$ into Eqn. 2.15, β_ν can be simplified as follows:

$$\beta_\nu \approx k_0 n_{\mathrm{eff},\nu} - \frac{(\nu+1)^2 \pi \lambda_0}{4 n_{\mathrm{eff},\nu} W_{\mathrm{MMI}}^2} \tag{2.16}$$

The beat length L_π is defined by the propagation constants of the two lowest-order modes. Using Eqn. 2.16, L_π can be expressed as follow:

$$L_\pi = \frac{\pi}{\beta_0 - \beta_1} \approx \frac{4 n_{\mathrm{eff},\nu} W_{\mathrm{MMI}}^2}{3\lambda_0} \tag{2.17}$$

The input field profile $\Psi(y,0)$ at $z = 0$ can be expressed in terms the superposition of the guided modes:

$$\Psi(y,0) = \sum_{\nu=0}^{\nu=m-1} c_\nu \psi_\nu(y) \tag{2.18}$$

where c_ν is the coefficient for the ν-th order mode.

At $z = L$, the field profile is expressed as follows:

$$\Psi(y, L) = \sum_{\nu=0}^{\nu=m-1} c_\nu \psi_\nu(y) \exp\left[j\frac{\nu(\nu+2)\pi}{3L_\pi}L\right] \tag{2.19}$$

For the case of general interference when no restriction is placed on c_ν, Eqn. 2.19 can be expressed in terms of a two-fold imaging at $L = \frac{p}{2}(3L_\pi)$, $p = 1, 3, 5...$:

$$\begin{aligned}\Psi(y, \frac{p}{2}3L_\pi) &= \sum_{\nu \text{ even}} c_\nu \psi_\nu(y) + \sum_{\nu \text{ odd}} (-j)^p c_\nu \psi_\nu(y) \\ &= \frac{1+(-1)^p}{2}\Psi(y,0) + \frac{1-(-1)^p}{2}\Psi(-y,0)\end{aligned} \tag{2.20}$$

For the case of restricted interference when only some of the guided modes are excited in the MMI waveguide, the input field should be excited at $y = \pm W_{\text{MMI}}/6$, and two-fold images will be formed at $L = \frac{p}{2}L_\pi$, p is non-negative integer.

2.2.2 2×2 Adiabatic coupler

The idea of adiabatic transition used in the PICs is defined in [33]. This idea has been exploited intensively on the SOI platform to implement different devices, including power splitters [34, 35, 77–85], polarization manipulating devices [86–96], and mode MUXs [97–104].

The focus of this thesis is on developing the OACs with improved performances. The operating theory of OACs involves only one mode, and the mode order stays the same through the adiabatic transition region even though the mode profiles at distinct locations are different. Therefore, OACs do not need precisely defined critical power transfer lengths. The detailed simulation process and operational theories will be presented in Section 3. The following paragraphs will present the research background and the state-of-the-art results regarding OACs.

The main reason that prohibited a vast deployment of OACs on the integrated platform is the large footprint of such devices. The footprint of some early fabricated OACs can be up to several mm^2. In the past two decades, much effort has gone into developing OACs with smaller footprint. Instead of the 90° waveguide bends, researchers have used the adiabatic S-shaped waveguide bends between the input(output) ports and the mode-evolution region to reduce the device width [35, 77, 84]. On the other hand, the main priority is to decrease the required mode-evolution length to shrink the device length, which can be achieved by increasing the coupling strength in the mode-evolution region. Researchers adopt SWG slots [14, 83] or rib waveguides [78, 84] to increase the coupling strength. However, the dimensions of SWG slots are close to the minimum feature size of almost all the available foundry processes. Therefore, SWG-based OACs are sensitive to fabrication errors. Another method is to optimize the shape of the coupling region. Researchers calculated the required coupling length based on different fitting functions of the coupling coefficients and propagation constants [84, 105, 106].

Above all, the imbalanced OACs are still open to be explored and will be discussed in Section 3.1. Also, the effects of width and gap change on the adiabaticity of the devices remain to be analyzed quantitively and will be presented in Section 3.2.

2.3 Wavelength multiplexing technology

Wavelength-division-multiplexing (WDM) technology is one of the popular solutions to enhance the transmission capacity of an optical interconnect link [36]. The key parameters to evaluate the performance for a wavelength (de-)MUX are shown in Fig. 2.6: channel spacings/free-spectral ranges (FSRs), ILs, crosstalks (XTs), and 1-dB BW [107]. Channel spacings are determined by the number of channels and the FSRs of the filters. Channel spacing is measured by the wavelength difference of the neighbouring channels when the maximums are achieved. IL is the optical transmission loss captured at the maximum point of each channel. At the maximum of each channel, the minimum transmission spectrum difference between the channel of interest and the neighbouring channels is defined as XT. For each channel, if we draw a horizontal line 1 dB below the maximum point, there will be at least two crossings on this channel. The 1-dB BW is the minimum spacing between the crossings on different sides of the maximum point.

Different structures are utilized in the SOI platform to realize wavelength (de-)MUXs, including micro-ring resonators (MRRs) [108–114], Bragg gratings (BG) waveguide [115–121], arrayed-waveguide gratings (AWGs) [122–127], and MZIs [39,40,128–132]. The advantages and disadvantages of each type of (de-)MUXs are introduced concerning the critical parameters, as shown in Fig. 2.6.

The benefit of the MRR-based wavelength (de-)MUXs is the capability of incorporating

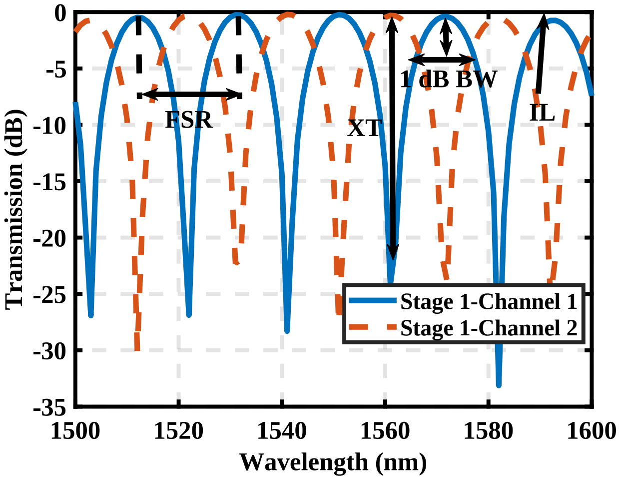

Fig. 2.6 The key parameters used to evaluate the performance of a (de-)MUX.

multiple channels in a compact footprint. However, the number of channels is limited by the tight FSR. The FSR of MRR is determined by the cavity length, which is limited by the bending radius. The minimum bending radius is as small as several microns in the standard SOI platform without introducing significant optical losses. Nevertheless, by utilizing a specially designed silicon waveguide, a record FSR is achieved for the MRR [114]. Another disadvantage of the MRR-based wavelength (de-)MUXs is the small channel BW because of the Lorentzian-like spectral response of MRR [107]. Researchers have presented cascaded high-order MRRs [133], a combined add-drop ring with a reflector [134], and MRR with photonic crystal (P-C) [135] to realize flat-top responses. Because of the tight BW of such MUX, the performance is also susceptible to temperature changes.

BGs in SiP are created by periodically corrugating the silicon waveguides to create the effective index modulation. The benefits of BG-based (de-)MUXs are the flat-top response, the flexible wavelength selectivity, and the large FSR. The corrugation depth controls the BW of the response. The periodicity of the BGs defines the center wavelength. In principle, the FSR of BG is infinite. The disadvantages of BG-based (de-)MUXs are the footprints and the ILs. Since multiple channels are often required to realize a wavelength (de-)MUX, several BGs must be cascaded to form a multi-channel filter, which increases the overall footprint. The ILs per channel are inherent with the BGs and are determined by the corrugation depth and the number of periods used in the gratings. Therefore, there is a trade-off between BW, footprint, and IL. Traditional BG has only two ports: input and output ports. To avoid the circulators in the devices, researchers have proposed several solutions to separate the reflected light from the injected light: the combination of MMI waveguides and BGs [115, 136], grating-assisted contra-directional couplers [117, 137], and multimode waveguide gratings [118, 119].

(De-)MUXs based on AWGs are typically composed of two free propagation regions (FPRs) and several arrayed waveguides connecting the FPRs. The most attractive benefit of AWGs is the capability of multiplexing tens of WDM channels simultaneously. Therefore, these devices have been adopted in practical dense WDM (DWDM) applications. Even though the SiP platform is capable of decreasing the footprint of AWGs from several cm^2 to around 0.1 cm^2, the integration density of such devices is still expected to be improved further. Also, the XTs within each channel could be decreased with a smaller footprint, given that the phase noises are introduced by the uneven silicon waveguide thickness and side-wall roughness. There are multiple ways to reduce the footprint of AWGs including overlapping the FPR regions [138], and using the P-Cs [126, 139] or BGs [140] at the end of arrayed waveguides as a reflective structure. Nevertheless, the ILs of such devices can be up to 10 dB, even for the AWGs fabricated on the low-loss silicon nitride (SiN) platform [141, 142].

Wavelength (de-)MUXs based on MZIs are typically composed of several stages. For each stage, one or more MZIs are cascaded. The elemental composition of MZI includes power splitters, power combiners, and delay paths. To demonstrate the filtering principle of the cascaded MZIs, we present a 1×4 wavelength (de-)MUX composed of three stages, as shown in Fig. 2.7. We use MMI couplers based on general interference, as introduced in Section 2.2.1, for the power splitters. Ansys Lumerical eigenmode expansion (EME) solver calculates the S-parameters of the MMI couplers. The following equation determines the delay path of each MZI [143]:

$$FSR = \frac{\lambda^2}{n_\mathrm{g}\Delta L} \tag{2.21}$$

where n_g and ΔL are the group index and length of the delay path, respectively. Section 4.2 presents the detailed calculation process, and we demonstrate the results only in this Section. The transmission spectrum for each stage is shown in Fig. 2.8. For Stage 1, the simulated FSR is 20 nm, and the output is separated into even and odd channels. For Stage 2A/2B, the simulated FSR is 40 nm, and the even/odd channels are filtered again.

Therefore, a wavelength (de-)MUX of 10 nm channel spacing is formed.

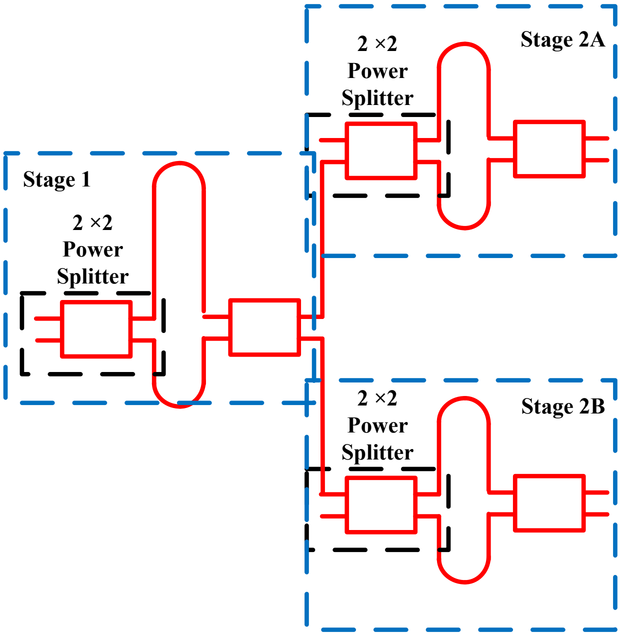

Fig. 2.7 The schematic of a MZI-based 1×4 wavelength (de-)MUX.

From the simple example shown above, the channel spacing of MZI-based wavelength (de-)MUX is determined by the number of stages and the FSR of each stage. Regardless of the footprint, such a scheme can realize a WDM design with random channel spacing. The power splitters' performance determines each channel's IL and XT. Also, the phase noise introduced by the delay path would influence the XTs. By cascading multiple MZIs for each stage, a flat-top response, therefore higher BW, is achieved for each channel [39].

Due to silicon waveguides' high TOCs, the effective and group indices are sensitive to temperature variations. Since the operational theories of the MZI-based (de-)MUXs are based on phase interference, which is directly related to the effective and group indices, the performance of such devices is temperature-dependent. Thus, it is essential to address the thermal sensitivity issue. Recently, researchers have proposed utilizing a material with a negative TOC on top of the silicon waveguide to counteract the positive TOC at the cost of compromising the CMOS compatibility [144]. The MUX fabricated on the SiN platform has low thermal sensitivity, but a larger footprint has also been demonstrated [145]. The active feedback loop is also applied to increase the thermal stability, which is effective but increases the power consumption and integration complexity [146]. Another method is to use a combination of waveguides with different TOCs to force the overall TOCs of the multiplexers to be zeros. Since the TOCs of waveguides are related to effective indices, the difference in TOCs is created using waveguides with different widths, modes, or polarizations [147–151]. However, additional ILs are introduced when light is coupled to the higher-order modes or different polarizations. In addition, directional couplers, whose performances are sensitive to temperature variations, are adopted in most MZI-based athermal MUXs. Therefore, by using a power splitter with lower thermal sensitivity, the overall TOC of the MUX could be further reduced.

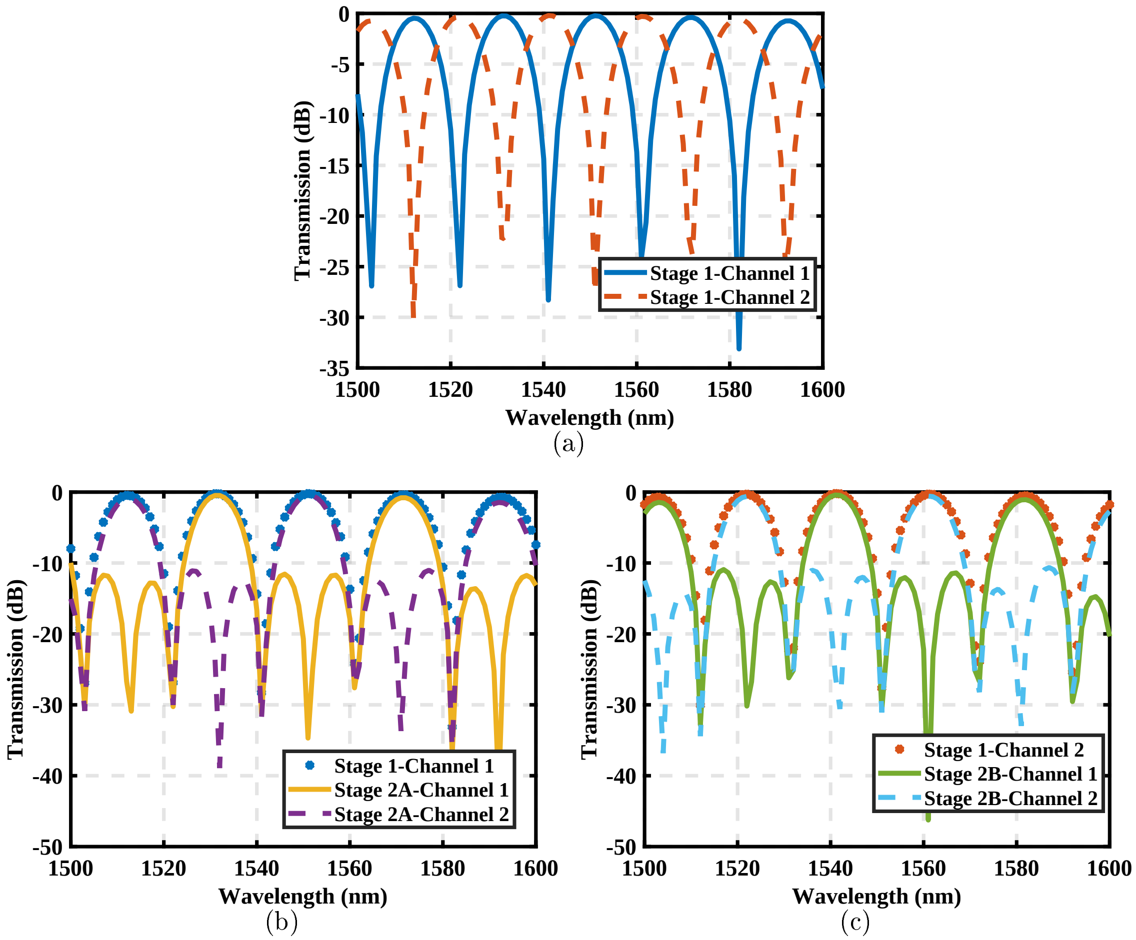

(a)

(b)

(c)

Fig. 2.8 Transmission spectra of (a) Stage 1, (b) Stage 2A, and (c) Stage 2B.

2.4 Modulator

Soref and Bennett first predicted the plasma dispersion effect in 1987, which has been widely used as the phase modulation principle on the SOI platform [152]. The phase change occurs when the carriers are injected or removed from the p-n junction. The changes in index of refraction at 1550 nm and 1310 nm can be expressed as follows according to the recent experimental data [153]:

$$\Delta n(\text{at} \quad 1550 \text{ nm}) = -5.4 \times 10^{-22} \Delta N^{1.011} - 1.53 \times 10^{-18} \Delta P^{0.838} \tag{2.22a}$$

$$\Delta n(\text{at} \quad 1310 \text{ nm}) = -2.98 \times 10^{-22} \Delta N^{1.016} - 1.25 \times 10^{-18} \Delta P^{0.835} \tag{2.22b}$$

The changes in absorption at 1550 nm and 1310 nm as functions of carrier densities are as follows:

$$\Delta \alpha(\text{at} \quad 1550 \text{ nm}) = 8.88 \times 10^{-21} \Delta N^{1.167} + 5.84 \times 10^{-20} \Delta P^{1.109} \tag{2.23a}$$

$$\Delta \alpha(\text{at} \quad 1310 \text{ nm}) = 3.48 \times 10^{-22} \Delta N^{1.229} + 1.02 \times 10^{-19} \Delta P^{1.089} \tag{2.23b}$$

where ΔN and ΔP are the carrier densities of electrons and holes in units of cm^{-3}.

For high-speed modulators, the reverse-biased p-n junction has been widely adopted. Under reverse bias, the motion of the free carriers is caused by the applied electric field, also called drift. As a comparison, under forward bias, the movement of free carriers is caused by the concentration difference, also called carrier diffusion. The drift velocity is much faster than the diffusion velocity [154]. Therefore, utilizing a reverse-biased p-n junction for a high-speed modulator seems intuitive. However, a significant drawback of the reverse-biased p-n junction is that a high voltage of up to 15 V is required to achieve a π phase shift, which is not acceptable to most CMOS radio frequency (RF) drivers [155]. Compared to the reverse-biased p-n junction, the forward-biased p-i-n junction is more efficient in phase modulation [156]. Using a passive RC equalizing technique, researchers have extended the EO BW of a modulator with a forward-biased p-i-n junction to 20 GHz [157, 158]. However, this technique would require different fabrication processes, which are difficult to access for academia. Therefore, this thesis focuses on developing the SiP modulators with the reverse-biased p-n junction.

Different types of modulators have been presented on the SOI platform, including

TWMZMs [16, 25, 159–169], MRMs [170–180], BG-based modulators [45, 181–191], P-Cs-based modulators [44], and MMZMs [46, 192, 193]. We will compare the critical metrics of different types of devices, including the EO BWs, the driving voltages, the power consumption, the optical BWs and temperature sensitivity, the footprints, and the optical ILs [160]. For monolithic integration of the CMOS RF driver on the SiP transceivers, the driving voltages are expected to be below 2.5 V [194]. The power consumption of modulators mainly comes from three aspects: 1) The RF driving voltage, termination, and capacitance of the p-n junction; 2) The biasing circuitry when thermal phase shifters are employed to tune the phases; 3) The temperature control circuitry when the devices are susceptible to thermal variations [193]. The optical operational BWs determine the thermal sensitivity of modulators. The footprints of devices are relevant to integration density, especially for transceivers using WDM techniques [170]. The optical ILs determine the receiver sensitivity, the highest transmission speed for error-free operation, and the adoption of optical amplifiers, including Erbium-Doped fiber amplifiers (EDFAs), Praseodymium-Doped fiber amplifiers (PDFAs), and semiconductor optical amplifiers (SOAs) [165].

MRMs are among the most promising solutions with their high-speed operations, compact footprints, and low RF driving voltages. The MR structures' slow-light effect enables the high modulation efficiency, where photons travel around the active region multiple times and accumulate phase changes before exiting the structures [108]. However, the EO BWs of MRMs are also limited by the photon lifetime. Therefore, researchers would sacrifice the modulation efficiency to achieve high EO BW by designing MR structures with a low quality-factor (Q-factor) [174]. Researchers have used L-shaped p-n junction to maximize the overlap with the optical mode to compensate for the modulation efficiency. Even though the capacitance of the L-shaped p-n junction is higher than the lateral junction, the EO BW of MRM is not limited by the RC constant of the p-n junction. Therefore, a high EO BW is also achieved with improved modulation efficiency [43, 173, 175]. Another issue with the MRMs is the limited extinction ratio (ER), which limits the optical modulation amplitude (OMA) and hinders the application of high-order modulation formats. To address this issue, researchers demonstrate PAM-8 modulations with a high-speed MRM by optimizing the p-n junction and MR structure [171]. Another solution is to use MRR-assisted MZM structures [176, 177]. Lastly, the most critical issue with MRMs are the wavelength tuning and locking circuitry. Since the MRMs are sensitive to fabrication errors and ambient temperature fluctuations, a dynamic circuit is often required to tune and lock the operational wavelength [178–180].

TWMZMs have been widely adopted in high-speed transceiver designs [159, 162]. To optimize the EO BWs of TWMZMs, we need to consider three main factors: the microwave loss dominated by the p-n junction's capacitance, the velocity mismatch between RF signal and optical signal, and the impedance mismatch between the characteristic impedance of the electrode and the termination [25, 160]. To further decrease the microwave loss, researchers propose the series-push-pull structure (SPP), where the p-n junctions are connected back-to-back (B2B) [163]. To compensate for the velocity mismatch, researchers have partially used the slow-wave electrode design [195] or removed the substrate [161] to slow down the speed of the RF signal. The characteristic impedance should be carefully designed considering the electrode dimension, material, and the p-n junctions [164]. Another benefit of TWMZM is the wide operational optical BW and resistance to temperature variations. In addition, the high ER enables higher modulation formats, including PAM-16 [165], 16-quadrature amplitude modulation (16-QAM) [166], and 32-QAM [167]. Researchers have also demonstrated multi-electrode MZMs to generate PAM-4 signal with a 2-bit digital-to-analog converter (DAC) [168, 169]. Nevertheless, there are some inherent drawbacks of TWMZMs. Because of the low modulation efficiency of the reverse-biased p-n junction, the length of a TWMZM can be up to several millimeters. Engineers must adopt a long phase shifter to decrease the driving voltage, sacrificing the EO BW and integration density. Also, the optical ILs introduced by the long p-n junction are pretty significant.

Researchers have used the slow light effect to increase the modulation efficiency and integration density. Initially, researchers have employed BG structures to substitute the straight waveguides in the MZMs [181–185]. However, the modulation efficiency improvement is limited, and the half-wave voltage (V_π) is around 12 V. Also, the EO BW is limited by the long photon lifetime caused by BGs. Furthermore, the optical BW is also limited to 0.5 nm, making the device susceptible to temperature changes. The optical ILs introduced by BGs are also significant. To address the abovementioned issues, researchers have used weakly coupler phase-shifter BGs [45, 186–191]. The optical BW is increased to several nanometers, improving thermal stability. Also, the optical ILs and EO BW are enhanced because of the weakly coupled BGs. High-speed MZMs with P-Cs waveguides are demonstrated as well [44]. However, P-Cs are inherently susceptible to fabrication error, and the optical ILs are also significant.

For low-cost and high-speed transmitters designs, a modulator with high integration density and modulation efficiency, low fabrication and thermal sensitivity, and negligible optical ILs is preferred. The MMZM has the capability of achieving all the targets above. Devices demonstrated to date are based on dual-drive modulation schemes [46, 192, 193]. To simplify the driving and biasing circuitry and increase the integration density further, we propose an SPP MMZM with a compact footprint on the SOI platform.

Chapter 3

Broadband Adiabatic Coupler

Building on the background introduced in Section 2.2.2, this Chapter reports the design, simulation, and experimental results of the OACs with different SRs. Section 3.1 presents the broadband and thermally stable OACs with variable SRs on the SOI platform. Section 3.2 proposes a time-efficient method to analyze and design the OACs. Using this method, we demonstrate OACs with improved performances. Section 3.3 Concludes this Chapter. Section 3.1 of this Chapter is based the author's work in [4]. Section 3.2 of this Chapter is based on the author's work in [3] and [6], respectively.

3.1 Adiabatic coupler with design-intended splitting ratio

3.1.1 Introduction

In this Section, we demonstrate broadband OACs of various SRs, which are resistant to temperature fluctuations and fabrication errors. Section 3.1.2 gives the mathematical analysis of the relationship between the SRs and the output waveguide width differences. In Section 3.1.3, we use a segmented simulation method based on 3-dimension (3D) FDTD and EME techniques to determine the parameters for the OACs operating in the wavelength region from 1260 nm to 1360 nm for the fundamental TE mode. Section 3.1.4 presents the experimental results of the OACs with different SRs at various temperatures.

3.1.2 Operation principle

The schematic of the proposed OAC is shown in Fig. 3.1. We will illustrate the constitution and operation principle of each region individually. Region I consists of two tapered waveguides with a length of L_t separated by a gap of g_1. The widths of the upper and lower waveguides are tapered from w to w_1 and w_2, respectively. This region is designed to gradually taper the widths of the two waveguides without introducing XTs between them. In addition, the injected mode is expected to remain mainly in the same waveguide without exciting higher-order modes. The waveguide spacing g_1 between the two waveguides should be large enough to realize this requirement.

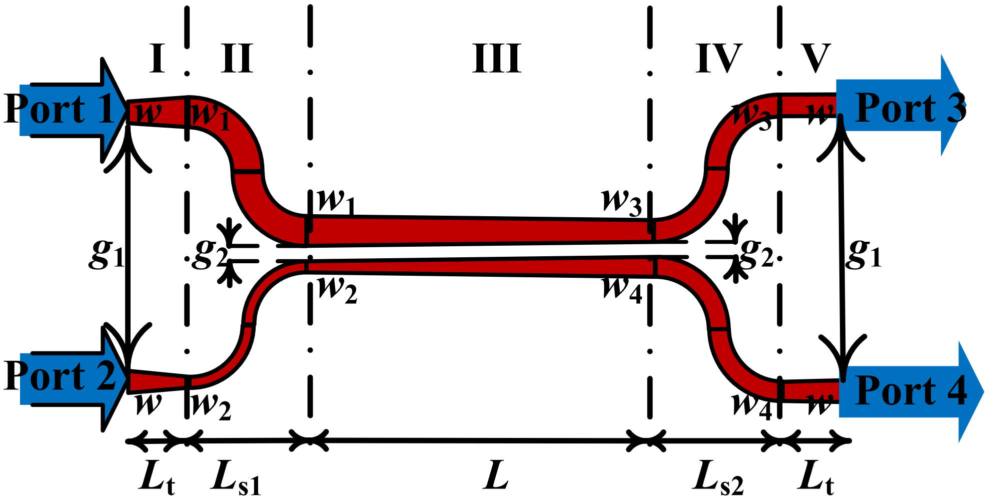

Fig. 3.1 The schematic of the OAC with labeled design parameters. [4] (© 2019 IEEE)

Region II composes a pair of S-shaped waveguide bends with widths w_1 and w_2. We define the width difference of the two input S-shaped waveguide bends, Δw_in, as follows:

$$\Delta w_\mathrm{in} = w_1 - w_2 \tag{3.1}$$

The S-shaped waveguide bends are brought together until a gap of g_2. Region II is designed to solely excite the $1^\mathrm{st}/2^\mathrm{nd}$-order mode of the two-waveguide system when the TE mode is injected from Port 1/Port 2, respectively. When the i^th-order is excited, most of the ILs in Region II come from the $(i+1)^\mathrm{th}$-order mode. Therefore, the analytical solutions of ILs in Region II are developed considering only the i^{th}- and $(i+1)^{\text{th}}$-order modes [196–198]. As shown in [196], the IL_{II} is inversely proportional to the square of the asynchronicity parameter X_{III0}:

$$IL_{\text{II}} \propto \frac{1}{X_{\text{III0}}^2} \tag{3.2}$$

where IL_i represents the IL for Region i ($i = \text{II} - \text{IV}$). The asynchronicity parameter X_{III0} is defined as follows:

$$X_{\text{III0}} \coloneqq \frac{\Delta\beta_{\text{III0}}}{2\kappa_{\text{III0}}} \tag{3.3}$$

where $\Delta\beta_{\text{III0}}$ represents the difference in propagation constants of two isolated waveguides with widths w_1 and w_2, and κ_{III0} is the coupling coefficient of two straight waveguides with widths w_1 and w_2 and a spacing of g_1. Equation 3.2 indicates that smaller IL_{II} can be achieved with larger X_{III0}. As shown in Eqn. 3.3, there are two ways to increase X_{III0}: increase $\Delta\beta_{\text{III0}}$ or decrease κ_{III0}. It is preferred to increase $\Delta\beta_{\text{III0}}$ since the variation of κ_{III0} is negligible when varying the constituent waveguides. In summary, by increasing the input waveguide width difference Δw_{in}, we can reduce the IL_{II} in Region II.

Region III has two tapered waveguides with a length of L and a spacing of g_2. The widths are tapered from w_1 to w_3 and w_4, respectively. The waveguide width difference at the input of this region is Δw_{out}:

$$\Delta w_{\text{out}} = w_3 - w_4 \tag{3.4}$$

Region III is designed to connect the neighbouring regions with an adiabatic transition. In other words, when the $1^{\text{st}}/2^{\text{nd}}$-order mode of the two-waveguide system is excited at the left-hand side of Region III, the same order mode is expected to be the dominating mode transmitted in this region. Next, the analytical expression of IL_{III} is developed, considering only the first two modes when the 1^{st}-order mode is excited. For Region III, $A_1(z)$ and $A_2(z)$ represent the amplitude of the 1^{st}- and the 2^{nd}-order modes, respectively. The coordinates along the transmission direction of the left and right ends are labeled as $z = 0$ and $z = L$, respectively. When injecting the light into Port 1, the amplitudes of the two waveguides at $z = 0$ are $A_1(0) = A_{10}$ and $A_2(0) = 0$. Assuming adiabaticity of Region

III, $A_1(z)$ and $A_2(z)$ are expressed as follows [196]:

$$A_1(z) \approx A_{10} \exp\left(j \int_0^z \beta_1(z')dz'\right) \tag{3.5a}$$

$$A_2(z) \approx A_{10}[\exp\left(j \int_0^z \beta_2(z')dz'\right) \int_0^z c_{12} \frac{\partial \rho}{\partial z'} \exp\left(j \int_0^{z'} [\beta_1(z'') - \beta_2(z'')]dz''\right) dz'] \tag{3.5b}$$

where β_1 and β_2 are the propagation constants of the 1^{st} and the 2^{nd}-order modes, respectively, c_{12} is the coupling coefficient between these two modes, and $\frac{\partial \rho}{\partial z}$ is the rate of the waveguide width change along the propagation direction. The power ratio of the 2^{nd}-order mode over the 1^{st}-order mode is expressed as follows [196]:

$$q_{\text{III}}(z) = \frac{|A_2(z)|^2}{|A_1(z)|^2} = |\int_0^z c_{12} \frac{\partial \rho}{\partial z'} \exp\left(j \int_0^{z'} [\beta_1(z'') - \beta_2(z'')]dz''\right) dz'|^2 \tag{3.6}$$

Under the adiabaticity assumption, c_{12} and $\beta_1(z'') - \beta_2(z'')$ can be approximated as follows:

$$c_{12} \approx \frac{X_{\text{III0}}}{2\Delta w_{\text{in}}} \tag{3.7a}$$

$$\beta_1(z'') - \beta_2(z'') \approx 2\kappa_{\text{III0}} \tag{3.7b}$$

By taking Eqn. 3.7 into Eqn. 3.6, $q_{\text{III}}(z)$ can be simplified as follows:

$$\begin{aligned} q_{\text{III}}(z) &\approx |\int_0^z \frac{X_{\text{III0}}}{2\Delta w_{\text{in}}} \frac{\Delta w_{\text{in}}}{2L} \exp\left(j \int_0^{z'} 2\kappa_{\text{III0}} dz''\right) dz'|^2 \\ &= |\frac{X_{\text{III0}}}{4L} \int_0^z \exp(2j\kappa_{\text{III0}} z') dz'|^2 \\ &= (\frac{X_{\text{III0}}}{4\kappa_{\text{III0}} L})^2 \sin^2(\kappa_{\text{III0}} z) \end{aligned} \tag{3.8}$$

Therefore, IL_{III} is approximated as follows with Eqn. 3.8:

$$IL_{\text{III}} \approx q_{\text{III}}(L) \times |A_1(L)|^2 = |A_1(L)|^2 \times (\frac{X_{\text{III0}}}{4})^2 (\frac{\sin \kappa_{\text{III0}} L}{\kappa_{\text{III0}} L})^2 \tag{3.9}$$

Based on Eqn. 3.9, we can conclude that IL_{III} is negligible with L goes to infinity:

$$0 \leq \lim_{L\to\infty} IL_{\mathrm{III}} \leq |A_1(L)|^2(\frac{X_{\mathrm{III}0}}{4})^2 \lim_{L\to\infty}(\frac{1}{L^2}) = 0 \tag{3.10}$$

On the right-hand side of Region III, the power distribution of the excided mode depends on the constituent waveguides at the intersection. Intuitively, the SRs can be varied by changing Δw_{out}. To establish a semi-analytical relationship between the SR and Δw_{out}, we restrict our attention to the injected i^{th}-order mode and the $(i+1)^{\mathrm{th}}$-order mode. The power ratio of the upper and lower output ports can be approximated as follows, ignoring the XT terms and assuming the 1st-order mode is excited [198]:

$$\frac{P_{\mathrm{up}}(z_0)}{P_{\mathrm{down}}(z_0)} = \frac{1}{\tan^2(\frac{\xi}{2})}, z_0 = L_{\mathrm{t}} + L_{\mathrm{s}1} + L \tag{3.11a}$$

$$\tan(\xi) = \frac{c_{i,i+1}(z_0)}{\varphi(z_0)} \tag{3.11b}$$

$$\varphi(z_0) = \frac{1}{2(\beta_{\mathrm{up}}(z_0) - \beta_{\mathrm{up}}(z_0))} \tag{3.11c}$$

where $c_{i,i+1}$ is the coupling coefficient between the i^{th}- and $(i+1)^{\mathrm{th}}$-order mode [20], β_{up} and β_{down} are the propagation constants of the upper and lower waveguides. Taking Eqn. 3.11b into Eqn. 3.11a, the power ratio between the constituent waveguide is expressed as follows:

$$\frac{P_{\mathrm{up}}(z_0)}{P_{\mathrm{down}}(z_0)} = 1 + \frac{2}{\tan^2(\xi)} + \frac{1\sqrt{1+\tan^2(\xi)}}{\tan^2(\xi)} \tag{3.12}$$

By taking Eqns. 3.11b and 3.11c into Eqn. 3.12, the power ratio can be written as function of the coupling coefficients and effective indices:

$$\frac{P_{\mathrm{up}}(z_0)}{P_{\mathrm{down}}(z_0)} = 1 + \frac{2\pi^2\Delta n_i^2(z_0)}{c_{i,i+1}^2(z_0)}(1 + \sqrt{1 + \frac{c_{i,i+1}^2(z_0)\lambda^2}{\pi^2\Delta n_i^2(z_0)}}) \tag{3.13}$$

where $\Delta n_i(z_0)$ is the effective indices difference between the upper and lower isolated waveguides when the i^{th}-order modes are excited in both waveguides. The expression of SR is as follows:

$$SR = \frac{P_{\mathrm{up}}}{P_{\mathrm{up}} + P_{\mathrm{down}}} \text{ or } \frac{P_{\mathrm{down}}}{P_{\mathrm{up}} + P_{\mathrm{down}}} \tag{3.14}$$

Equations 3.13 and 3.14 establish the relationship between the SR and the effective index difference. To demonstrate the relationship between the SR and Δw_{out}, we need to determine two parameters by numerical modelling: $\Delta n_i(z_0)$ and $c_{i,i+1}(z_0)$. First, we set $w_3 = 0.35$ µm, $g_2 = 0.15$ µm, and w_4 is taken from 0.3 µm to 0.35 µm every 2 nm. Therefore, Δw_{out} ranges from 0 nm to 50 nm every 2 nm. Then, we use the FDE solver to calculate the effective indices of the 1^{st}-order mode for a straight waveguide when its width ranges from 0.3 µm to 0.35 µm in a 2 nm spacing, based on which we calculate $\Delta n_i(z_0)$ for different Δw_{out}. According to [20], $c_{i,i+1}(z_0) = \frac{\pi \Delta n_{i,i+1}(z_0)}{\lambda}$, where $\Delta n_{i,i+1}(z_0)$ is the difference in the effective indices of the i^{th}- and $(i+1)^{\mathrm{th}}$-order modes of the constituent waveguides at z_0. Again, we use the FDE solver to calculate the effective indices of the 1^{st}- and 2^{nd}-order modes for two straight waveguides with widths w_3 and w_4 and a spacing of g_2. With the calculated effective indices, we can calculate $c_{i,i+1}(z_0)$ for different Δw_{out}. Based on the calculated $\Delta n_i(z_0)$ and $c_{i,i+1}(z_0)$, we compute the SR as a function of Δw_{out}. The semi-analytical SR versus Δw_{out} is demonstrated in Fig. 3.2.

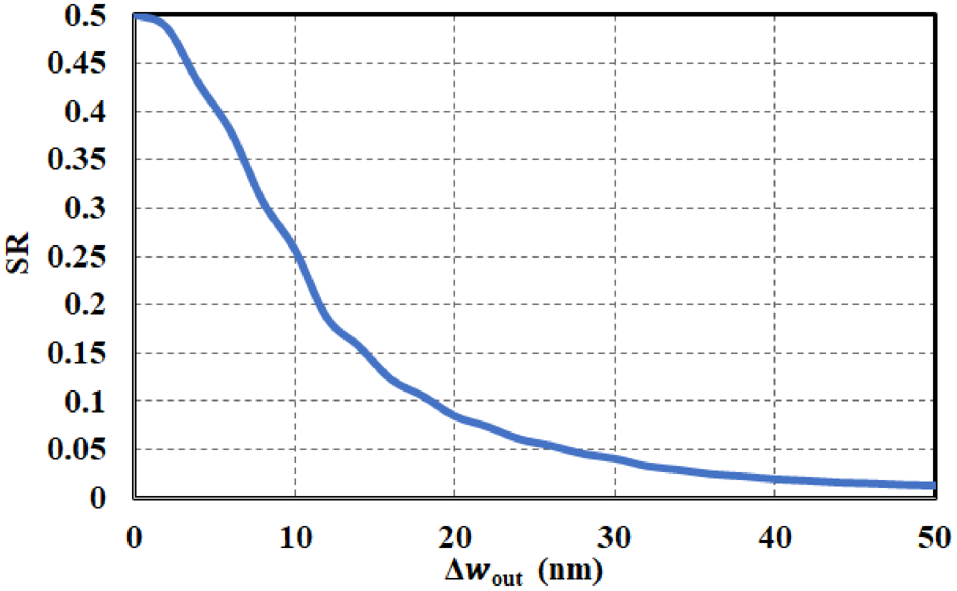

Fig. 3.2 Calculated SR as a function of output waveguide width difference. [4] (© 2019 IEEE)

Region IV contains another pair of S-shaped waveguide bends with widths w_3 and w_4. The S-shaped bends are brought apart from a gap of g_2 to g_1. This region guides the modes into different paths without exciting higher-order modes. Region V has two tapered waveguides with a length of L_t separated by a gap of g_1. The widths are tapered from w_3 and w_4 to w, respectively. This region is to connect the OAC to the rest of the circuit.

Figures 3.3(a) and (b) demonstrate the field propagation through the 3-dB OAC when injecting the fundamental TE mode into Port 1 and 2, respectively. When the TE mode is injected into Port 1, only the TE mode is excited and transmitted along the upper waveguide of Regions I and II. On the right-hand side of Region II, the TE mode in the upper waveguide excites the 1$^{\mathrm{st}}$-order mode of Region III. In Region III, only the 1$^{\mathrm{st}}$-order mode is excited and guided. For a 3-dB OAC, the output waveguide widths are the same, ensuring an equal power distribution with no phase shift at the end of Region III. In Regions IV and V, only the TE mode is guided on both the upper and lower waveguides.

The mode propagation process is similar when the fundamental TE mode is injected into Port 2. The main difference is that the 2$^{\mathrm{nd}}$-order mode is excited and guided throughout Region III. On the right-hand side of Region III, the constituent waveguides have equal power distribution but π phase shift because of the mode property.

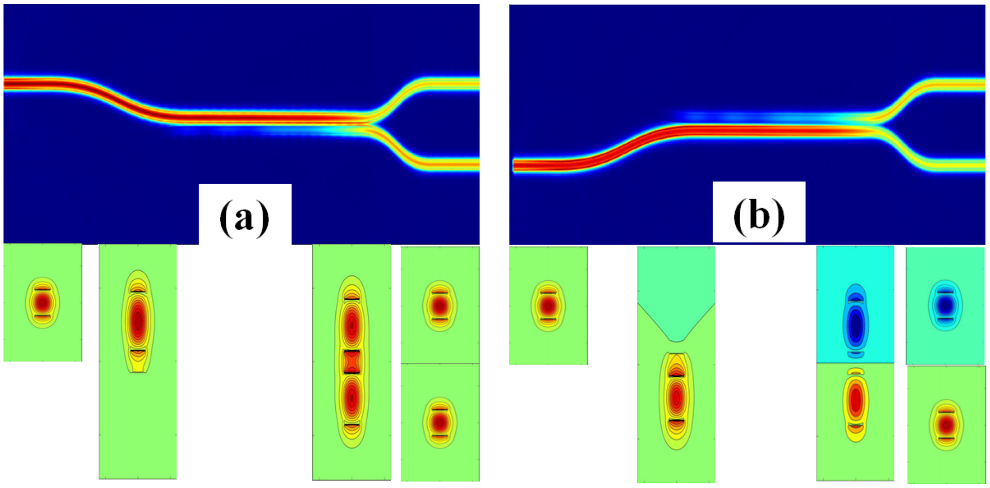

Fig. 3.3 The field propagation diagrams of the proposed OACs and illustrations of the mode profiles at different locations in the devices. The OAC with 50%/50% SR and the TE mode is injected from (a) Port 1; (b) Port 2. [4] (© 2019 IEEE)

Figures 3.4(a) and (b) are the field propagation diagrams for the OAC with a targeted SR of 20%/80% when light is injected from Port 1 and 2, respectively. The mode evolution process is similar to the 3-dB OAC. The difference is that uneven power distribution is achieved with different output waveguide widths.

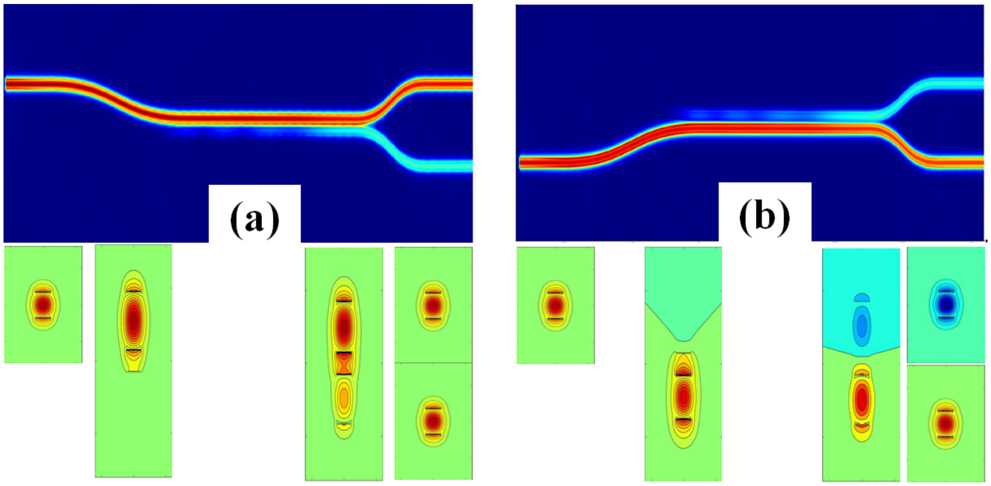

Fig. 3.4 The field propagation diagrams of the proposed OACs and illustrations of the mode profiles at different locations in the devices. The OAC with 20%/80% SR and the TE mode is injected from (a) Port 1; (b) Port 2. [4] (© 2019 IEEE)

3.1.3 Design and simulation

This Section introduces the segmented simulation process to determine the parameters labeled in Fig. 3.1. The values of the waveguide width w and separation g_2 are set beforehand. The waveguide width w is chosen to be 350 nm for single-mode operation. With a smaller g_2, the required length for Region III is shorter. However, limited by the minimum feature size defined by the fabrication process, g_2 is set as 150 nm.

The first four steps use the 3D FDTD solver, and the last two use the EME solver. First, the input waveguide spacing g_1 is explored. The simulated structure includes two parallel, straight, and ten µm-long waveguides with the same width w =350 µm and spacing of g_1. The TE mode is injected into the upper waveguide, and two mode-expansion monitors are placed on the right-hand side to calculate the power coupled into the fundamental TE mode for both waveguides. The spacing, g_1, is set to minimize the XTs between the two waveguides. The simulated XTs as functions of the spacing at three different wavelengths are shown in Fig. 3.5. XTs converge to a negligible level for all three wavelengths when $g_1 \geq 1.3$ μm. Therefore, g_1 is set as 3 μm.

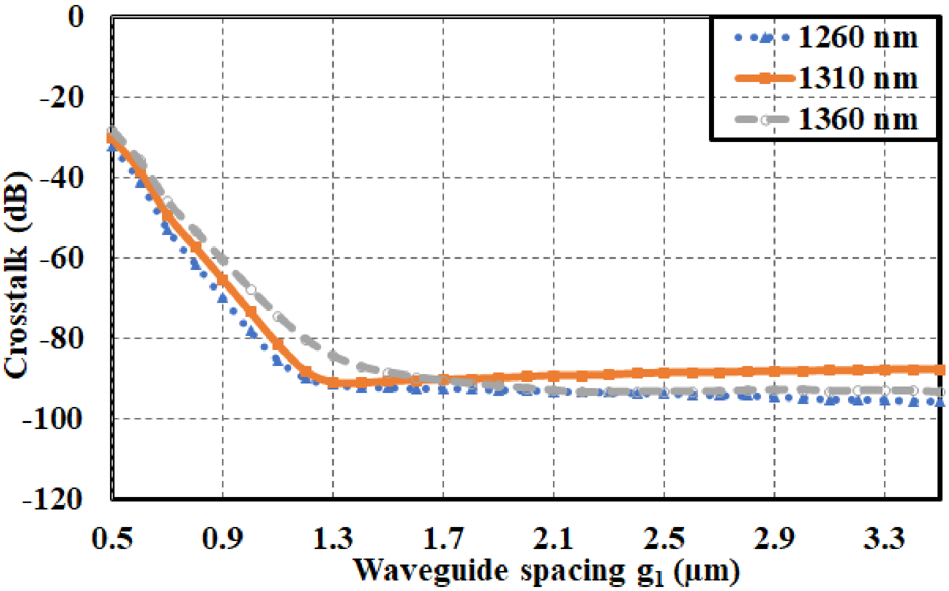

Fig. 3.5 Simulated XTs as functions of input waveguide spacing g_1 at three wavelengths. [4] (© 2019 IEEE)

Since the primary purpose of this work is to demonstrate the OACs with different SRs, we intentionally choose conservative values for the parameters of the OACs. In general, there are two criteria when determining the parameters in the following steps. First, the ILs for different regions are expected to be lower than 0.1 dB, and we assume the ILs are negligible at this level. When ILs are insignificant, we also consider the dimensions resulting in the convergence of ILs.

The second step is determining the input waveguide widths w_1 and w_2 and the length L_{s1} of the two input S-shaped waveguide bends. The simulation structure is based on Region II, as shown in Fig. 3.1. We set $w_1 = w + 0.5\Delta w_{\text{in}}$ and $w_2 = w - 0.5\Delta w_{\text{in}}$. As shown in [34], the difference in IL_{II} when injecting light into the upper and lower waveguides is insignificant. Thus, the results are only presented for the case when light is injected into the upper waveguide. As Δw_{in} is increased from 50 nm to 150 nm with a step of 50 nm, we sweep L_{s1} from 5 μm to 25 μm. Figures 3.6(a)-(c) demonstrate the simulated IL_{II} as functions of L_{s1} when (w1, w2) is (375 nm, 325 nm), (400 nm, 300 nm), and (425 nm, 275 nm), respectively. The corresponding IL_{II} is both negligible and convergent when $L_{\mathrm{s1}} \leq 25$ µm, 20 µm, and 15 µm, respectively. Considering the length of the input S-shaped waveguide bends alone, (w_1, w_2) being equal to (425 nm, 275 nm) is preferred since it achieves a smaller IL_{II} within less area. However, the increase in Δw_{in} will prolong the footprint of the mode-evolution region significantly. Also, the differences of IL_{II} between the last two cases, namely (400 nm, 300 nm) and (425 nm, 275 nm), is within 0.02 dB which is negligible. Taking all above into consideration, we choose (400 nm, 300 nm) for (w_1, w_2) and 20 µm for L_{s1}.

Next, the length L_{t} of the taper is decided. The TE mode is injected into a linear taper with input and output waveguide widths of w and 1 µm, respectively. L_{t} is designed to minimize the IL_{I}. The simulated IL_{I} as functions of L_{t} is shown in Fig. 3.7 at three wavelengths. For all the simulated wavelengths, the IL_{I} are both negligible and convergent when $L_{\mathrm{t}} \geq 5$ µm. Therefore, we set L_{t} to be 5 µm.

The fourth step specifies the length L_{s2} of the two output S-shaped waveguide bends. The simulation structure is based on Region IV. We set $w_3 = w$ and $w_4 = w_3 - \Delta w_{\mathrm{out}}$. In this step, we set $\Delta w_{\mathrm{out}} = 0$ when the maximum L_{s2} is required to reach negligible IL. According to the results from the second step, when increasing Δw_{in} from 50 nm to 150 nm, a smaller L_{s1} is required to reach negligible IL. Similarly, the same conclusion can be drawn for the output S-shaped waveguide bends when Δw_{out} is less than 150 nm. Therefore, when $\Delta w_{\mathrm{out}} = 0$, the required L_{s2} is the largest to reach insignificant ILs. The simulated IL_{IV} as functions of L_{s2} is shown in Fig. 3.8 when the 1^{st}/ 2^{nd}-order mode is excited at three wavelengths. As shown in Fig. 3.8(a), the IL_{IV} is negligible and convergent when $L_{\mathrm{s2}} \leq 10$ µm. In Fig. 3.8(b), even though the IL_{IV} is not convergent, the value is ten-fold smaller than in Fig. 3.8(a). The fluctuation comes from the computational software error. Based on the simulation results, we choose 10 µm for L_{s2}.

The fifth step is to select the length L of the mode-evolution region. The simulation structure is based on Region III in Fig. 3.1. On the right-hand side of Region III, w_3 is set to be 350 nm and $w_4 = w_3 - \Delta w_{\mathrm{out}}$. The 1^{st}/2^{nd}-order mode is injected from the left-hand side of Region III and is chosen as the targeted mode on the right-hand side of Region III, respectively. By analyzing the scattering matrix, we calculate the amount of power coupled into the 1^{st}/2^{nd}-order mode, respectively. As Δw_{out} is increased from 0 nm to 20 nm with a step of 10 nm, we sweep L from 20 µm to 200 µm. Figures. 3.9(a) – (c) show the simulated $\mathrm{IL}_{\mathrm{III}}$ as functions of the mode-evolution length L when injecting TE

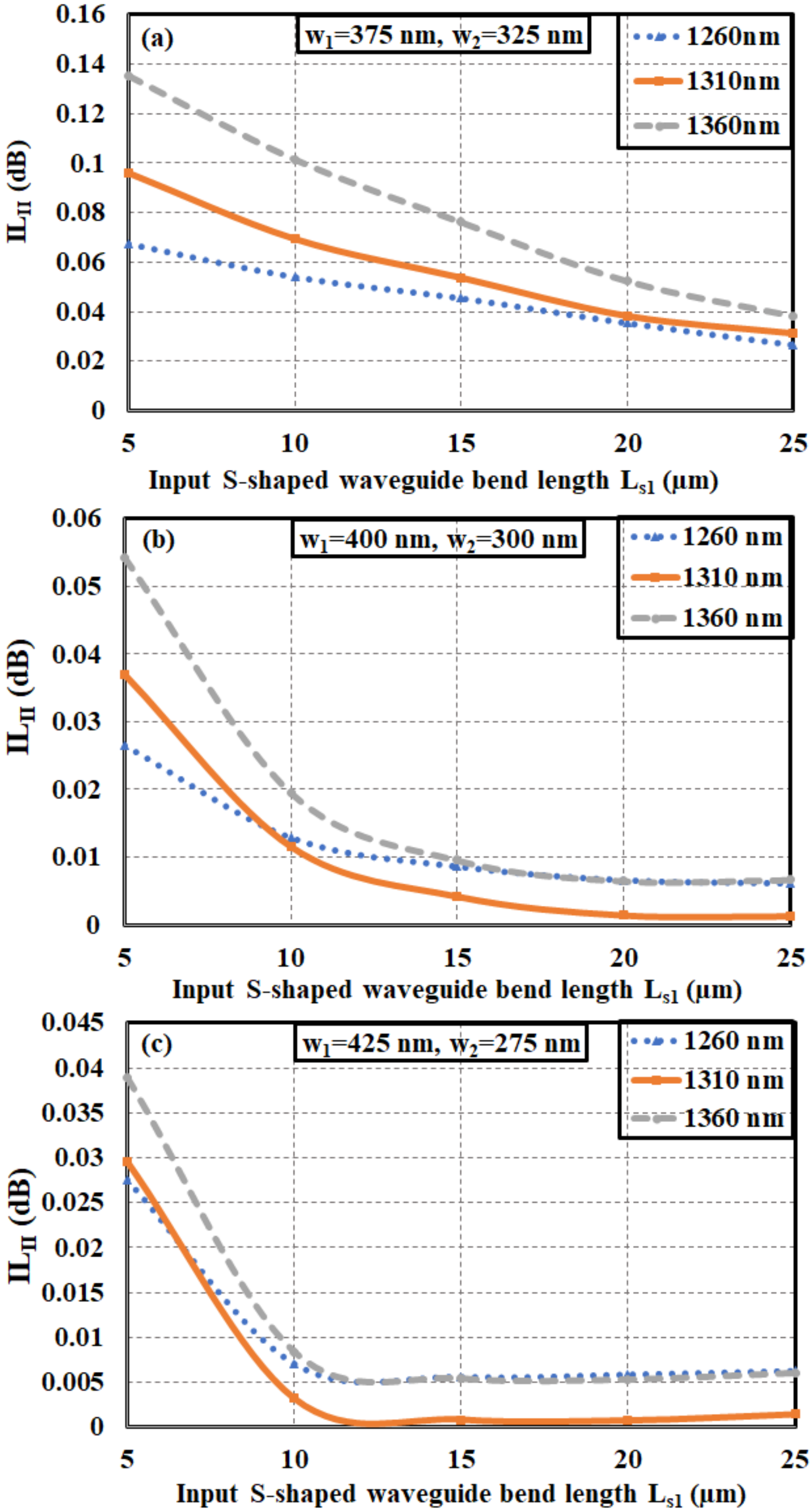

Fig. 3.6 Simulated IL_{II} as functions of S-shaped waveguide bends length L_{s1} at three wavelengths when (a) $w_1 = 375$ nm, $w_2 = 325$ nm; (b) $w_1 = 400$ nm, $w_2 = 300$ nm; (c) $w_1 = 425$ nm, $w_2 = 275$ nm. [4] (© 2019 IEEE)

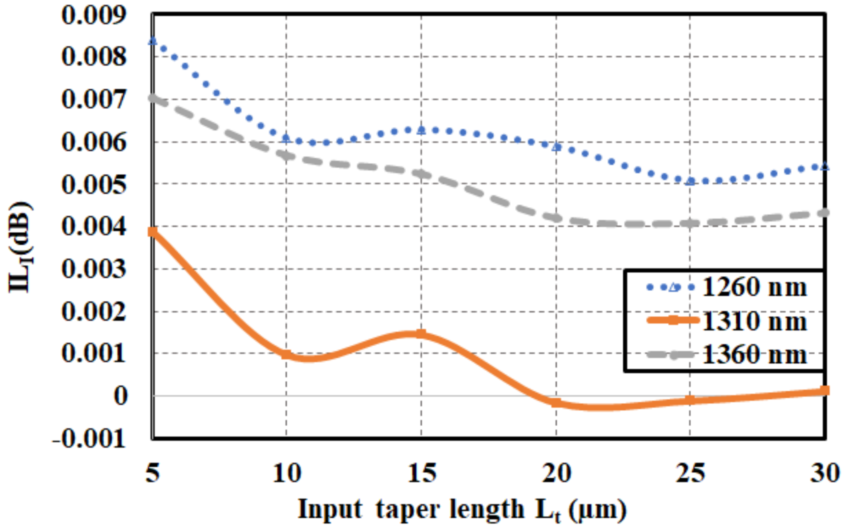

Fig. 3.7 Simulated IL_I as functions of taper length L_t at three wavelengths. [4] (© 2019 IEEE)

mode into Port 1. Since the results are similar when injecting TE mode into Port 2, we only present the results for Port 1 to avoid redundancy. For a fixed value of Δw_out, IL_III is higher at a shorter wavelength, resulting from the weaker coupling at shorter wavelengths. At the same wavelength, IL_III is smaller with larger Δw_out. The output end of imbalanced OACs can be treated as a cross-section of the 3-dB OAC. Thus, it takes less distance to reach the steady-state for Region III with a larger Δw_out. Considering all the above, IL_III is negligible and convergent when $L \geq 180$ μm. Therefore, we choose L=200 μm for the OAC.

The sixth step is determining the relationship between the SR and the Δw_out. The whole device shown in Fig. 3.1 is simulated. Apart from w_4, the other parameters are set according to previous steps. For Port 1 - Port 4, the fundamental TE mode is chosen as the expansion mode. By analyzing the scattering matrix computed by the EME solver, we calculate the amount of power coupled into the TE mode for Port 3 and Port 4 and then calculate the SR based on it. The simulated SRs as functions of Δw_out are shown in Figs. 3.10(a) – (b) when injecting TE mode into Port 1 and Port 2, respectively. Figures. 3.11(a) – (b) show the simulated SRs as functions of wavelength for the OAC with $\Delta w_\mathrm{out} = 10$ nm when injecting TE mode into Port 1 and Port 2, respectively. At 1310 nm, the SR is around 79%/21%. From 1260 nm to 1310 nm, the largest SR-deviation away from the SR

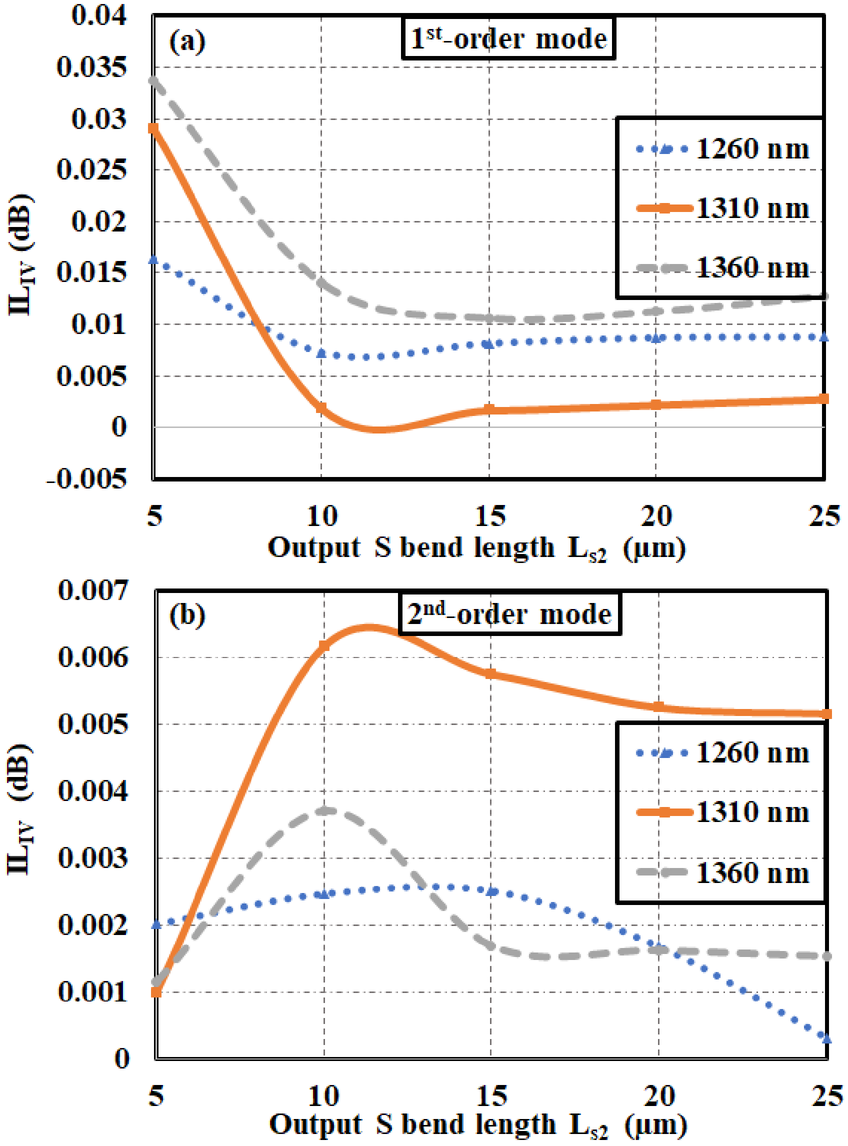

Fig. 3.8 Simulated IL_{IV} as functions of S-shaped waveguide bend length L_{s2} at three wavelengths when exciting the (a) 1st- and (b) 2nd-order modes. [4] (© 2019 IEEE)

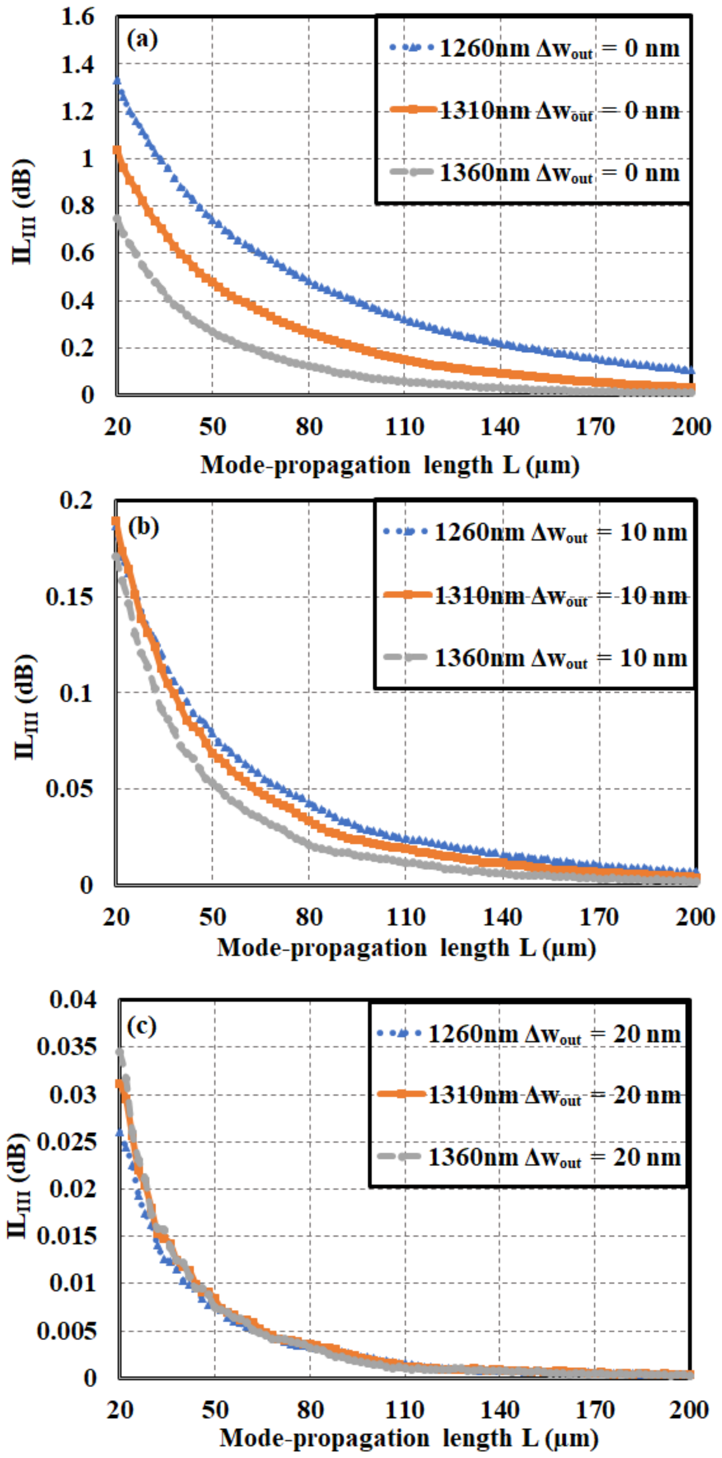

Fig. 3.9 Simulated IL_{III} as functions of L at three wavelengths when injecting TE mode into Port 1 and Δw_{out} is (a) 0 nm; (b) 10 nm; and (c) 20 nm. [4] (© 2019 IEEE)

at 1310 nm is 1.03%. From 1310 nm to 1360 nm, the largest SR-deviation away from the SR at 1310 nm is 0.68%. The SR-deviation difference between wavelengths comes from the more powerful coupling strength at longer wavelengths.

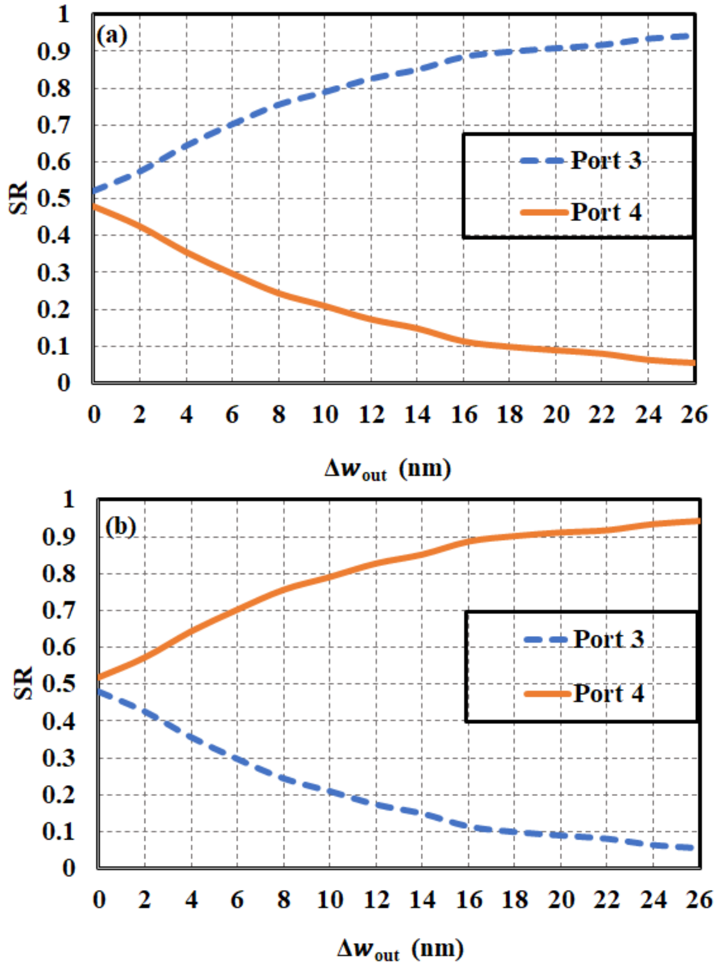

Fig. 3.10 Simulated SRs as functions of Δw_{out} when injecting the TE mode into (a) Port 1; (b) Port 2. [4] (© 2019 IEEE)

3.1.4 Fabrication and experiment results

The schematic of the experimental setup is shown in Fig. 3.12. The setup comprises optical components, mechanical support, and a thermoelectric cooler (TEC) controller. The optical connections are introduced first. The tunable laser is connected to the CT400

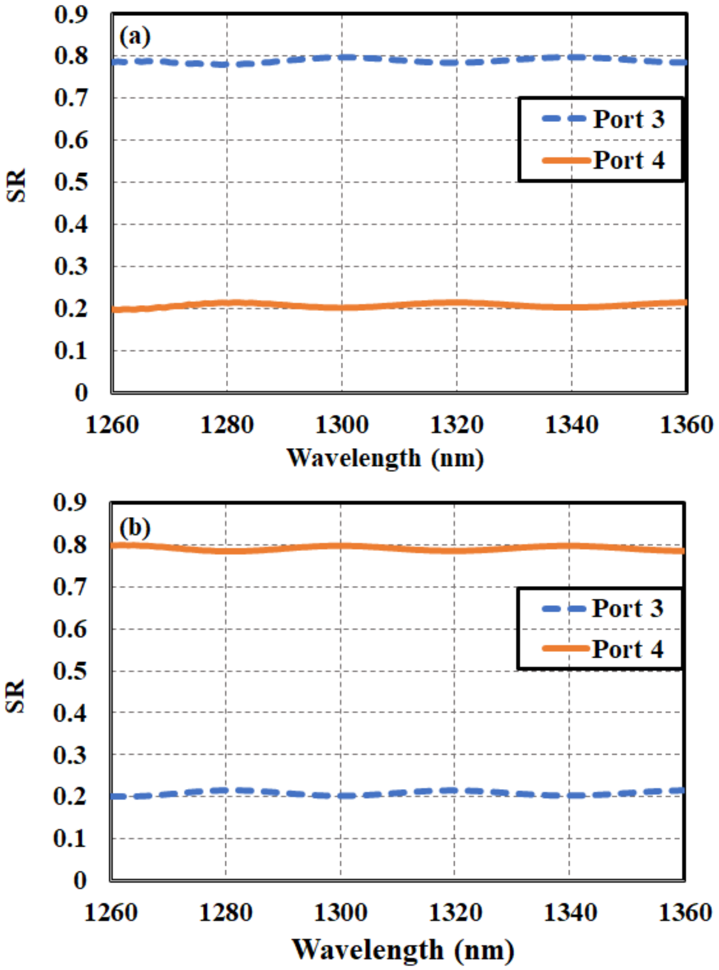

Fig. 3.11 Simulated SRs as functions of wavelength when $\Delta w_{\mathrm{out}} = 10$ nm and injecting TE mode from (a) Port 1; (b) Port 2. [4] (© 2019 IEEE)

passive optical component tester. The output light of CT400 is sent to a polarization controller, which is then connected to the FAU. The FAU is used to inject and collect light from the on-chip vertical GCs. The received optical signals are connected to the four input ports of CT400. The mechanical part is divided into those that support the FAU and those that move the chip. An FAU holder capable of moving in three directions and rotating in three angles is used to hold and adjust the position of the FAU. The Maple Leaf automated stage controller is used to move the stage with the SiP chips on top in the 2-dimension (2D) plane. The top and side-view cameras are used to monitor the movement of the chips and the FAU. To test the thermal stability of devices, we use a 30×30 mm^2 Peltier element to thermally tune the chip stage [199]. The chip is placed on top of a large piece of copper that serves as a heat sink. The Peltier element is mounted between the heat sink and the chip mount block. A thermistor is embedded in the chip mount block and is wired to the temperature controller.

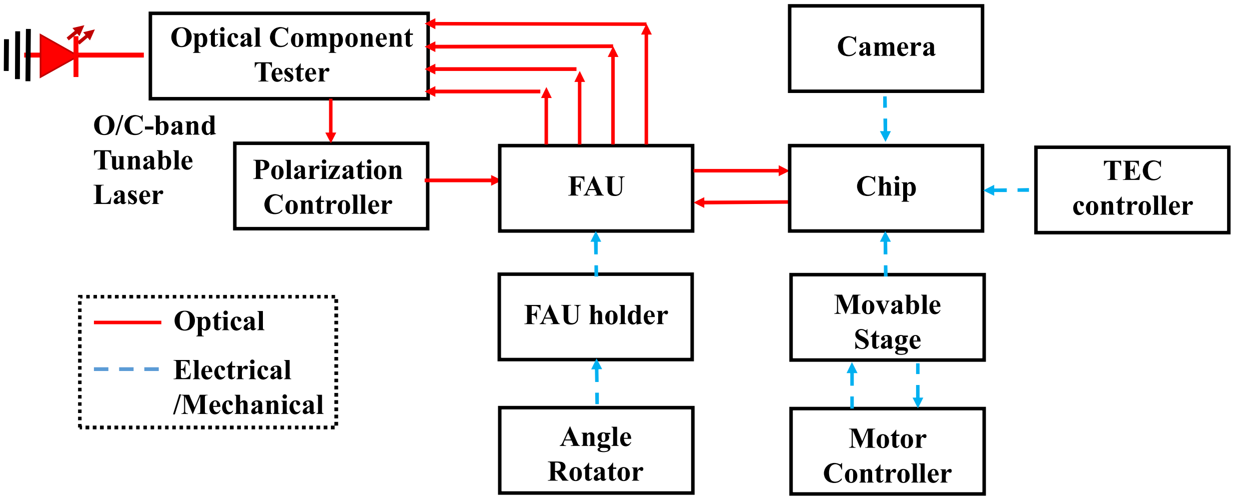

Fig. 3.12 The schematic of the experiment setup. [4] (© 2019 IEEE)

The OACs were fabricated on a 200 mm SOI wafer with 220 nm nominal top silicon thickness using 193 nm optical lithography. Several variations of OACs with different Δw_{out} were fabricated on the same wafer. Vertical GCs are used for optical interface with approximately 10 dB loss at 1310 nm.

The unbalanced MZI test structures are used to characterize the SRs for the designed OACs. For each MZI test structure, two identical OACs are connected by two optical waveguide paths with different lengths. The length difference of the two optical waveguide paths results in an FSR in the measured spectrum from which the ERs can be extracted. Once the ERs are extracted, the SRs can be calculated using the formula below [31]:

$$SR = \frac{1}{2} \pm \frac{1}{2}\sqrt{\frac{1}{10^{\frac{ER}{10}}}} \tag{3.15}$$

Figure 3.13 shows the measured ERs as functions of the wavelength when Δw_{out} equals 0 nm to 25 nm with a step of 5 nm. Based on Fig. 3.13 and Eqn. 3.15, we can calculate the corresponding SRs for different wavelengths. The ERs for different Δw_{out} increase around 1350 nm to 1360 nm, which results from the nonuniformity of the GCs used in the test structures.

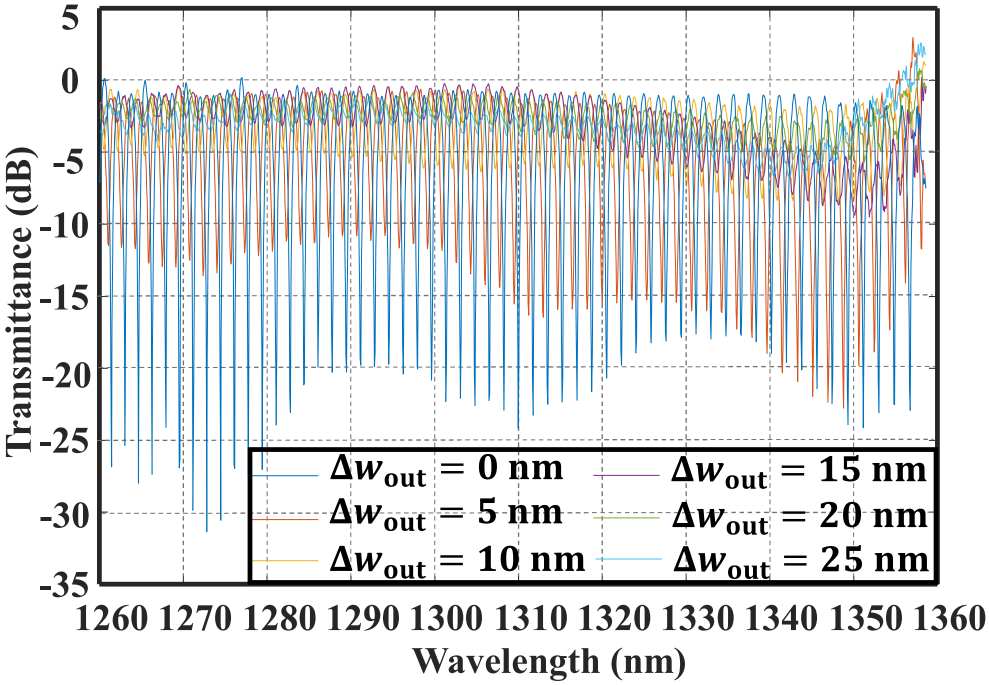

Fig. 3.13 ERs as functions of the wavelength when Δw_{out} equals to 0 nm to 25 nm with a step of 5 nm. [4] (© 2019 IEEE)

Researchers use the cut-back method to calculate the ILs for compact devices where many of the same devices are cascaded. However, limited by the large footprint, another method is used to estimate the ILs of the OACs. The transmission spectrum of a pair of GCs connected B2B is first measured. Since the test structure of OACs also contains two GCs, the ILs introduced by the OACs can be assessed by deducting the transmission spectra of the B2B GCs. However, this method has two limitations. First, the limited BW and the roll-off of the GC spectrum constrained us from characterizing the total operating bandwidth of our device, especially at the longer wavelength side, as shown in Fig.3.13. Second, the spectrum repeatability of the GC we used is limited, which gave us an uncertainty of about 1 dB for the same GC design located at different places of the chip. Such uncertainty in ILs from the GCs is about a magnitude more significant than the ILs of our devices. Therefore, characterizing the ILs of our devices with such GCs will not be accurate. Nevertheless, as shown in Fig. 3.13, over the wavelength range from 1260 nm to 1320 nm, the ILs of our devices are about 1 dB, mainly attributed to the uncertainty of the grating coupler. Beyond 1320 nm, the uncertainty from the grating coupler increases dramatically, and it is not clear to see the actual ILs of our devices.

Figure 3.14 displays the SRs as functions of Δw_{out} at a wavelength of 1310 nm. The diamond, triangle and square markers denote the data calculated from the semi-analytical representation, EME simulation, and experiment, respectively. The dashed line represents the exponential curve fit for the experiment data. The deviations between the data and the exponential curve fit are 6.1%, 2.8% and 6.5% for semi-analytical representation, EME simulation, and experimental data, respectively. The slight difference between the simulation and experimental results suggests that the exponential function is a reliable way to describe the relationship between the SR and Δw_{out}, which can be used to customize OACs with random SRs.

Figure 3.15 shows the simulated and measured SRs at room temperature and the variations of SRs under different temperatures as functions of the wavelength of the designed OACs. The orange and blue lines depict the SRs calculated from the EME simulation and experiment. The solid and dashed lines describe the output power from Port 3 and Port 4, respectively. The error bars parallel to the y-axis show the variations of SRs at different wavelengths when temperatures are increased from 0°C to 100°C and 20°C to 50°C for simulation and experiment, respectively. The maximum variations caused by temperature across the entire O-band are 1.6% and 1.3% for simulation and experiment, respectively. Since the tuning range of Peltier is below 60 °C, we did not increase the stage temperature above 50°C. However, the simulation results suggest that the variation of SRs caused by temperature change is negligible even at 100°C. The slight SRs variation under 30 °C temperature change proves the thermal stability of the proposed OACs.

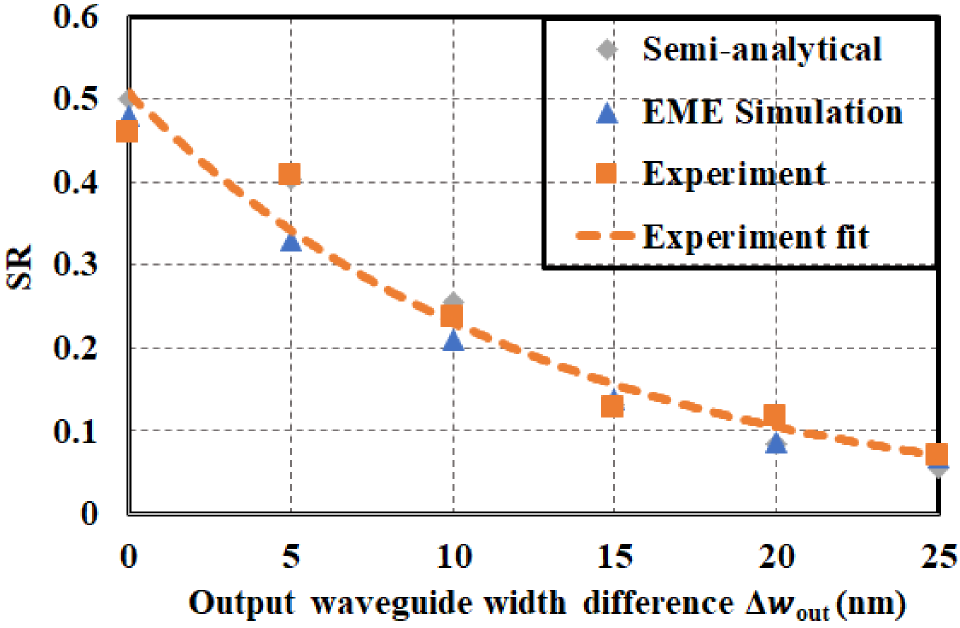

Fig. 3.14 SRs calculated from the semi-analytical expression, EME solver, and experimental results as functions of Δw_{out} at 1310 nm. [4] (© 2019 IEEE)

Recently, several imbalanced OACs, DCs, and MMI couplers have been demonstrated [30,31,200,201]. The comparisons between the state-of-the-art imbalanced couplers with the proposed OACs are summarized in Table 3.1. The critical advantage of mode-evolution-based devices such as the one we presented in the paper over the mode-coupling-based devices such as DCs and the MMI couplers is the insensitivity to thermal change. Such thermal insensitivity is extremely important for datacom applications where the devices must operate within an extensive temperature range from 0 °C up to 80 °C. Unfortunately, the refractive index of silicon is temperature-dependent and is reported to be 1.87×10^{-4}/K at 1500 nm. For a temperature change of 80 °C, the index change is approximately 1.50×10^{-2}, deteriorating the performance of any mode-coupling-based devices such as DCs and MMI couplers. However, there are still many improvements that could be made to OACs. For example, the footprint of this device could be reduced further by using either sub-wavelength grating or a rib waveguide.

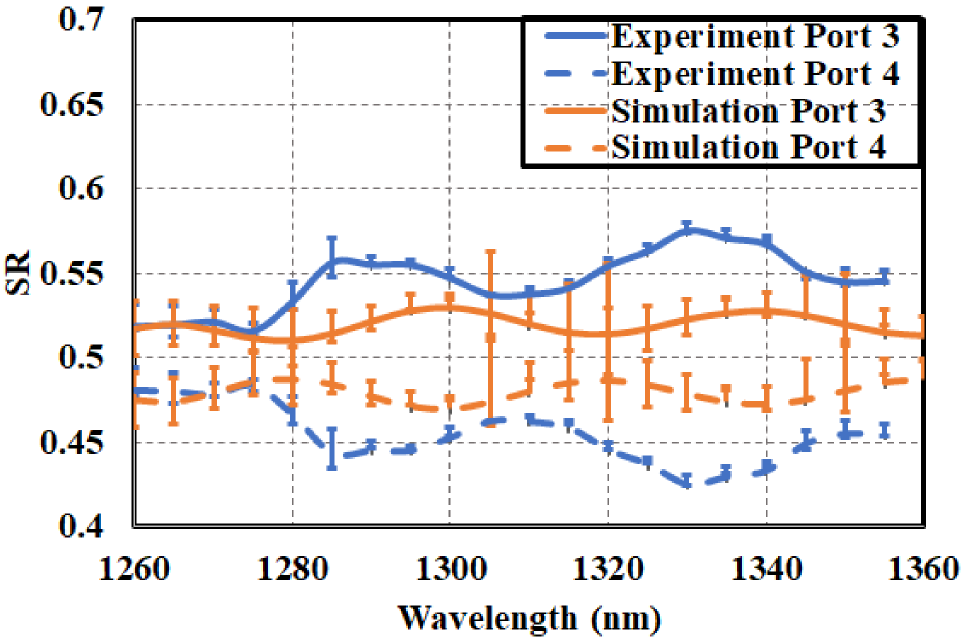

Fig. 3.15 SRs calculated from simulation and experiment as functions of the wavelength under different temperatures. [4] (© 2019 IEEE)

Table 3.1 Comparison of the state-of-the-art imbalanced couplers [4] (© 2019 IEEE)

Ref.	Type	In*out	Average measured SR	Maximum variation	BW	Footprint	Temperature sensitivity
[30]	DC	2*2	80%/20%	6%	100 nm	1.3*23 µm^2	N/A
[31]	DC	2*2	80%/20%	3%	100 nm	3*14 µm^2	N/A
[200]	MMI	1*2	72%/28%	5%	10 nm	3*18.2 µm^2	N/A
[201]	MMI	2*2	85%/15%	3%	50 nm	10*185 µm^2	N/A
This work	OAC	2*2	78%/22%	6.2%	100 nm	4*240 µm^2	1.3% SR variation for 30°C variation

3.2 Adiabatic coupler with nonlinearly tapered mode-evolution region

3.2.1 Introduction

In this Section, we first derive the boundary conditions and the constraints on the tapering functions of the mode-evolution region. Following the derived conditions and constraints, we choose linear, quadratic, and exponential tapering functions and quantitatively compare the performance of the OACs with these functions. The OACs are designed for the fundamental TE mode operating from 1500 nm to 1600 nm. Next, the analyses are validated using experimental results. For the designed 3-dB OAC, the quadratic separation and exponential width tapering function give the best performance. The SRs of the designed 3-dB OAC using this function are within 3 ± 0.33 dB with a mode-evolution length of 110 μm. Using the same tapering method, we also demonstrate several imbalanced OACs with SRs from 8%/92% to 42%/58%.

3.2.2 Theoretical analysis

The schematic of the proposed OAC is shown in Fig. 3.16. The device is divided into five regions. Region I consists of two tapered waveguides with a length L_t separated by a gap g_1. The widths of the upper and lower waveguides are tapered from w to $w_1(0)$ and $w_2(0)$, respectively. Region II has a pair of S-shaped waveguide bends with widths $w_1(0)$ and $w_2(0)$. Region III composes two tapered waveguides with a length of L. Since the waveguide width and gap tapering function are our primary interest, the left and right end of Region III are labeled as $z = 0$ and $z = L$, respectively, where z is the propagation direction. The widths are tapered from $w_1(0)$ and $w_2(0)$ to $w_1(L)$ and $w_2(L)$, respectively. The gap between the two waveguides is tapered from $g_2(0)$ to $g_2(L)$. Region IV contains another pair of S-shaped waveguide bends with widths $w_1(L)$ and $w_2(L)$, respectively. Region V includes two tapered waveguides with a length of L_t separated by a gap of g_1. The widths are tapered from $w_1(L)$ and $w_2(L)$ to w, respectively.

For Region III, the guided mode amplitudes are denoted as $|\Psi\rangle = [A_1, A_2]^\mathrm{T}$ where A_1 and A_2 represent the amplitudes of the modes in the upper and lower waveguides, respectively. Assuming the scalar and paraxial approximation and weak coupling, the amplitudes change

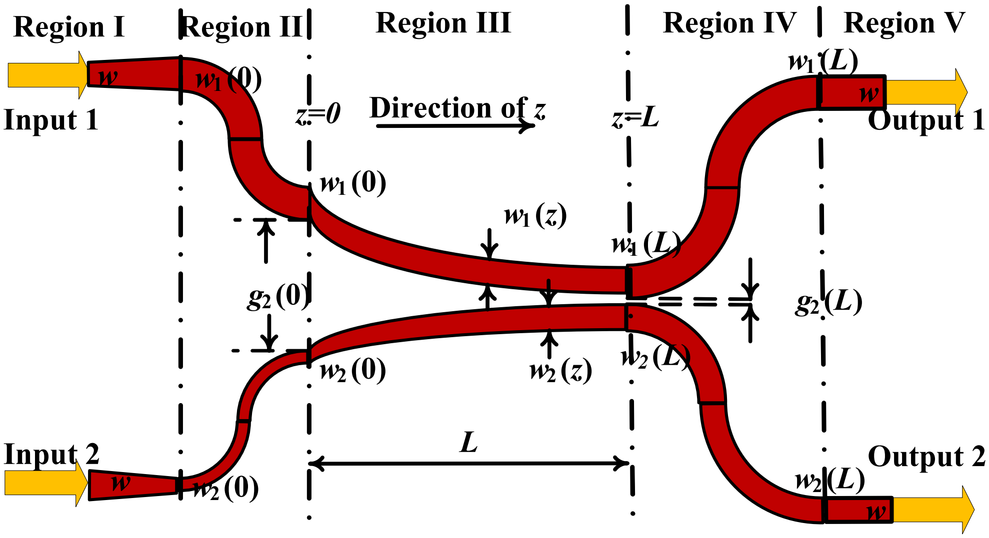

Fig. 3.16 The schematic for the OAC with labeled parameters. [3] (© 2021 IEEE)

along the propagation direction is expressed as follows [202]:

$$\frac{d}{dz}\left|\Psi\right\rangle = -i\begin{bmatrix}-\Delta & \Omega \\ \Omega & \Delta\end{bmatrix}\left|\Psi\right\rangle \tag{3.16}$$

where Ω is the coupling coefficient, $\Delta = \beta_{\mathrm{up}} - \beta_{\mathrm{lo}}$, with β_{up} and β_{lo} being the propagation constants of the modes for the upper and lower waveguides, respectively. When light is injected into the upper (lower) waveguide, only the 1^{st}- (2^{nd}-) order mode is excited. Since the amplitude of the 1^{st}- (2^{nd}-) order mode at the left end of Region III is focused mainly in the upper (lower) waveguide, the 1^{st}- and 2^{nd}-order modes at the left end of Region III can be written as $\left|1\right\rangle = [1, 0]^{\mathrm{T}}$ and $\left|2\right\rangle = [0, 1]^{\mathrm{T}}$, respectively. Next, the first two order modes of the two-waveguide system can be expressed as follows [106]:

$$\left|\Phi_+\right\rangle = \sin\Theta\left|1\right\rangle + \cos\Theta\left|2\right\rangle \tag{3.17a}$$

$$\left|\Phi_-\right\rangle = -\cos\Theta\left|1\right\rangle + \sin\Theta\left|2\right\rangle \tag{3.17b}$$

where $\Theta = \frac{1}{2}\tan^{-1}(\frac{\Omega}{\Delta})$. The adiabaticity of the device is closely related to the modes of the two-waveguide system and can be expressed by the Hamiltonian matrix element Υ as follows [203]:

$$\Upsilon = \frac{1}{L}\frac{|\left\langle \dot{\Phi}_+ \middle| \Phi_- \right\rangle|}{|2\sqrt{\Delta^2+\Omega^2}|} \tag{3.18}$$

where $\dot{}$ denotes the first order derivative with respect to z, and $\dot{\Phi}_+ = \dot{\Theta}\cos\Theta\,|1\rangle - \dot{\Theta}\sin\Theta\,|2\rangle$. Therefore Υ can be written as a function of Δ and Ω:

$$\Upsilon = \frac{1}{4L}\left|\frac{\dot{\Omega}\Delta - \Omega\dot{\Delta}}{(\Omega^2+\Delta^2)^{\frac{3}{2}}}\right| \tag{3.19}$$

A smaller Υ means less power would be coupled to higher-order modes. Ideally, with infinite mode-evolution length L, Υ would be negligible. The main priority is to minimize Υ_{max} and the required mode-evolution length.

To better explore Υ, the numerical approximations for Ω and Δ are introduced [84]:

$$\Delta = \alpha^{\mathrm{T}}W, \quad \alpha = [\alpha_1, \alpha_0]^{\mathrm{T}}, \quad W = [w_{\mathrm{diff}}(z), 1]^{\mathrm{T}} \tag{3.20a}$$

$$\Omega = b_0\exp\big(\beta^{\mathrm{T}}G\big), \quad \beta = [\beta_1, \beta_0]^{\mathrm{T}}, \quad G = [g_2(z), 1]^{\mathrm{T}} \tag{3.20b}$$

where α, b_0, and β are constants and $w_{\mathrm{diff}}(z) = w_1(z) - w_2(z)$. Inserting Eqns. 3.20a and 3.20b into Eqn. 3.19, Υ can be written as follows:

$$\Upsilon = \frac{\Omega}{4L}\left|\frac{b_0\beta^{\mathrm{T}}\dot{G}\Delta - \alpha^{\mathrm{T}}\dot{W}}{(\Omega^2+\Delta^2)^{\frac{3}{2}}}\right| \tag{3.21}$$

Next, we derive the constraints on these constants based on their definition and the operational principles of the OAC: (1) Ω and Δ are both non-negative; (2) in Region III, the waveguide width difference $w_{\mathrm{diff}}(z)$ is decreasing along the propagation direction to make sure that power is gradually transferred from one arm to the other arm. Thus, the propagation constant difference Δ is also decreasing; (3) with the two constituent waveguides getting close, the coupling strength Ω increases along the propagation direction. To sum up, the constraints on the parameters mentioned above are the follows:

$$\Delta,\ \Omega \geq 0 \Rightarrow b_0 \geq 0 \tag{3.22a}$$

$$\dot{\Delta} = \alpha_1\dot{w}_{\mathrm{diff}}(z) \leq 0,\ \ \dot{w}_{\mathrm{diff}}(z) \leq 0 \Rightarrow \alpha_1 \geq 0 \tag{3.22b}$$

$$\dot{\Omega} = b_0\beta_1\dot{g}_2(z)\exp\big(\beta^{\mathrm{T}}G\big) \geq 0,\ \ \dot{g}_2(z) \leq 0 \Rightarrow \beta_1 \leq 0 \tag{3.22c}$$

After determining the constraints for the parameters, we specify the boundary conditions next. At the left end of Region III, to ensure that the coupling to higher-order modes is negligible, the waveguides are intentionally separated so that their coupling strength is negligible. Also, to make sure that the input mode stays in the waveguide into which it is injected, the waveguide width difference is introduced at the left end of Region III. At the right end, to design a 3-dB OAC, there is no waveguide width difference, indicating no propagation constant difference. Thus, the mathematical expressions of the boundary conditions can be summarized as follows:

$$\Omega(0) = 0,\ \ \Delta(0) > 0 \tag{3.23a}$$

$$\Omega(L) > 0,\ \ \Delta(L) = 0 \tag{3.23b}$$

To examine the influence of width change on Υ, the gap is set to be constant. By applying Eqns. (3.22a) - (3.22c), Υ is simplified as follows:

$$\Upsilon = -\frac{\Omega}{4L}\frac{\alpha_1\dot{w}_{\mathrm{diff}}}{(\Omega^2+\Delta^2)^{\frac{3}{2}}} \tag{3.24}$$

To observe the behavior of Υ along z, the first order derivative of Υ is calculated and expressed as follows:

$$\dot{\Upsilon} = -\frac{\alpha_1\Omega[\ddot{w}_{\mathrm{diff}}(\Omega^2+\Delta^2) - 3\dot{w}_{\mathrm{diff}}\Delta\dot{\Delta}]}{4L(\Omega^2+\Delta^2)^{\frac{5}{2}}} \tag{3.25}$$

To ensure adiabatic power transition along the mode-evolution region, Υ_{max} is expected to be shifted toward the end of that region. To realize this, $\dot{\Upsilon} \geq 0$ has to be true along this region and a certain constraint over $w_{\mathrm{diff}}(z)$ is required:

$$\dot{\Upsilon} \geq 0 \Rightarrow \ddot{w}_{\mathrm{diff}}(z) \leq \frac{3\dot{w}_{\mathrm{diff}}\Delta\dot{\Delta}}{\Omega^2+\Delta^2} \tag{3.26}$$

Then, Υ_{max} is at $z = L$ and can be expressed as:

$$\Upsilon_{\mathrm{max}} = -\frac{\alpha_1\dot{w}_{\mathrm{diff}}(L)}{4L\Omega^2(L)} \tag{3.27}$$

To decrease the XTs of the device, $\Upsilon_{\max}$ needs to be reduced. Therefore, based on Eqn. 3.27, we need to decrease $|\dot{w}_{\text{diff}}(L)|$ - the slope of the width function at the right end of Region III, which requires $\ddot{w}_{\text{diff}} \geq 0$.

Next, we evaluate the effect of gap change on Υ while keeping a constant width change. Assuming the change of waveguide width-difference is very slow:

$$\lim_{\dot{W}\to 0} \dot{\Delta} = \lim_{\dot{W}\to 0} \alpha^{\mathrm{T}} \dot{W} = 0 \tag{3.28}$$

Under this assumption, Υ can be simplified as follows:

$$\Upsilon = \frac{b_0 \beta_1 \dot{g}_2(z) \Omega \Delta}{4L(\Omega^2 + \Delta^2)^{\frac{3}{2}}} \tag{3.29}$$

Given the boundary conditions $\Omega(0) = \Delta(L) = 0$, we have $\Upsilon(0) = \Upsilon(L) = 0$. Thus, $\dot{\Upsilon} \geq 0$ cannot be guaranteed along Region III. Next, we take the first order derivative of Υ:

$$\dot{\Upsilon} = \frac{b_0 \beta_1 \Delta \Omega}{4L(\Omega^2 + \Delta^2)^{\frac{5}{2}}} [b_0 \beta_1 (\dot{g}_2(z))^2 (\Delta^2 - 2\Omega^2) + \ddot{g}_2(z)(\Delta^2 + \Omega^2)] \tag{3.30a}$$

$$\dot{\Upsilon}(z_0) = 0 \;\text{ when }\; \Delta^2 = 2\Omega^2 - \frac{3\Omega^2 \ddot{g}_2(z)}{b_0 \beta_1 (\dot{g}_2(z))^2 + \ddot{g}_2(z)} \tag{3.30b}$$

Since Δ is a decreasing function and Ω is an increasing function, there is only one possible z_0. Therefore, we can obtain the following inequalities and equation:

$$\dot{\Upsilon} \geq 0 \text{ when} z < z_0 \tag{3.31a}$$

$$\dot{\Upsilon} \leq 0 \text{ when} z \geq z_0 \tag{3.31b}$$

$$\Upsilon_{\max} \text{ when} z = z_0 \tag{3.31c}$$

Similarly, z_0 is expected to be as close to L as possible to decrease the XTs level in the middle of the mode-evolution region. The second term of Eqn. 3.30b should be positive to realize this, implying the following conditions:

$$\ddot{g}_2(z) \leq 0 \text{ or } \; \ddot{g}_2(z) \geq -b_0 \beta_1 (\dot{g}_2(z))^2 \geq 0 \tag{3.32}$$

With the second term of (3.30b) being positive, the following inequality is true:

$$\Delta^2 = 2\Omega^2 - \frac{3\Omega^2 \ddot{g}_2(z)}{b_0\beta_1(\dot{g}_2(z))^2 + \ddot{g}_2(z)} \leq 2\Omega^2 \tag{3.33}$$

When the equality is taken, z_0 is furthest to the right end of Region III, indicating the largest XT. In this case, Υ_{max} can be expressed as follows:

$$\Upsilon_{\text{max}} = \frac{\sqrt{2}b_0\beta_1\dot{g}_2(z_0)}{4 \times 3^{\frac{3}{2}}L\Omega(z_0)} \text{ when } \Delta = \sqrt{2}\Omega \tag{3.34}$$

When z_0 is closer to L, $\Omega(z_0)$ will increase and Υ_{max} will decrease. Also, a smaller $|\dot{g}_2(z_0)|$ gives rise to a more diminutive Υ_{max}. Since a small $|\dot{g}_2(z_0)|$ indicates a smooth gap change at the end of mode-evolution region, $\ddot{g}_2(z) \geq 0$ is preferred than $\ddot{g}_2(z) \leq 0$.

In summary, the derived conditions for width and separation tapering functions are:

$$\dot{w}_{\text{diff}}(z) < 0, \;\; \ddot{w}_{\text{diff}}(z) \geq 0 \tag{3.35a}$$

$$\dot{g}_2(z) < 0, \;\; \ddot{g}_2(z) \geq 0 \tag{3.35b}$$

3.2.3 Numerical simulation

As can be seen from Section 3.2.2, when ignoring the width change and considering the gap change, Υ_{max} occurs in the middle of the mode-evolution process, breaking the adiabaticity of the device. Therefore, gap change would be more likely to introduce XTs than the width change. Thus, the gap change is explored first. We choose three commonly used functions for the gap change: linear, quadratic, and exponential functions for Region III, named Type A-C, respectively. All of the Type A-C designs use linear width functions. After comparing the performance of the Type A-C designs, we pick the best gap function among the Type A-C designs, and we use this function for Type D. The exponential width function is used for Type D to compare the influence of width change. The complex tapering functions are summarized in Table. 3.2.

For the purpose of comparison, we set $g_2(0) = 500$ nm, $g_2(L) = 100$ nm, $w_1(0) = 550$ nm, $w_2(0) = 350$ nm, $w_1(L) = w_2(L) = 450$ nm, and $L = 150$ μm. Figure 3.17 presents the coupling strength Ω and average propagation constants Δ along the propagation direction. Since the waveguide width tapering functions are the same for the Type A-C designs, their

Table 3.2 Waveguide width and separation functions in Region III [3] (© 2021 IEEE)

Linear width	$(w_i(L) - w_i(0))/L \times z + w_i(0)$, i=1 or 2
Exponential width	$w_i(0)\exp(\ln(w_i(L)/w_i(0)) \times z/L)$, i=1 or 2
Linear gap	$(g_2(L) - g_2(0))/L \times z + g_2(0)$
Exponential gap	$g_2(0) \times \exp(\ln(g_2(L)/g_2(0)) \times z/L)$
Quadratic gap	$(g_2(0) - g_2(L)) \times z^2/L^2$ $-2 \times (g_2(0) - g_2(L)) \times z/L + g_2(0)$

Δ values are the same. Among the Type A-C designs, the coupling strength Ω of the Type C design is the strongest and the Type A design is the weakest along the propagation region. With higher coupling strength at the left end of Region III, the device would be able to realize more power transfer when there are less XTs. Next, the values in Fig. 3.17 are inserted into Eqn. 3.21 to plot the adiabaticity along the transmission direction, as shown in Fig. 3.18. When $z = 0 - 100$ µm, Υ is negligible so we only present Υ when $z = 100 - 150$ µm. Among the Type A-C designs, the Type C design has the lowest maximum, and its maximum is closest to the end of the device. Considering both Ω and Υ among the Type A-C designs, the designed 3-dB OAC with the quadratic gap (Type C design) would be able to realize the least SR imbalance with the shortest length. Thus, we choose the quadratic gap function for the Type D design. Similarly, Δ, Ω, and Υ are plotted for the Typed D design in Figs. 3.17 and 3.18. Since the width change of the Type C and D designs are very similar and use the same gap tapering function, their Δ and Ω are very close to each other. As for Υ, the maximum of the Type D design is lower than the Type C design and closer to the end. Thus, the Type D design should provide a smaller SR imbalance than the Type C design. In the next Section, the SRs of the fabricated devices will be compared.

3.2.4 Fabrication and experiment results

The designed devices were patterned by electron beam lithography in a commercial foundry. The silicon waveguide has a thickness of 220 nm, and the wafer has a buffer oxide layer of 2 µm thickness and a substrate of 675 µm thickness. The rest of the experimental setup is the same as described in Section 3.1.4. The extracted SRs for the designed 3-dB OACs are plotted in Fig 3.19 and summarized in Table 3.3. Compared to the Type A design, the

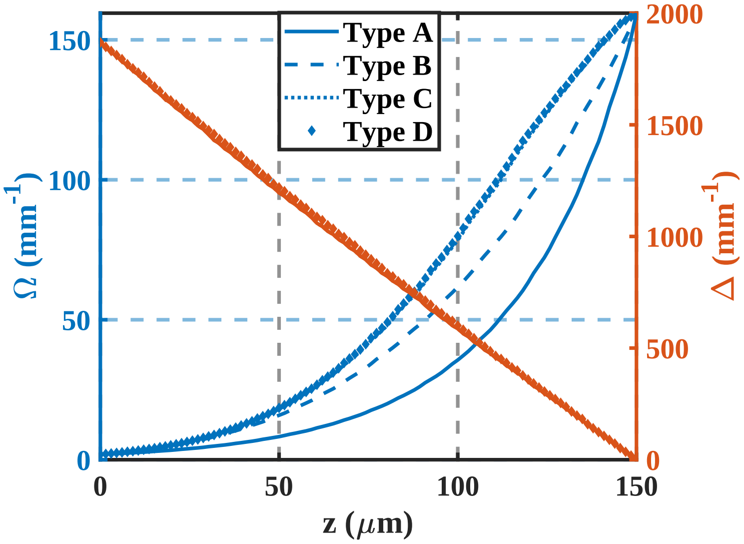

Fig. 3.17 Simulated coupling strength Ω and average propagation constant difference Δ as functions of z. [3] (© 2021 IEEE)

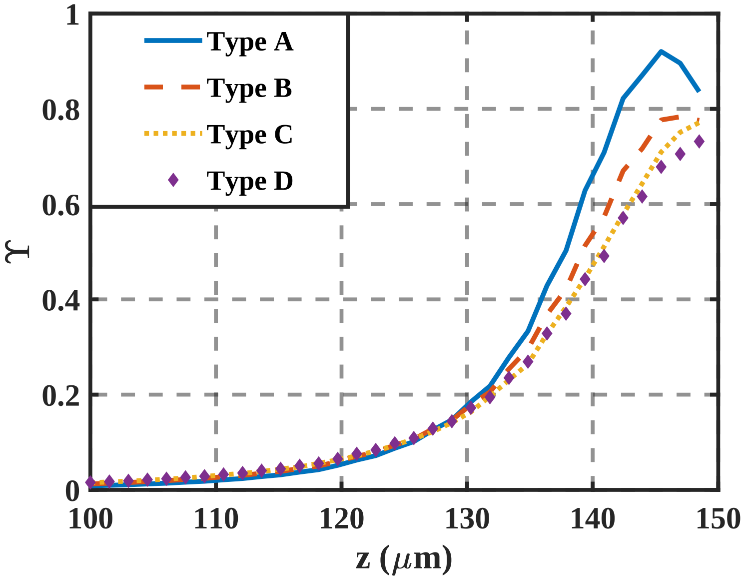

Fig. 3.18 Simulated Hamiltonian matrix element ϒ as functions of z. [3] (© 2021 IEEE)

Type B design has a minor SR imbalance with the same mode-evolution length. Compared to the Type B design with 120 µm, the Type C design has better performance with $L = 110$ µm. Thus, the quadratic gap gives the slightest imbalance with the shortest length, while the linear gap is the opposite. The Type D design has a minor SR imbalance with the same mode-evolution length as the Type C design. Therefore, this proves that exponential width change would improve the performance further.

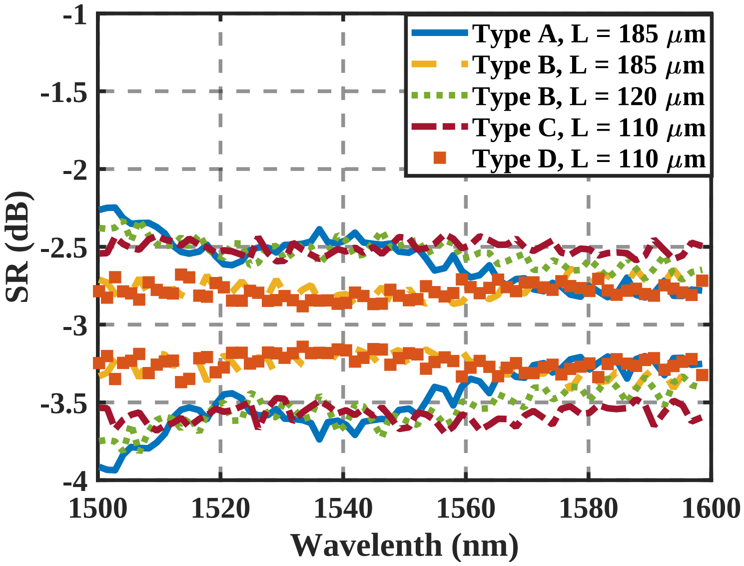

Fig. 3.19 Measured SRs for the designed 3-dB OACs. [3] (© 2021 IEEE)

Table 3.3 A summary of the experiment results for the designed 3-dB OACs [3] (© 2021 IEEE)

Design	Width	Gap	L (µm)	Imbalance (dB)
Type A	Linear	Linear	185	3±0.76
Type B	Linear	Exponential	185	3±0.37
Type B	Linear	Exponential	120	3±0.68
Type C	Linear	Quadratic	110	3±0.59
Type D	Exponential	Quadratic	110	3±0.33

Next, we use the optimized tapering function to design OACs with different SRs by varying the waveguide width difference $w_{\text{diff}}(L)$ at the end of Region III. As illustrated in

Section 3.1, the SRs are calculated as a function of waveguide width differences. The same method is used to plot the calculated SRs at 1550 nm in Fig. 3.20. The measured SRs at 1550 nm when $w_{\text{diff}}(L)$ is varied from 0 nm to 60 nm every 5 nm are also displayed in Fig. 3.20. The horizontal error bar indicates the SRs for the device when the wavelength is swept from 1500 nm to 1600 nm. When $w_{\text{diff}}(L) \geq 40$ nm, the SRs deviates from the theoretical values. The deviation can be explained as follows. Firstly, the MZI test structure is not the best way to test imbalanced OACs. As the imbalance level increases, the ER extracted from the MZI spectrum decreases, which the fluctuation of the GCs can influence. Secondly, the device performance can be influenced by the fabrication accuracy. The SR is directly related to $w_{\text{diff}}(L)$. A slightly different $w_{\text{diff}}(L)$ would make the measured SRs deviate from the theoretical values. Also, it is noteworthy that the SR variances are larger when $w_{\text{diff}}(L) = 15$ - 30 nm. The SR variances increase among this range can also be explained from two perspectives. The first reason is based on the working theory of the imbalanced OAC design. Since the SR is closely related to the effective index difference of the constituent output waveguides at Region III, which is wavelength sensitive, the SR as a function of $w_{\text{diff}}(L)$ is also wavelength sensitive. The second reason is related to the MZI test structures. With a smaller ER, the variance of the devices with $w_{\text{diff}}(L) \leq 30$ nm may be added by the variance of the GCs. However, when the ER keeps decreasing, the influence of the GC may not be reflected. Therefore, the fluctuation is decreased when $w_{\text{diff}}(L) \geq 30$ nm.

3.3 Conclusion

Section 3.1 have experimentally demonstrated the OACs with controllable SRs in the SOI platform operating over a broad wavelength range in the O-band for TE-polarization. The OACs with SRs from 7%/93% to 50%/50% have been demonstrated in this paper. We use the exponential function to fit the data calculated from the experiment. At center wavelength, the deviations of the SRs from the experimental data curve fit are within 6.1%, 2.8%, and 6.5% for semi-analytical representation, simulations, and experiment, respectively. Therefore, the exponential function calculated from experimental data can be used as an empirical formula to realize OACs with arbitrary SRs without going through the prototyping process. The thermal property is also explored for the proposed devices. For the simulation, the device temperature is increased from 0°C to 100°C. For the experi-

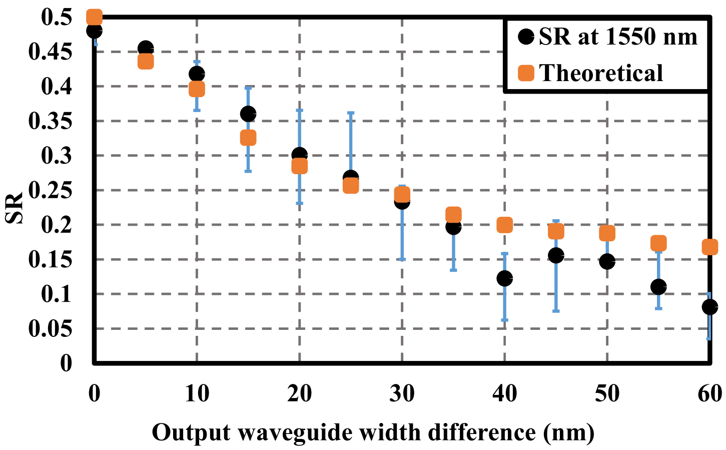

Fig. 3.20 Measured SRs for the imbalanced OACs (black circle). Orange squares denotes the theoretical SRs calculated at 1550 nm.. [3] (© 2021 IEEE)

ment, the stage temperature is increased from 20°C to 50°C. The maximum variations of the SRs for different wavelengths over the entire O-band are 1.6% and 1.3% for simulation and experiment, respectively. The OACs are proven to be resistant to volatile temperature fluctuations.

Section 3.2 analytically and experimentally demonstrate an efficient method to improve the performance of the OACs. A quantitative study to evaluate the mode-evolution process is proposed for the OACs. By analytically studying the influence of waveguide width and gap tapering functions, we derive necessary constraints for the mode-evolution functions to optimize the performance. Then, we compare four different types of mode-evolving functions. We theoretically and experimentally prove that the quadratic separation and exponentially varying width would bear the most negligible SR imbalance for the designed 3-dB OAC with the shortest length. The measured SRs of the designed 3-dB OAC using the optimized tapering function are within 47%/53% from 1500 nm to 1600 nm. Lastly, the optimized tapering function is used to realize OACs with different SRs from 8%/92% to 42%/58%.

Chapter 4

CMOS-compatible and Temperature Insensitive C-band Wavelength (de-)Multiplexer

Based on the background presented in Sections 2.2.1 and 2.3, this Chapter reports the design, simulation, and experimental results of a CMOS-compatible and temperature insensitive C-band wavelength (de-)MUX. Section 4.1 briefly introduces the content of this Chapter. Section 4.2 gives the design methodology and simulation results. Section 4.3 presents the important figure-of-merits (FOMs) for the proposed (de-)MUXs at different temperatures. Section 4.4 concludes this Chapter. This Chapter is based on the author's work in [2].

4.1 Introduction

In this work, we propose and demonstrate a 1×4 C-band MZI-based MUX on the SOI platform with low thermal sensitivity and can be easily modified for O-band Coarse WDM (CWDM) operation. Waveguides with different widths are employed in the delay lines to balance the overall TOC. Compact and broadband MMI couplers are utilized in the design. Another MZI-based MUX with uniform delay lines is also demonstrated for comparison. The transmission spectra for both devices are measured from 1500 nm to 1600 nm when the temperature is varied from 293.15 K to 323.15 K. Compared to the reference MUX with a TOC of 85.36 pm/K, the measured TOC of the proposed device is 4.8 pm/K. For the reference device under various temperatures, the ILs and signal XTs degrade from ∼1 dB to ∼8 dB and from ∼30 dB to ∼25 dB, respectively. For the proposed device under the same temperature changes, the ILs and XTs remain ∼2 dB and ∼20 dB, respectively.

4.2 Design and simulation

The schematic of the paired-interference-based MMI coupler used in the MUXs is displayed in Fig. 4.1 [74]. The MMI coupler consists of two input/output tapers and a multi-mode waveguide. The critical parameters labeled in Fig. 4.1 are multi-mode waveguide width $w_{\mathrm{MMI}} = 4.5$ µm and length $l_{\mathrm{MMI}} = 24$ µm, taper width $w_{\mathrm{t}} = 1$ µm, and input/output waveguide width $w_{\mathrm{in}} = 0.5$ µm. These parameters are calculated based on the theory introduced in Section 2.2.1. The MMI coupler is characterized by the SRs and ILs which are defined as follows:

$$SR = 10\log_{10}(\frac{P_{\mathrm{O1}}}{P_{\mathrm{O1}} + P_{\mathrm{O2}}}) \tag{4.1a}$$

$$IL = 10\log_{10}(P_{\mathrm{O1}} + P_{\mathrm{O2}}) \tag{4.1b}$$

where P_{O1} and P_{O2} are the power at output 1 and output 2 of the MMI coupler, respectively. The simulated SRs and ILs at different temperatures are displayed in Figs. 4.2 and 4.3, respectively. For ∼30 K temperature change, the variations of both SRs and ILs are within 0.1 dB, implying the excellent thermal stability of the proposed MMI coupler.

The schematic of the reference MUX containing three MZI stages with uniform delay paths is shown in Fig. 4.4. For each stage, the waveguide width of the delay path is 450 nm for single-mode operation. With FSR being 10 nm, the lengths of the delay paths for each stage ΔL_1, $\Delta L_{2\mathrm{a}}$, and $\Delta L_{2\mathrm{b}}$ are chosen to be 28.126 µm, 14.228 µm, and 14.393 µm, respectively [39]. Considering both the dispersion and thermal-optic properties of the waveguides and the MMI couplers, the transmission spectra of the device are calculated by taking the S-parameters of the simulated MMI coupler into the transfer matrix for each MZI stage:

$$E_{\mathrm{out}} = \begin{bmatrix} S_{31} & S_{32} \\ S_{41} & S_{42} \end{bmatrix} \cdot \begin{bmatrix} e^{\frac{-j\cdot 2\pi n_{\mathrm{eff}}(\lambda,T)\cdot \Delta L_{ST}}{\lambda}} & 0 \\ 0 & 1 \end{bmatrix} \cdot \begin{bmatrix} S_{31} & S_{32} \\ S_{41} & S_{42} \end{bmatrix} \tag{4.2}$$

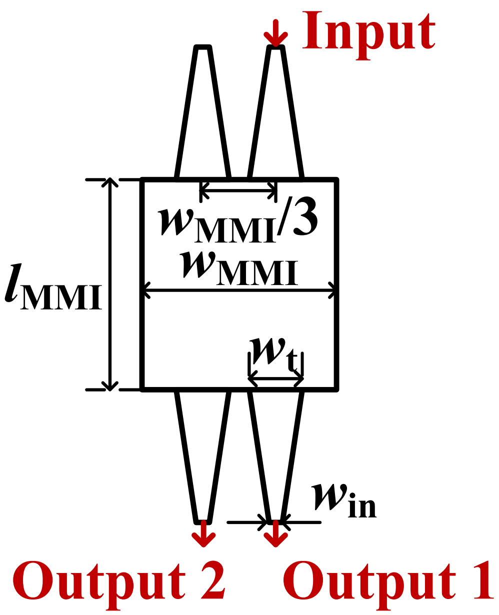

Fig. 4.1 Schematic of the MMI coupler. [2] (© 2022 IEEE)

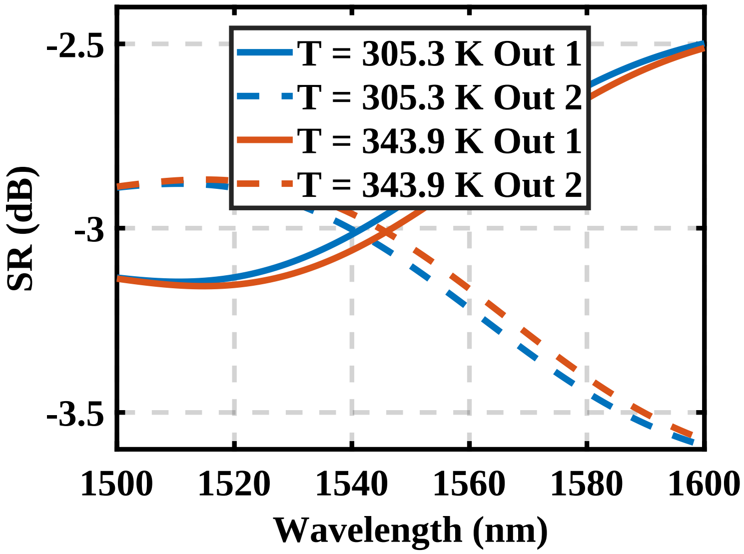

Fig. 4.2 The SRs as functions of wavelength for the proposed MMI coupler at different temperatures. [2] (© 2022 IEEE)

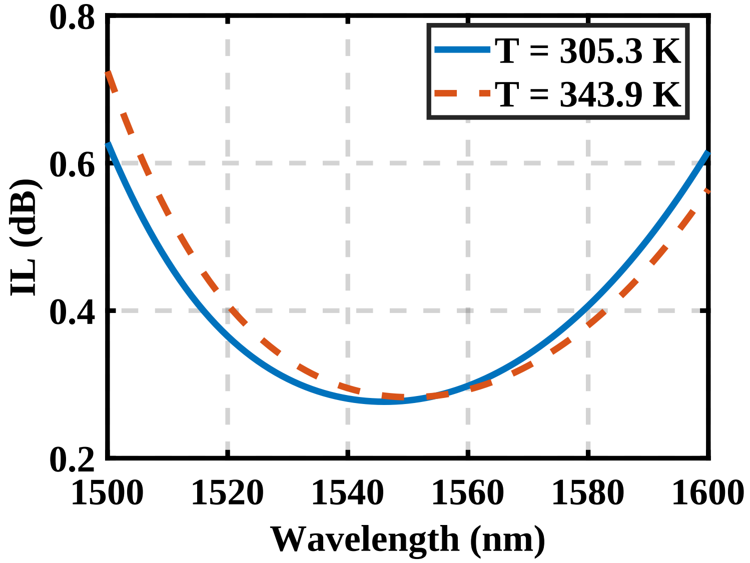

Fig. 4.3 The ILs as functions of wavelength for the proposed MMI coupler at different temperatures. [2] (© 2022 IEEE)

where $ST = 1$, 2a, or 2b, S_{ij} is the calculated S-parameter of the MMI coupler ($i = 3, 4$, $j = 1, 2$), and $n_{\text{eff}}(\lambda, T)$ is the waveguide effective index as a function of both wavelength and temperature. The calculated transmission spectra at different temperatures are illustrated in Fig. 4.5. Based on the transmission spectra, the center wavelength is defined as the wavelength where the local maximum is achieved per channel. The IL and XT are determined for each center wavelength. The calculated center wavelengths, ILs, and XTs for the four output channels are summarized in Table 4.1. The simulation results confirm that the temperature variation mainly affects the center wavelengths of the MUX. The TOC of the simulated device is 68.9 pm/K. The ILs of the multiplexer mainly come from the MMI couplers.

The schematic of the proposed device is displayed in Fig. 4.6 and consists of three MZI stages with nonuniform delay paths. For each stage, the longer delay path is composed of two segments of waveguides with widths w_1 and w_2, lengths dL_{ST} and L_{ST}, respectively ($ST = 1, 2\text{a}, 2\text{b}$). The shorter delay path comprises one segment of uniform waveguide with width w_1 and length L_{ST}. Since the calculation method to determine the lengths of delay paths for each stage is the same, the detailed process is only demonstrated for the first stage.

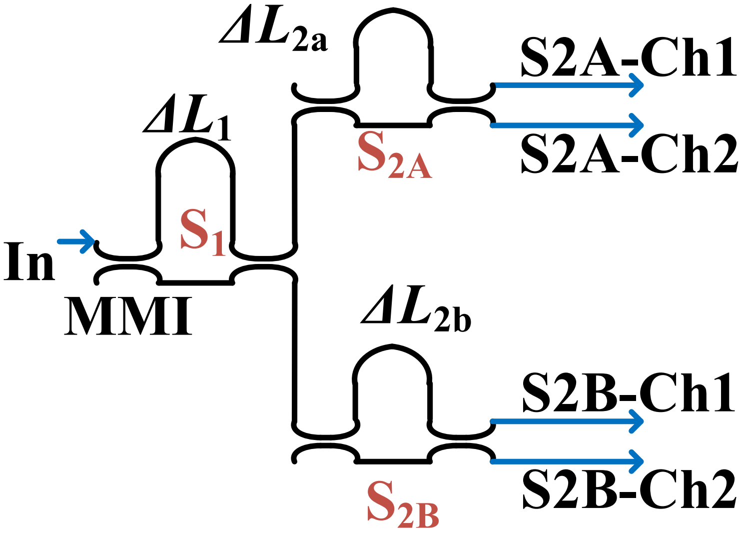

Fig. 4.4 Schematic of the wavelength MUX without thermal stability design. [2] (© 2022 IEEE)

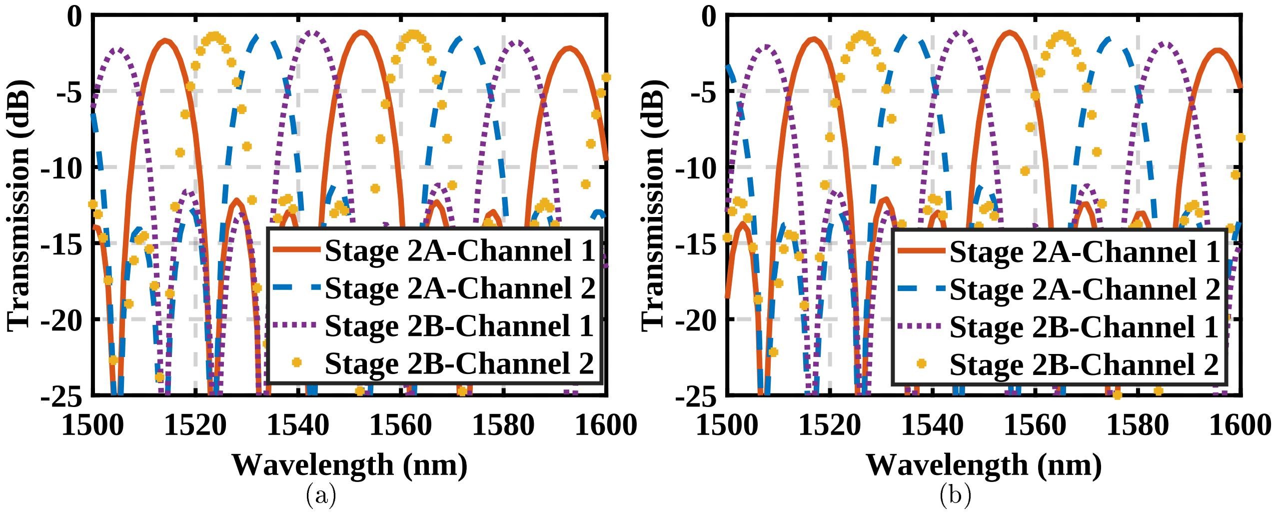

(a) (b)

Fig. 4.5 Transmission spectra of the reference design in Fig. 4.4 at (a) 307.1 K and (b) 342.7 K. [2] (© 2022 IEEE)

Table 4.1 Summary of the Simulation results for the design in Fig. 4.4 [2] (© 2022 IEEE)

T = 307.1 K			T = 342.7 K		
WL (nm)	IL (dB)	XT (dB)	WL (nm)	IL (dB)	XT (dB)
1514	1.68	32	1517	1.59	26
1524	1.4	32	1526	1.32	35
1533	1.19	36	1536	1.17	47
1543	1.12	53	1545	1.13	33

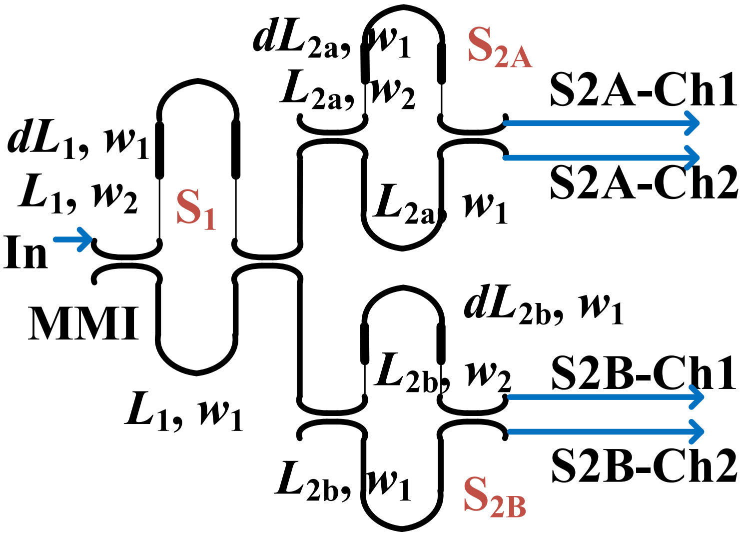

Fig. 4.6 Schematic of the wavelength MUX with thermal stability design. [2] (© 2022 IEEE)

The interference for the first stage is expressed as follows [149]:

$$\begin{aligned} m\lambda = {} & n_{\mathrm{eff}}(w_1, \lambda, T) \cdot dL_1 \\ & + [n_{\mathrm{eff}}(w_2, \lambda, T) - n_{\mathrm{eff}}(w_1, \lambda, T)] \cdot L_1 \end{aligned} \tag{4.3}$$

where m is a half-integer or integer and $n_{\mathrm{eff}}(w_k, \lambda, T)$ $(k = 1, 2)$ is the effective index for the waveguide of width w_k as a function of both wavelength and temperature. Differentiating both sides of Eqn. 4.3 with respect to λ, we can get a modified expression M for m as the following:

$$\begin{aligned} M = {} & m - dL_1 \frac{\partial n_{\mathrm{eff}}(w_1, \lambda, T)}{\partial \lambda} \\ & - L_1 \frac{\partial [n_{\mathrm{eff}}(w_2, \lambda, T) - n_{\mathrm{eff}}(w_1, \lambda, T)]}{\partial \lambda} \end{aligned} \tag{4.4}$$

Considering the dispersion effect as shown in Eqn. 4.4, the TOC $\frac{\mathrm{d}\lambda}{\mathrm{d}T}$ of the first stage is calculated by taking the partial derivative of Eqn. 4.3 with respect to the temperature:

$$\begin{aligned} \frac{\mathrm{d}\lambda}{\mathrm{d}T} = {} & \frac{dL_1}{M} \frac{\partial n_{\mathrm{eff}}(w_1, \lambda, T)}{\partial T} \\ & + \frac{L_1}{M} \frac{\partial [n_{\mathrm{eff}}(w_2, \lambda, T) - n_{\mathrm{eff}}(w_1, \lambda, T)]}{\partial T} \end{aligned} \tag{4.5}$$

The FSR of the first stage can be approximated as such:

$$FSR = \frac{\lambda^2}{n_{\mathrm{g}}(w_1, \lambda, T) dL_1 + \Delta n_{\mathrm{g}} L_1} \tag{4.6}$$

where $\Delta n_{\mathrm{g}} = n_{\mathrm{g}}(w_2, \lambda, T) - n_{\mathrm{g}}(w_1, \lambda, T)$, and $n_{\mathrm{g}}(w_k, \lambda, T)$ $(k = 1, 2)$ is the group index for the waveguide of width w_k. To achieve the athermal condition ($\frac{\mathrm{d}\lambda}{\mathrm{d}T} = 0$) for the first stage, dL_1 and L_1 are derived from Eqns. 4.5 and 4.6 and expressed as the following:

$$dL_1 = \frac{\lambda^2}{FSR[n_{\mathrm{g}}(w_1, \lambda, T) - \Delta n_{\mathrm{g}}(\frac{\frac{\partial n_{\mathrm{eff}}(w_1, \lambda, T)}{\partial T}}{\frac{\partial n_{\mathrm{eff}}(w_2, \lambda, T)}{\partial T} - \frac{\partial n_{\mathrm{eff}}(w_1, \lambda, T)}{\partial T}})]} \tag{4.7a}$$

$$L_1 = \frac{\partial n_{\mathrm{eff}}(w_1, \lambda, T)/\partial T}{\partial [n_{\mathrm{eff}}(w_1, \lambda, T) - n_{\mathrm{eff}}(w_2, \lambda, T)]/\partial T} \tag{4.7b}$$

Equations 4.7a and 4.7b show that both dL_1 and L_1 are directly dependent on the waveguide properties. Thus, it is crucial to determine the values for w_1 and w_2 in order to calculate dL_1 and L_1.

To specify the values for w_1 and w_2 so that $\frac{\mathrm{d}\lambda}{\mathrm{d}T} = 0$, the thermal dependence of the effective index with respect to waveguide widths is plotted in Fig. 4.7 by using Ansys Lumerical MODE and HEAT solvers. As illustrated in the Fig. 4.7, with $\frac{\partial n_{\text{eff}}}{\partial T}$ being positive for the calculated waveguide widths, the first term in Eqn. 4.5 remains positive. Therefore, the second term of Eqn. 4.5 has to be negative to make sure $\frac{\mathrm{d}\lambda}{\mathrm{d}T} = 0$, implying w_1 and w_2 have to be chosen such that the following condition is satisfied:

$$\frac{\partial n_{\text{eff}}(w_2, \lambda, T)}{\partial T} < \frac{\partial n_{\text{eff}}(w_1, \lambda, T)}{\partial T} \tag{4.8}$$

Also, to limit the footprint of the multiplexer, w_1 is set to be 500 nm where $\frac{\partial n_{\text{eff}}(w,\lambda,T)}{\partial T}$ is close to the maxima. Then, dL_1 and L_1 are only dependent on w_2 and are plotted in Fig. 4.8. To ensure a compact footprint, we set the following conditions for the delay lengths:

$$0 < dL_1, L_1 \leq 250 \ \mu\text{m} \tag{4.9}$$

Additionally, to ensure that the optical loss caused by the narrow waveguide is negligible, w_2 should be no less than 350 nm. To satisfy the conditions above, w_2 is set as 350 nm. After determining the values for w_1 and w_2, dL_1 is calculated as 15.803 µm based on Eqn. 4.7a. Then, the TOC ($\frac{\mathrm{d}\lambda}{\mathrm{d}T}$) is plotted as a function of L_1 in Fig. 4.9. Taking the fabrication error into account, $\frac{\mathrm{d}\lambda}{\mathrm{d}T}$ is also computed when the waveguide widths are varied by ± 20 nm. As can be seen, the maximum TOC is 26 pm/K when $L_1 = 237.629$ µm considering ± 20 nm width and length error. Thus, such a design is reliable even with ± 20 nm fabrication error in both waveguide width and length. Similarly, dL_2, L_2, dL_3, and L_3 are calculated to be 8.059 µm, 118.814 µm, 8.217 µm, and 118.814 µm, respectively. Then, the transmission spectra of the multiplexer are calculated by multiplying the transfer matrix of each stage:

$$E_{\text{out}} = \begin{bmatrix} S_{31} & S_{32} \\ S_{41} & S_{42} \end{bmatrix} \cdot \begin{bmatrix} e^{\frac{-j\phi_1}{\lambda}} & 0 \\ 0 & e^{\frac{-j\phi_2}{\lambda}} \end{bmatrix} \cdot \begin{bmatrix} S_{31} & S_{32} \\ S_{41} & S_{42} \end{bmatrix} \tag{4.10a}$$

$$\phi_1 = 2\pi \cdot n_{\text{eff}}(w_1, \lambda, T) \cdot dL_{ST} + n_{\text{eff}}(w_2, \lambda, T) \cdot L_{ST} \tag{4.10b}$$

$$\phi_2 = 2\pi \cdot n_{\text{eff}}(w_1, \lambda, T) \cdot L_{ST}, ST = 1, 2\text{a}, 2\text{b} \tag{4.10c}$$

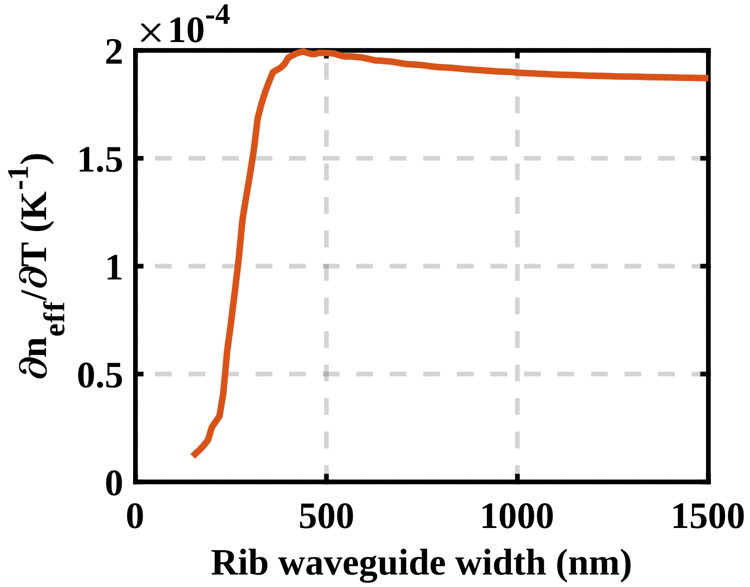

Fig. 4.7 Thermal-optic property of the effective index as a function of width. [2] (© 2022 IEEE)

The calculated results at different temperatures are plotted in Fig. 4.10 and summarized in Table 4.2. Compared to the reference device with a TOC of 68.9 pm/K, the calculated TOC is 5 pm/K. The ILs and XTs of the proposed device are ∼2 dB and ∼20 dB, respectively. Compared to the reference device, ILs increase by 1 dB while the XTs decrease by 5 dB. The degradation in ILs and XTs is caused by slightly compromised phase-matching condition for the proposed delay paths, indicating a trade-off between thermal stability and ILs/XTs.

Table 4.2 Summary of the Simulation results for the design in Fig. 4.6 [2] (© 2022 IEEE)

T = 307.2 K			T = 343 K		
WL (nm)	IL (dB)	XT (dB)	WL (nm)	IL (dB)	XT (dB)
1510	2.23	12	1510	2.16	11
1518	1.71	16	1519	1.73	14
1527	1.48	14	1527	1.47	16
1536	1.34	16	1536	1.34	17

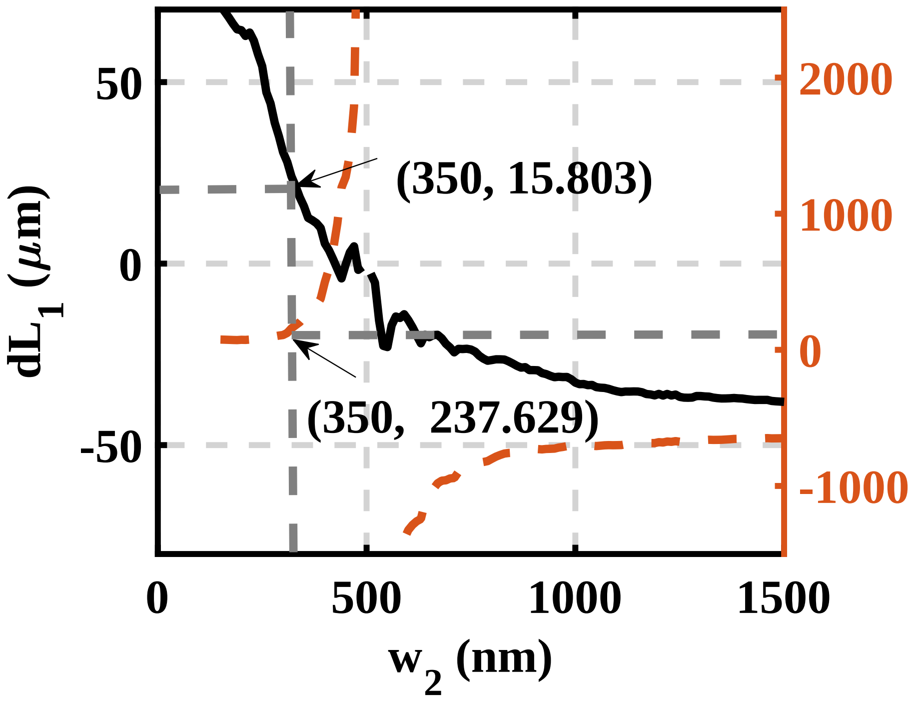

Fig. 4.8 dL_1 and L_1 as functions of w_2. [2] (© 2022 IEEE)

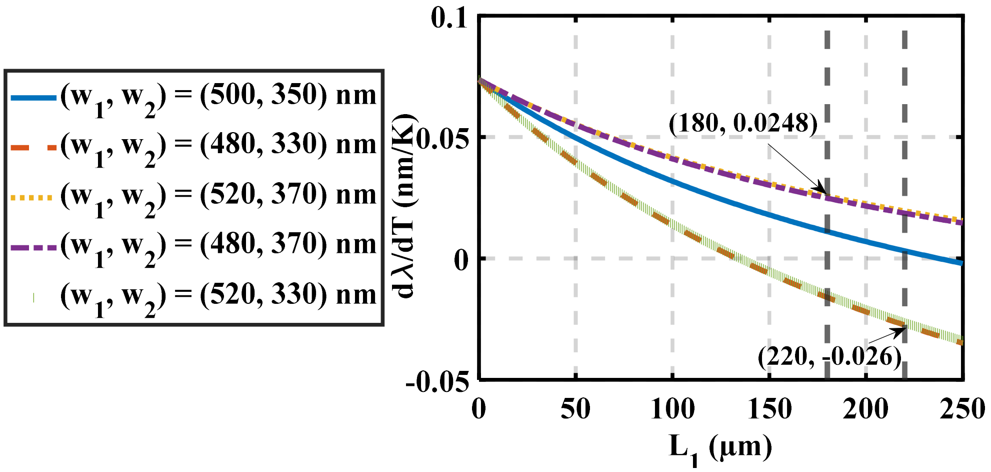

Fig. 4.9 $\frac{d\lambda}{dT}$ as a function of L_1 for different (w_1, w_2). [2] (© 2022 IEEE)

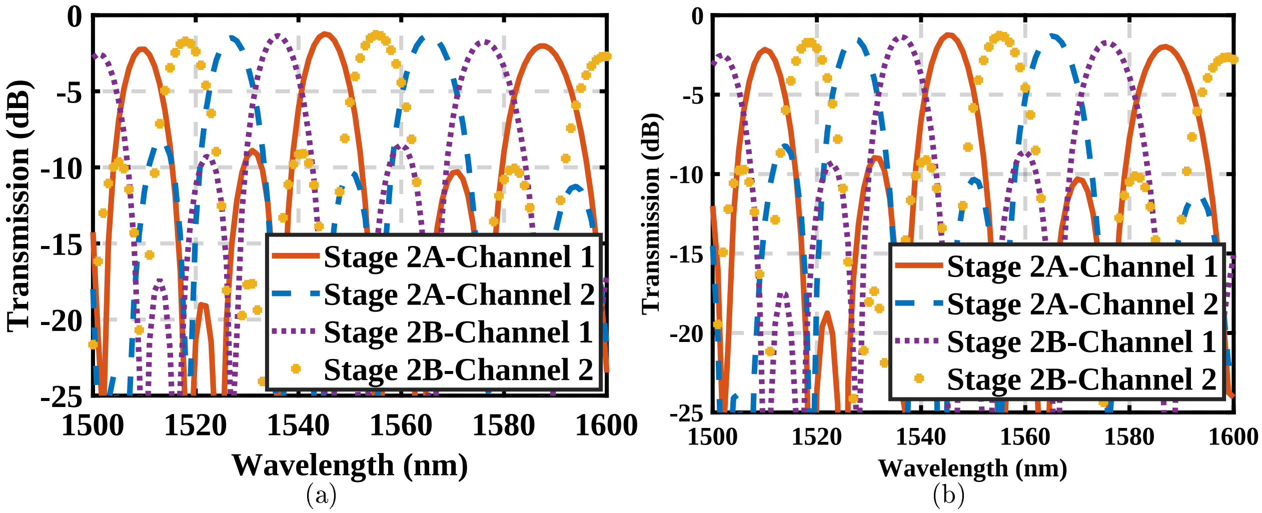

(a)

(b)

Fig. 4.10 Transmission spectra of the proposed design in Fig. 4.6 at (a) 307.2 K and (b) 343 K. [2] (© 2022 IEEE)

4.3 Fabrication and experimental results

The devices were patterned using electron beam lithography by Applied Nanotools foundry with silicon waveguides of 220 nm thickness, a buffer oxide layer of 2 µm thickness, and a Si substrate of 675 µm thickness. The experimental setup is the same as described in Section 3.1.3. The calculated SRs of the fabricated MMI coupler are 3±0.5 dB from 1500 nm to 1600 nm, as shown in Fig. 4.11. The SR variation is within 0.5 dB when the temperature is varied from 293.15 K to 323.15 K.

The measured transmission spectra for the designs in Figs. 4.4 and 4.6 under different temperatures are presented in Fig. 4.12. The center wavelengths, ILs, and XTs for both designs are summarized in Tables 4.3 and 4.4. The wavelength shifts of the four output ports for both designs are shown in Fig. 4.13. In comparison to the reference device with a TOC of 85.36 pm/K, the proposed multiplexer has a TOC of 4.8 pm/K. The wavelength shifts are slightly different among the four output ports, as depicted in Fig. 4.13. The minor difference between among channels is because the phase-matching condition is wavelength-dependent. For both designs at 293.15 K, the ILs are mainly caused by the MMI couplers. However, when the temperature is increased by 30 K, the ILs surge to ~6.5 dB for the reference design while the ILs remains the same level for the proposed one. The worsened ILs are attributed

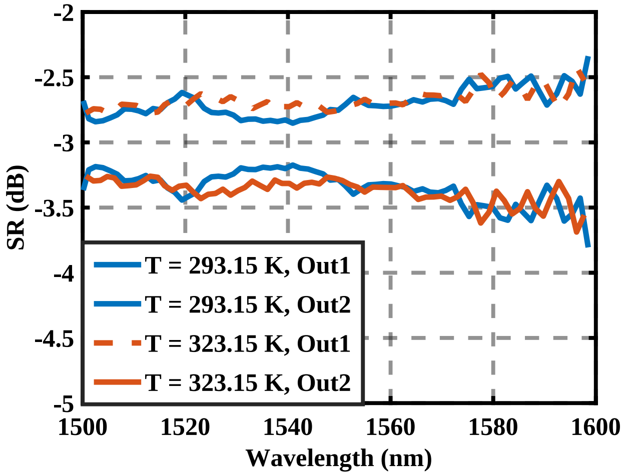

Fig. 4.11 Measured SRs of the fabricated MMI coupler at different temperatures.

to the additional phase noises introduced by the side-wall roughness together with the SR imbalance of the MMI couplers under severe temperatures. The XTs for the reference and proposed designs at different temperatures are ~25 dB and ~20 dB, respectively, implying a trade-off between thermal stability and interference. Low interference from neighboring channels, corresponding to high XT, is achieved with the perfect π phase difference between the targeted channel and neighboring channels. However, for the proposed device, a perfect π phase shift is more difficult to realize given the designed delay paths compared to the reference device, resulting in a lower XTs.

Comparing with the state-of-the-art MZI-based WDM devices summarized in Table 4.5, the proposed device in this work demonstrates extraordinary thermal stability across the

Table 4.3 Summary of the experiment results for the design in Fig. 4.4 [2] (© 2022 IEEE)

293.15 K			323.15 K		
WL (nm)	IL (dB)	XT (dB)	WL (nm)	IL (dB)	XT (dB)
1512.47	1.28	28	1514.71	7.62	26
1521.64	1.35	30	1524.22	7.22	25
1531.39	0.46	38	1534.08	6.74	34
1540.38	1.07	28	1543.10	7.93	22

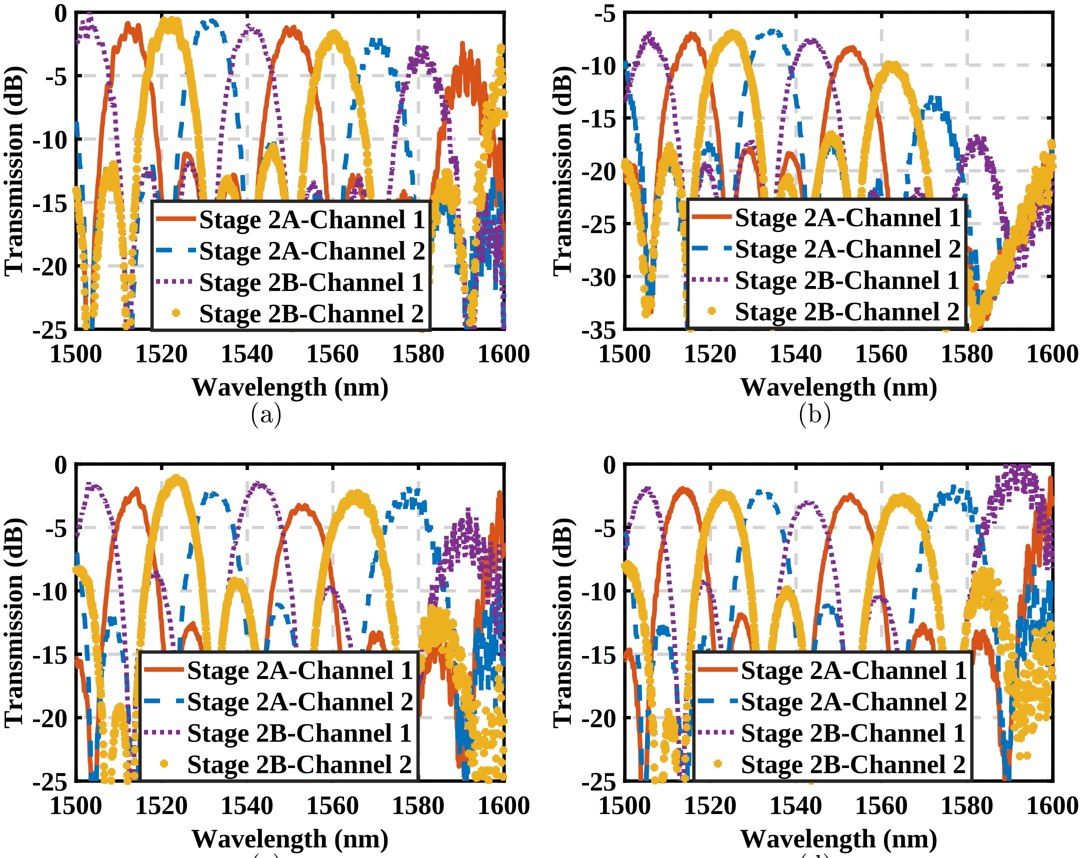

(a) (b) (c) (d)

Fig. 4.12 Measured transmission spectra for the reference device at (a) 293.15 K and (b) 323.15 K; for the proposed device at (c) 293.15 K and (d) 323.15 K. [2] (© 2022 IEEE)

Table 4.4 Summary of the experiment results for the design in Fig. 4.6 [2] (© 2022 IEEE)

293.15 K			323.15 K		
WL (nm)	IL (dB)	XT (dB)	WL (nm)	IL (dB)	XT (dB)
1513.19	2.33	25	1513.63	2.13	24
1523.62	1.28	17	1523.60	2.49	16
1532.36	2.39	18	1532.50	2.11	30
1543.30	1.85	18	1542.96	2.97	17

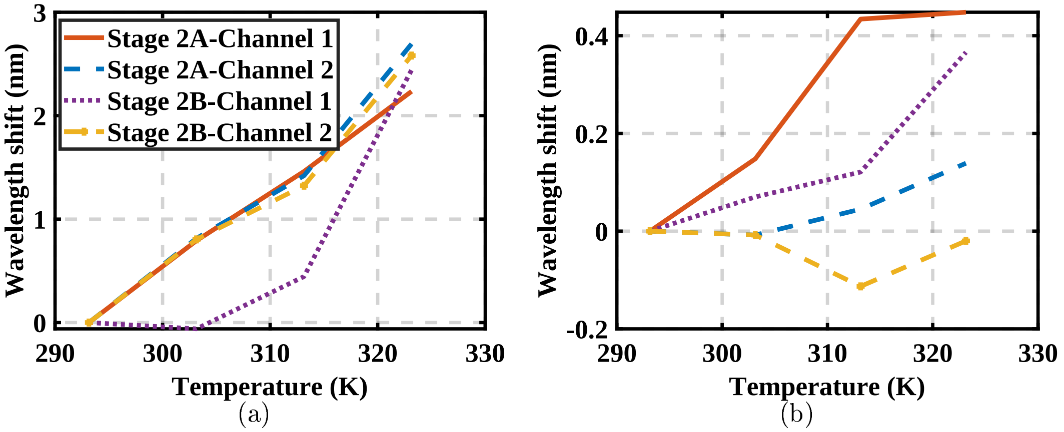

Fig. 4.13 Calculated TOCs for (a) reference and (b) proposed MUXs. [2] (© 2022 IEEE)

100 nm wavelength range. The ILs and XTs could be improved by further optimizing the MMI couplers. To be specific, the SR deviation over the C-band is mainly due to the output tapers being closer to each other. The ILs are mostly attributed to the small taper width W_t. Therefore, reduced SR deviation and ILs could be achieved with larger multi-mode waveguide width, allowing wider output taper separation and widths.

Table 4.5 Experimental Results of various MZI-based WDM designs [2] (© 2022 IEEE)

Ref.	WG	Band/FSR	$\mathrm{BW}_{1\mathrm{dB}}$	IL (dB)	XT (dB)	TOC (pm/K)
[39]	Si 220 nm	C/5 nm	3 nm	1.6	15	NA
[41]	Si 340 nm	O/3.2 nm	NA	0.5-2.0	15-20	NA
[40]	Si 220 nm	O/20 nm	16 nm	1.0	20	NA
[149]	Si 220 nm	O/5 nm	NA	4	15	17
[145]	SiN 340 nm	O/20 nm	13 nm	1.61-1.75	20.04-25.01	18.5
This work	**Si 220 nm**	**C/10 nm**	**4.56 nm**	**1.9-3.42**	**14.85-41.33**	**4.8**

4.4 Conclusion

This Section demonstrates a CMOS-compatible 1×4 C-band MZI-based wavelength multiplexer with remarkable thermal stability. The TOC is as low as 4.8 pm/K thermally stable MMI couplers and the matched waveguide widths in the delay lines. Considering the data center application where the temperature fluctuates from 283.15 K to 343.15 K [204], the proposed design would introduce only a 0.29 nm wavelength shift. With the temperature increasing from 293.15 K to 323.15 K, the measured ILs and XTs of the proposed device are $\sim$2 dB and $\sim$20 dB, respectively. With the ILs and SR imbalance of the MMI couplers being further decreased, this work demonstrates that such a MUX with robust thermal stability is power-efficient and suitable for data center applications.

Chapter 5

Compact Mach-Zehnder Modulator with Meandered Phase Shifter

Building on the background described in Section 2.4, this Chapter propose a C-band Mach-Zehnder modulator with meandered phase shifters on the SOI platform, achieving low ILs and high thermal and fabrication error tolerance. Section 5.1 presents the scope of this Chapter. Section 5.2 demonstrates the device layout and the complete EO BW simulation process. This section also compares the performance of the proposed device and a TWMZM of the same active region length. Section 5.3 displays the DC and small signal measurement results. Section 5.4 gives the large signal experimental setup and results. Energy consumption is calculated and demonstrated in Section 5.5. Finally, Section 5.6 concludes this Chapter. This Chapter is established on the author's work in [1] and [5].

5.1 Introduction

In this Chapter, we demonstrate MZMs having meandering phase shifters. To simplify the driving and biasing circuitry and increase the integration density, we propose an MMZM based on the SPP driving scheme with a footprint of 432×260 μm^2 on the SOI platform. The optical IL without biasing is found to be 2.1 dB. Using a −0.5 V reverse bias, the half-wave voltage (V_π) and 3-dB EO BW are measured as 6.4 V and 7.7 GHz, respectively. Using the fabricated MMZM, we experimentally demonstrate 53 Gbaud PAM-4 transmission over 2 km distance in the C-band at a BER below the HD pre-FEC BER threshold having 6.7% overhead.

5.2 Design and simulation

5.2.1 Device layout

The schematic, the p-n junction cross-section, and the fabricated device of the proposed MMZM are displayed in Figs. 5.1-5.3, respectively. The overall footprint of the MMZM is 432×260 μm^2. The footprint reduction is realized by folding the optical waveguide in the active region. Specifically, the optical waveguide is divided into eight sections, as labelled by the green dotted square in Fig. 5.1. The waveguide is arranged in an arc shape for each section, and the total length of the optical waveguide embedded in the active region is 1.6 mm. A waveguide imbalance of 100 µm between the two MZI arms is created for convenience of DC characterization and biasing.

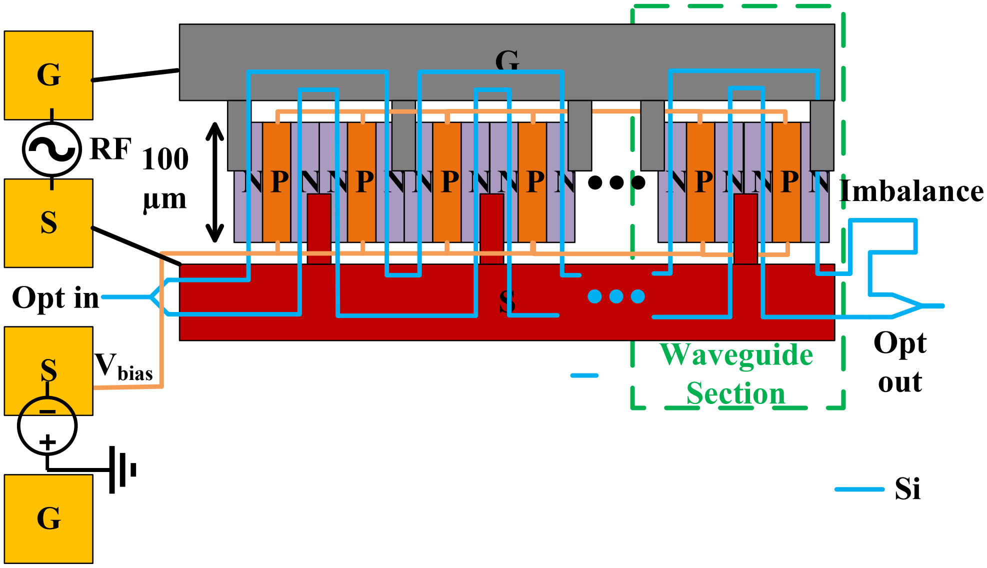

Fig. 5.1 Schematic of the meandered Mach-Zehnder Modulator (MMZM). [1] (© Optica Publishing Group.)

The p-n junctions are embedded around the optical waveguide. Figure 5.1 shows that the p-n junctions are connected B2B in the first section. The SPP structure enables a single RF driver to load the electrical signal. In the first waveguide section, the n-p-n junction shares the N++ region with the neighbouring n-p-n junction. The extended teeth from the coplanar strips (CPS) structure are used to make contact with the N++ region through two VIA layers and an intermediate metal layer. A 40 GHz, GSSG RF probe with a 125 µm pitch is used to test the modulator. The first GS tips apply the RF signal to the modulator. The second S tip applies the DC bias via the connected P++ junction. The top two pads are connected to the RF signals through the GSSG probe. The third pad is connected to the DC signal through the GSSG probe and applies the DC bias via the connected P++ junctions. The fourth pad is not connected to any terminal on the chip and is used for landing the tip of GSSG probe.

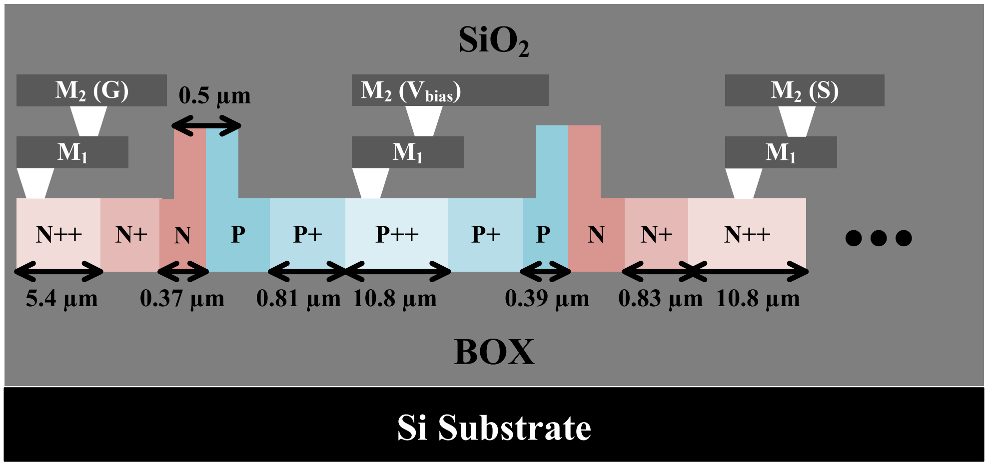

Fig. 5.2 The p-n junction cross-section of the MMZM (not to scale). [1] (© Optica Publishing Group.)

5.2.2 Electrode and p-n junction analysis

In this section, the EO BW is calculated considering the two metal layers, two VIA layers, and the p-n junctions. The metal and VIA layers, shown in Fig. 5.4, are first simulated in the Ansys high-frequency structure simulator (HFSS). The calculated S-parameter is then imported to the Keysight Advanced Design System (ADS) to extract the values for the lumped circuit model, as demonstrated in Fig. 5.5. As shown in Table 5.1, the resistance of the electrode (1 Ω) is almost negligible, suggesting that the 432 µm - electrode has an insignificant microwave (MW) loss. The inductance (227 pH) is higher than the result shown in [205]. Considering that the currents tend to concentrate at the edge of the electrode due to the skin effect, the extended teeth from the CPS structure increase the accumulated magnetic field while decreasing the gap between the electrodes. The conductance, repre-

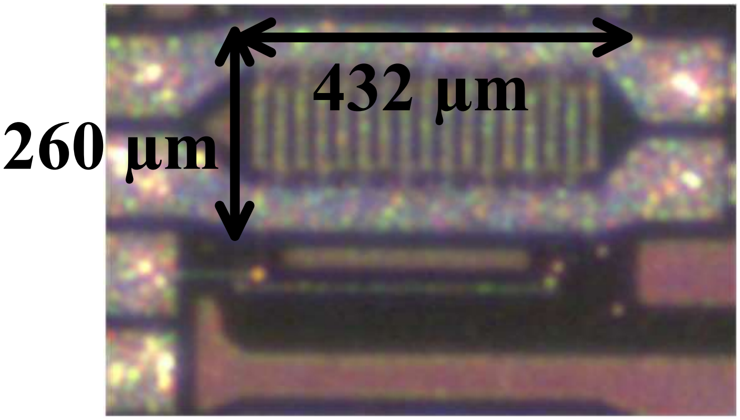

Fig. 5.3 The image of the fabricated MMZM. [1] (© Optica Publishing Group.)

senting the dielectric loss of the electrode, is also higher than the regular CPS waveguide because of the extended metal teeth.

Table 5.1 Summary of the values for the parameters in Fig. 5.5. [1] (© Optica Publishing Group.)

R_{lump}	L_{lump}	C_{lump}	$1/G_{\text{lump}}$	R_{PN}	C_{PN} (0 V)	C_{PN} (−0.5 V)	C_{PN} (−2 V)	C_{PN} (−4 V)
1 Ω	227 pH	134 fF	50 kΩ	14 Ω	216 fF	200 fF	122 fF	80 fF

The resistance and the capacitance of the p-n junction under different reverse bias voltages are calculated using the Ansys Lumerical CHARGE solver and summarized in Table 5.1. Inserting the calculated p-n junction results into the model shown in Fig. 5.5, $v_{\text{out}}/v_{\text{in}}$ is calculated for different frequencies and demonstrated in Fig. 5.6. As shown in Fig. 5.6, the 3-dB BW of the electrode without the p-n junction is much larger than 30 GHz. With the p-n junction, the 3-dB BW is decreased to 17 GHz. When using −0.5 V reverse bias, the capacitance change is slight, resulting in minor BW improvement. With a higher reverse bias voltage, the doping profile change results in a more prominent capacitance decrease. Therefore, a more obvious BW improvement is observed at a higher reverse bias voltage.

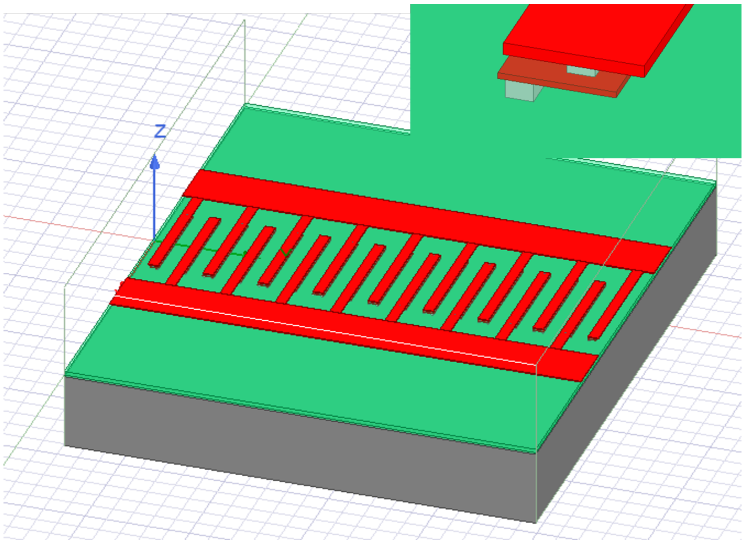

Fig. 5.4 Layout of the simulated electrode. [1] (© Optica Publishing Group.)

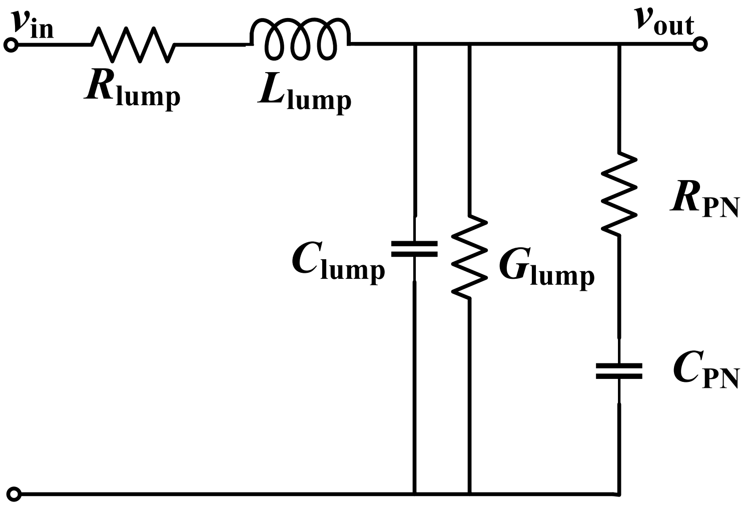

Fig. 5.5 Lumped circuit model of the MMZM. [1] (© Optica Publishing Group.)

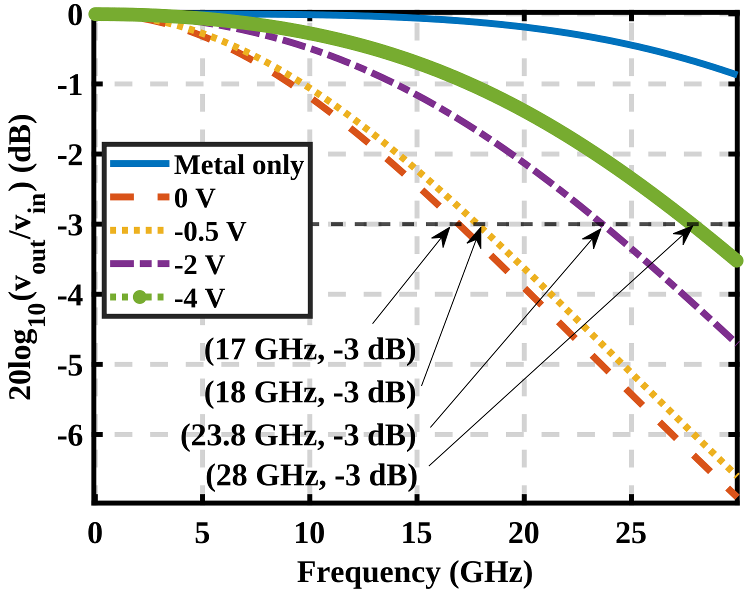

Fig. 5.6 Calculated $20\log_{10}(v_{\text{out}}/v_{\text{in}})$ as a function of frequency considering the electrode and p-n junction. [1] (© Optica Publishing Group.)

5.2.3 Optical transit time analysis

Optical transit time is another factor limiting the EO BW of lumped modulators. Since the electrode is usually less than 500 µm long, the RF signal can be considered independent of the transmission direction. Under this assumption, an optical signal travels through the waveguide and accumulates specific phase changes introduced by the RF signal. The accumulated optical phase change can be understood as the time integration of the RF signal, which varies with RF frequencies given the same optical transit time. Therefore, the following two equations are used to calculate the accumulated phase change versus different RF frequencies [46]:

$$C_{\text{PN}}\frac{\text{d}v_{\text{c}}}{\text{d}t} = \frac{v_{\text{s}} - v_{\text{c}}}{R_{\text{PN}}} \tag{5.1a}$$

$$\Delta\phi(t) = \frac{\eta c}{n_{\text{g}}}\int_{t_0}^{t_0+\tau_0} v_{\text{c}}(t)\,dt \tag{5.1b}$$

where C_{PN} and R_{PN} are the capacitance and resistance for the p-n junction, $v_{\text{s}} = \frac{v_{\text{pp}}\sin(\omega t)}{2}$ is the applied RF signal, v_{pp} is the peak-to-peak value of the applied RF signal, ω is the RF frequency, t is the time variable, v_{c} is the voltage across the p-n junction, $\Delta\phi(t)$ is the accumulated phase change as a function of time, η is the slope of the waveguide phase change with respect to reverse bias voltage, c is the speed of light in the vacuum, n_{g} is the optical group index, and τ_0 is the optical transit time.

Based on Eqns. 5.1a and 5.1b, we will demonstrate the derivative of the voltage that falls on the capacitor and the resulting overall phase change. First, we will derive the solution for a linear differentiation equation as below:

$$y' + p(x)y = q(x) \tag{5.2}$$

where y' is the first order derivative of y with respect to x, $p(x)$ and $q(x)$ are both functions of x. Then, we introduce a function $I(x)$:

$$I(x) = \exp\left(\int p(x)dx\right) \tag{5.3}$$

When multiplying Eqn. 5.3 to both sides of Eqn. 5.2, we will obtain the following equation:

$$I(x)y' + I(x)p(x)y = I(x)q(x) \tag{5.4}$$

When differentiating $yI(x)$ with respect to x, we will have the following relationship:

$$\begin{aligned}
\frac{\mathrm{d}yI(x)}{\mathrm{d}x} &= y'I(x) + y\frac{\mathrm{d}I(x)}{\mathrm{d}x} \\
&= y'I(x) + y\frac{\mathrm{d}\exp\left(\int p(x)dx\right)}{\mathrm{d}x} \\
&= y'I(x) + y\exp\left(\int p(x)dx\right)\frac{\mathrm{d}\int p(x)dx}{\mathrm{d}x} \\
&= y'I(x) + yI(x)p(x) \\
&= I(x)q(x)
\end{aligned} \tag{5.5}$$

Therefore, the expression of $yI(x)$ can be derived from Eqn. 5.5:

$$yI(x) = \int (I(x)q(x)) + \text{constant} \tag{5.6}$$

and the constant is dependent on the initial conditions. The solution of $y(x)$ can be derived from Eqn. 5.6:

$$y(x) = \frac{\int (I(x)q(x)) + \text{constant}}{I(x)} \tag{5.7}$$

With the solution of the linear differentiation equation presented above, we can derive the solution to Eqn. 5.1a. In the case of Eqn. 5.1a, we will have the following expressions:

$$p(t) = \frac{1}{R_{\text{PN}}C_{\text{PN}}} \tag{5.8a}$$

$$q(t) = \frac{v_{\text{s}}}{R_{\text{PN}}C_{\text{PN}}} \tag{5.8b}$$

$$I(t) = \exp\left(\int p(t)dt\right) = \exp\left(\frac{t}{R_{\text{PN}}C_{\text{PN}}}\right) \tag{5.8c}$$

Therefore, the expression of v_{c} is derived with Eqn. 5.7, and Eqns. 5.8a-5.8c:

$$v_{\text{c}}(t) = \frac{\int (\exp\left(\frac{t}{R_{\text{PN}}C_{\text{PN}}}\right)\frac{v_{\text{s}}}{R_{\text{PN}}C_{\text{PN}}}dt) + \text{constant}}{\exp\left(\frac{t}{R_{\text{PN}}C_{\text{PN}}}\right)} \tag{5.9}$$

By taking the expression of $v_{\text{s}} = \frac{v_{\text{pp}}\sin(\omega t)}{2}$ into Eqn. 5.9, v_{c} can be expressed as follows:

$$v_{\text{c}}(t) = \frac{v_{\text{pp}}R_{\text{PN}}C_{\text{PN}}}{2}\frac{\int (\exp\left(\frac{t}{R_{\text{PN}}C_{\text{PN}}}\right)\sin(\omega t))dt + \text{constant}}{\exp\left(\frac{t}{R_{\text{PN}}C_{\text{PN}}}\right)} \tag{5.10}$$

To simplify the expression, we introduce another parameter a:

$$a = \frac{1}{R_{\text{PN}}C_{\text{PN}}} \tag{5.11}$$

Next, we will derive a simplified expression for $\int(\exp(at)\sin(\omega t))dt$:

$$\begin{aligned}\int(\exp(at)\sin(\omega t))dt &= \frac{1}{\omega}\int \exp(at)d(-\cos(\omega t)\\ &= \frac{1}{\omega}[\exp(at)(-\cos(\omega t)) + a\int(\cos(\omega t)\exp(at))dt]\\ &= -\frac{\exp(at)\cos(\omega t)}{\omega} + \frac{a}{\omega^2}\int(\exp(at))d(\sin(\omega t))\\ &= -\frac{\exp(at)\cos(\omega t)}{\omega} + \frac{a}{\omega^2}[\exp(at)\sin(\omega t) - a\int(\sin(\omega t)\exp(at))dt]\end{aligned} \tag{5.12}$$

Therefore, from Eqn. 5.12, the expression of $\int(\exp(at)\sin(\omega t))dt$ can be calculated as follows:

$$\int(\exp(at)\sin(\omega t))dt = \frac{1}{a^2\omega^2}\exp(at)(a\sin(\omega t) - \omega\cos(\omega t)) \tag{5.13}$$

Then, we take the simplified integration term Eqn. 5.13 into Eqn. 5.10 and assume the initial voltage is zero, the voltage that falls on the capacitor can be simplified as follows:

$$v_{\mathrm{c}} = \frac{a v_{\mathrm{pp}}}{2(a^2+\omega^2)}(a\sin(\omega t) - \omega\cos(at)), a = \frac{1}{R_{\mathrm{PN}}C_{\mathrm{PN}}} \tag{5.14}$$

By taking Eqn. 5.14 into Eqn. 5.1b, the accumulated phase change is calculated as follows:

$$\Delta\phi(t) = \frac{\eta c}{n_{\mathrm{g}}}\frac{a v_{\mathrm{pp}}}{2(a^2+\omega^2)}[-a\cos(\omega(t_0+\tau_0)) - \omega\sin(a(t_0+\tau_0)) + a\cos(\omega t_0) + \omega\sin(at_0)] \tag{5.15}$$

In the context of the EO BW, the magnitude of the small-signal response should be normalized to the maxima and can be approximated using the phase response [25]:

$$m(\omega) \approx |\frac{\phi(\omega)}{\phi(0)}| \tag{5.16}$$

The calculated results are shown in Fig. 5.7. The impact of the p-n junction on the overall EO-BW is small, even though being included in the calculation. Also, the estimated EO BW is around 12 GHz, smaller than the results considering the electrode and the p-n junction. Therefore, the device EO BW is limited by the optical transient time.

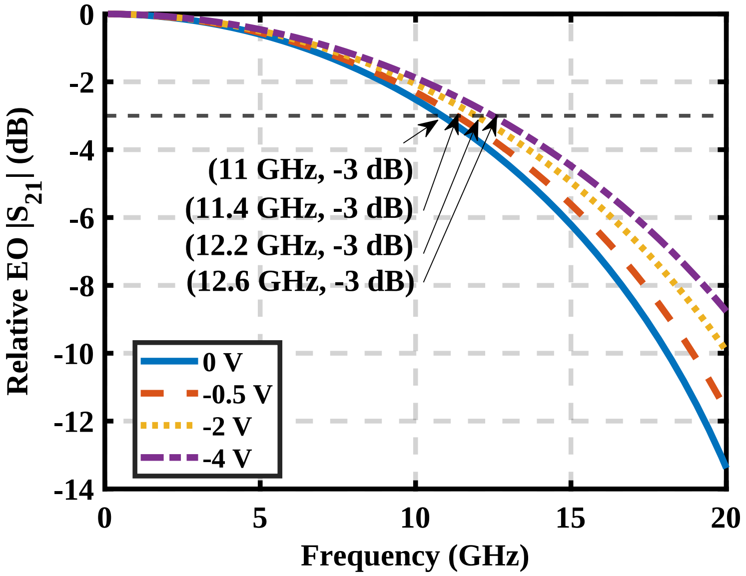

Fig. 5.7 Optical transit time limited EO BW estimation. [1] (© The Optical Society.)

5.2.4 Comparison with TWMZM

To compare the performance of the proposed MMZM to an SPP-based TWMZM, we simulate the TWMZM with a 1.6 mm length of CPS electrode. The top CPS electrode, shown in Fig. 5.8, is comprised of two conductors of 50 μm width and a 35 μm spacing. As demonstrated in Fig. 5.9, the metal and VIA layers are first simulated in HFSS. The simulation results compute the characteristic impedance $Z_{0\text{ul}}$ and propagation constant γ_{ul} for the unloaded CPS structures. The RLGC parameters for the unloaded CPS structures can be calculated by applying the following equations to $Z_{0\text{ul}}$ and γ_{ul} [25]:

$$R_{\text{tl}} = \text{Re}\{Z_{0\text{ul}}\gamma_{\text{ul}}\} \tag{5.17a}$$

$$L_{\text{tl}} = \frac{\text{Im}\{Z_{0\text{ul}}\gamma_{\text{ul}}\}}{\omega} \tag{5.17b}$$

$$G_{\text{tl}} = \text{Re}\{\frac{Z_{0\text{ul}}}{\gamma_{\text{ul}}}\} \tag{5.17c}$$

$$C_{\mathrm{tl}} = \frac{\mathrm{Im}\{\frac{Z_{0\mathrm{ul}}}{\gamma_{\mathrm{ul}}}\}}{\omega} \tag{5.17d}$$

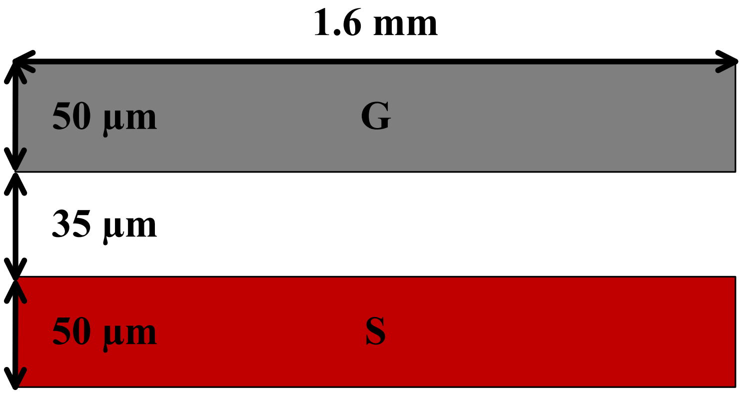

Fig. 5.8 Schematic of the simulated top electrode layer (not to scale). [1] (© The Optical Society.)

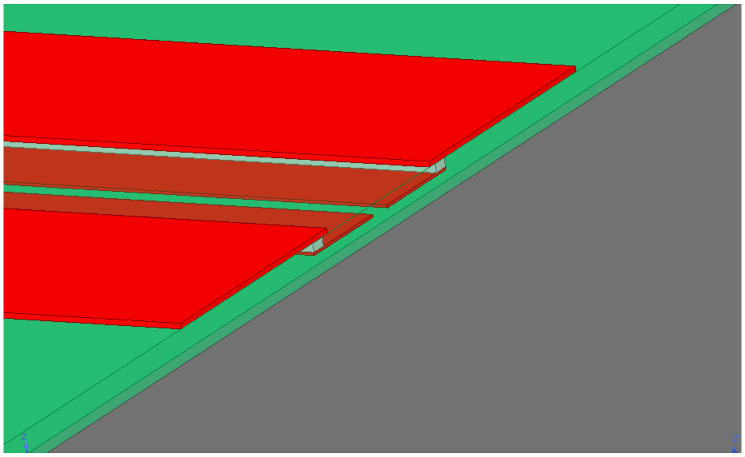

Fig. 5.9 Layout of the simulated electrode.. [1] (© The Optical Society.)

The calculated RLGC parameters of the unloaded CPS structure are shown in Fig. 5.10. The resistance and conductance model the power dissipated in the conductors and dielectric media, respectively. The inductance and capacitance model the energy stored in the magnetic and electric field, respectively. With increasing frequency, the numerical values of the resistance and conductance start to grow, indicating a rising power dissipation in the conductor and the dielectric media.

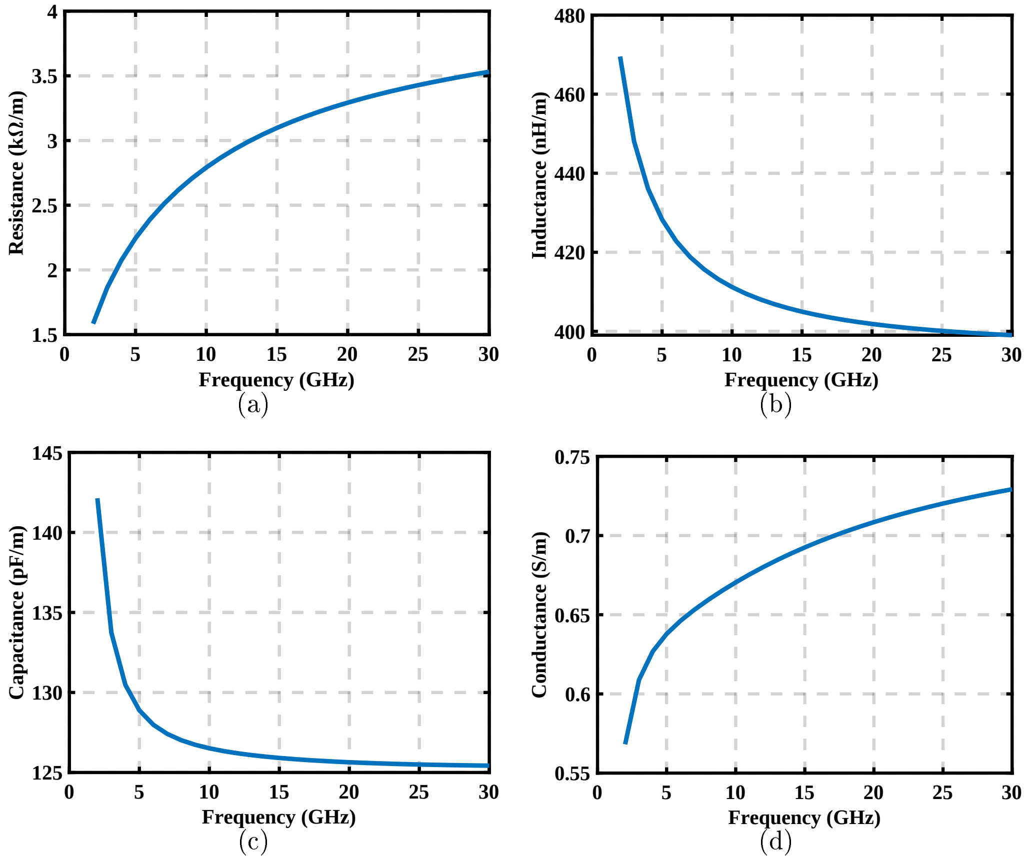

Fig. 5.10 RLGC parameters extracted from the electrode simulation results.

To estimate the characteristic impedance of the CPS electrode loaded with the p-n junction, the following parameters are introduced [25]:

$$Q = \frac{1}{\omega C_{\mathrm{pn}} R_{\mathrm{pn}}} \tag{5.18a}$$

$$R_{\mathrm{tpn}} = R_{\mathrm{pn}}(1 + Q^2) \tag{5.18b}$$

$$C_{\mathrm{tpn}} = C_{\mathrm{pn}} \frac{Q^2}{1 + Q^2} \tag{5.18c}$$

Based on Eqs. 5.18a-5.18c, the characteristic impedance Z_{l} of the loaded electrode, MW loss α_l, and the transfer function TF_VM considering velocity mismatch are calculated for different frequencies by the following equations [25]:

$$Z_\mathrm{l} = \sqrt{\frac{L_\mathrm{tl}}{C_\mathrm{tl} + C_\mathrm{tpn}}} \tag{5.19a}$$

$$\alpha_\mathrm{l} = \frac{R_\mathrm{tl}}{Z_\mathrm{l}} + (G_\mathrm{tl} + R_\mathrm{tpn}^{-1})Z_\mathrm{l} \tag{5.19b}$$

$$TF_\mathrm{VM} = 10\log_{10}(|\mathrm{sinc}(\frac{\pi f(n_\mathrm{g,\ pn} - n_\mathrm{g,\ O})}{c})|) \tag{5.19c}$$

where f is the MW frequency in units of Hz, c is the speed of light in vacuum, $n_\mathrm{g,\ pn}$ and $n_\mathrm{g,\ O}$ are the group indices of the MW signal in the p-n junction loaded electrode and the optical signal, respectively. Using the same SPP-based p-n junction, we calculate the characteristic impedance, MW loss, and velocity mismatch limited transfer function and demonstrate the results in Fig. 5.11.

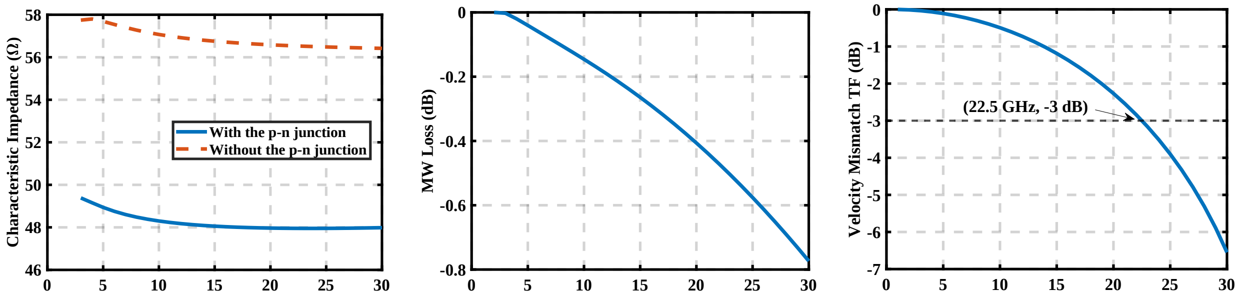

(a) (b) (c)

Fig. 5.11 EO BW estimation considering (a) characteristic impedance, (b) MW loss, and (c) velocity mismatch.

The characteristic impedance of the loaded electrode is around 48 Ω, with the unloaded electrode being intentionally designed to be slightly larger than 50 Ω. For a TWMZM of 1.6 mm, the 6.4-dB BW is much larger than 30 GHz, indicating the overall BW is not limited by the MW loss. The transfer function's 3-dB BW, considering only the velocity mismatch, is 22.5 GHz. For such a CPS structure, the group index difference between the MW signal and the optical signal is the factor limiting the EO BW. Therefore, the slow-wave electrode structure can be adopted to minimize the group index difference and increase the BW further.

Ideally, the modulation efficiency of the proposed MMZM and the TWMZM should be the same with an active region of the same length. The TWMZM is advantageous in terms of the EO BW and transmission capacity. In theory, by compromising 8 GHz EO BW, the footprint is reduced by 75% when adopting the MMZM design. Also, the energy consumption is positively proportional to the device's footprint [162]. Therefore, when integration density and power consumption are of priority, the proposed MMZM can be a promising candidate.

5.3 DC and small signal characterization

The modulator is fabricated using 193 nm lithography via a multi-project-wafer (MPW) run by the Advanced Micro Foundry (AMF). The fabricated device is on an SOI wafer with a 220-nm-thick top silicon layer, a 2-µm-thick buried oxide layer, and a silicon substrate having a 750 Ω-cm resistivity. The optical spectrum of the device is characterized by an FAU interfacing with on-chip vertical GCs. The measured IL spectra for the B2B GCs and the device under test are shown in Fig. 5.12. The IL at the maximum transmission of the device is 16.1 dB. The IL of a pair of GCs measured at the same wavelength on the same die is 12.9 dB. Assuming standard 2.5 dB/cm waveguide loss [206], the routing loss is estimated to be 1.1 dB. The calculated loss introduced by the modulator is 2.1 dB. The minimum optical interference ER is 32 dB.

The V_π of the modulator is measured by sweeping the DC voltages applied to the "G" and "S" electrodes at different reverse-biased voltages [207]. First, the laser wavelength is adjusted to the 3-dB operational point for each reverse-biased voltage when no driving voltage is applied. Then, the differential DC voltages are simultaneously applied to the "G" and "S" electrodes with equal amplitude and reverse sign. The output optical power is recorded when sweeping the driving voltage at each reverse-biased voltage. The optical power is normalized to its maximum for each biasing voltage and is shown in Fig. 5.13. The V_π is then calculated as the driving voltage difference when the maximum and minimum normalized optical powers are achieved: $V_\pi = |(V_\mathrm{G} - V_\mathrm{S})_\mathrm{max} - (V_\mathrm{G} - V_\mathrm{S})_\mathrm{min}|$. The measured V_π is shown in Table 5.2 for different biasing voltages. V_π rises with increasing reverse biased voltages. The growth of V_π is because, as the width of the depletion region continues

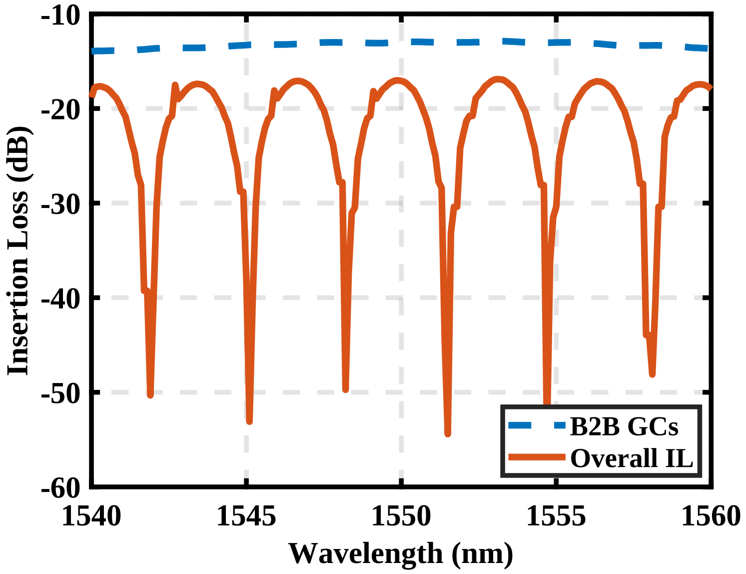

Fig. 5.12 Optical spectrum for B2B GCs and the device under test. [1] (© Optica Publishing Group.)

to expand, the overlap between this region and the optical mode decreases. However, the increase in V_π with growing bias voltage is faster than a traditional TWMZM. This indicates that the decreasing rate of the overlap reduction for a MMZM is faster than for a TWMZM, attributed to fabrication imperfection

The EO and EE responses of the modulator are measured with an Agilent 50 GHz lightwave component analyzer (LCA) and a 40 GHz GSSG probe. The RF cable and probe calibration is performed before the measurement. The measured EO S_{21} response at different reverse bias voltages, normalized to 1 GHz, is shown in Fig. 5.14. The corresponding 3-dB EO BWs are summarized in Table. 5.2. The increase in EO BW with higher reverse-biased voltage is not apparent, which can be attributed to lower p-n junction efficiencies. Also, the measured EO BW is smaller than the estimated result in Sec. 5.2.3. To further examine the limiting factor of this modulator, the EE S_{11} response is measured and used to extract the values for the lumped circuit model.

The measured EE S_{11} response at various reverse-biased voltages is shown in Fig. 5.15. High reflection is observed at low frequencies, which is not an indication of poor modulation [205]. When reverse biased, the p-n junction behaves as a capacitor, resembling an open circuit at low frequencies. The measured results are then imported to Keysight

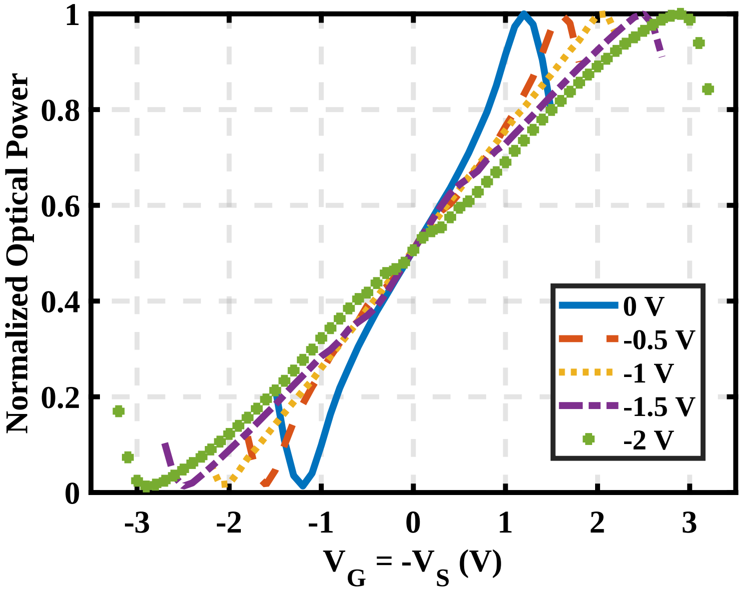

Fig. 5.13 Normalized measured optical power at different reverse bias voltages. [1] (© Optica Publishing Group.)

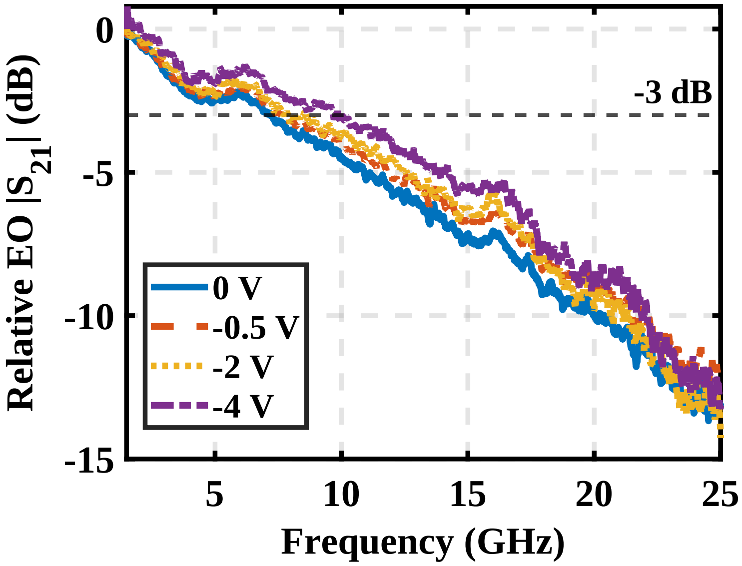

Fig. 5.14 Measured EO S_{21} response at different reverse bias voltages. [1] (© Optica Publishing Group.)

Table 5.2 Summary of the V_{π} and 3-dB EO BW at different reverse bias voltages. [1] (© Optica Publishing Group.)

Reverse Bias	0 V	−0.5 V	−2 V	−4 V
V_{π}	4.8 V	6.4 V	11.6 V	NA
3-dB EO BW	7.3 GHz	7.7 GHz	8.0 GHz	9.7 GHz

ADS to extract the numerical values of the circuit elements shown in Fig. 5.16. For the lumped circuit model, R_{s} models power dissipated in the conductors, C_{pad} is the parasitic capacitance between the electrodes, L_{lead} is the parasitic lead inductance, r_{b} is the resistance including the contact and the quasi-neutral region, g_{d} is the conductance of the p-n junction, and c_{j} is the capacitance of the p-n junction.

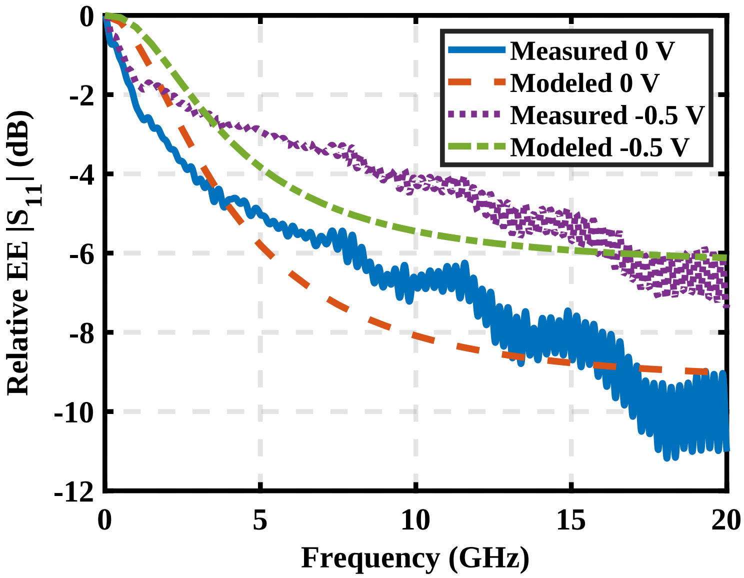

Fig. 5.15 Measured and modeled EE S_{11} response. [1] (© Optica Publishing Group.)

The extracted values for the circuit elements and the calculated junction BWs at various bias voltages are shown in Table 5.3. The calculated S_{11} responses from the lumped circuit model are also shown in Fig. 5.15. When increasing the bias voltage, the MW loss modelled by R_{s} is small and remains almost the same. The slight MW loss primarily comes from the dielectric loss from the embedded p-n junction instead of the conductor loss from the electrode. When reverse-biased, the resistance and capacitance of the p-n junction decrease while C_{pad} remains almost the same. However, the calculated resistance and capacitance of the p-n junction are much higher than the simulated results, indicating a less efficient p-n junction because of the fabrication errors. The discrepancy between the simulation and calculated results for the p-n junctions can be explained as follows: a) the asymmetry of the p-n junctions increases the overall capacitance of the SPP structures, which is also reported in [25]; and b) the boundary between the highly doped and the lightly doped regions may be blurred, and the extended highly doped region increases the overall resistance and capacitance. The junction BWs $\frac{1}{2\pi r_{\text{b}} c_{\text{j}}}$ are also calculated with the simulated p-n junction parameters and demonstrated in Table 5.3. From the calculated junction BWs and the calculated EO S_{21} responses, we determine that the EO BW is limited by both the optical transient time and the configuration of the p-n junction. Lastly, the parasitic inductance L_{lead} is also higher than the result shown in [205], and results from the accumulated magnetic field introduced by the extended metal teeth.

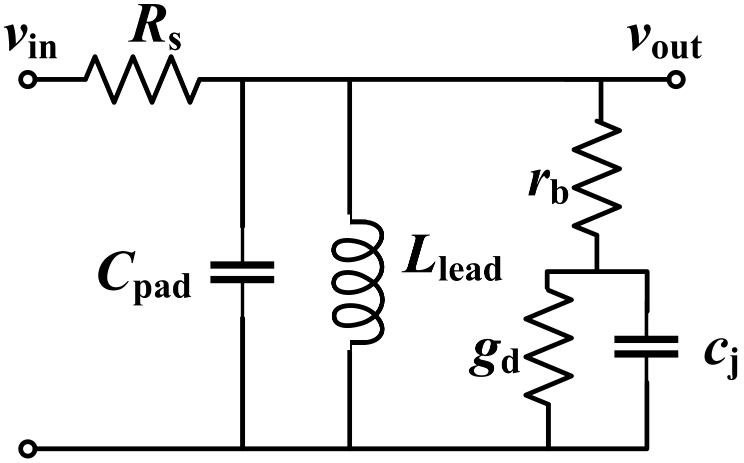

Fig. 5.16 Lumped circuit model to fit the EE S_{11} response. [1] (© Optica Publishing Group.)

5.4 Large signal characterization: OOK and PAM modulation with DSP

Transmission experiments utilizing the modulator are carried out with a DAC, an analog-to-digital converter (ADC), and basic DSP, which is very similar to [165,205,208]. A schematic

Table 5.3 Small signal circuit model in Fig. 5.16 for reverse-biased junctions.

Bias (V)	R_s (Ω)	C_pad (fF)	L_lead (pH)	r_b (Ω)	c_j (pF)	$1/g_\mathrm{d}$ (kΩ)	Junction BW (GHz)
0	4.93	38.62	150.5	9.33	1.8	27.4	9.47
−0.5	4.45	37.66	160	7.86	1.5	27.6	13.50

of the experimental setup is shown in Fig. 5.17. The transmitted data is generated by offline DSP and uploaded to a DAC which runs at 120 GSamples/s (GSa/s). An RF amplifier with a 3-dB BW of 44 GHz and 26 dB gain is used to amplify the generated analog signal. The amplitude of the transmitted signal is adjusted at the DAC end for the measurement simplicity. A 40 GHz, GSSG RF probe is used to apply the RF signal to the modulator. A C-band tunable laser is connected to the FAU, interfaced by on-chip vertical GCs, to inject and collect optical signals to and from the device. The device is biased at the quadrature point by tuning the optical wavelength. The DC bias is also applied to the modulator through the GSSG probe. The modulated optical signal is then launched into 2 km of Corning SMF-28e+ fiber or directly connected to the receiver side for the B2B experiment. A 35 GHz Picometric photoreceiver composed of a photo-diode and a trans-impedance amplifier is used at the receiver side to convert the optical signal to the RF domain. The amplified signal is digitized by a real-time oscilloscope (RTO) with a 33 GHz BW, 8-bit resolution, and a sampling rate of 80 GSa/s.

The steps of offline DSP on the transmitter and receiver ends are shown in Fig. 5.18. The symbols are randomly generated for different PAM formats in the transmitter side. The symbols are then up-sampled to 2 samples per symbol (sps) for raised cosine (RC) pulse-shaping. The roll-off factor ($\alpha \in [0, 1]$) at each symbol rate is chosen empirically to get the best BER. The samples are then resampled to match the DAC sampling rate for pre-emphasis function, which compensates for the low pass response of the DAC. Finally, the samples are clipped and quantized to 8-bit resolution and uploaded to DAC memory for transmission. On the receiver end, the data captured by the RTO is first re-sampled to 2 sps [209]. The re-sampled data is then equalized with a finite-impulse-response (FIR) filter using 21 taps, where the coefficients are calculated from a training sequence. After the equalizer, the BER is calculated by comparing the transmitted and received binary streams by mapping both data into binary sequences.

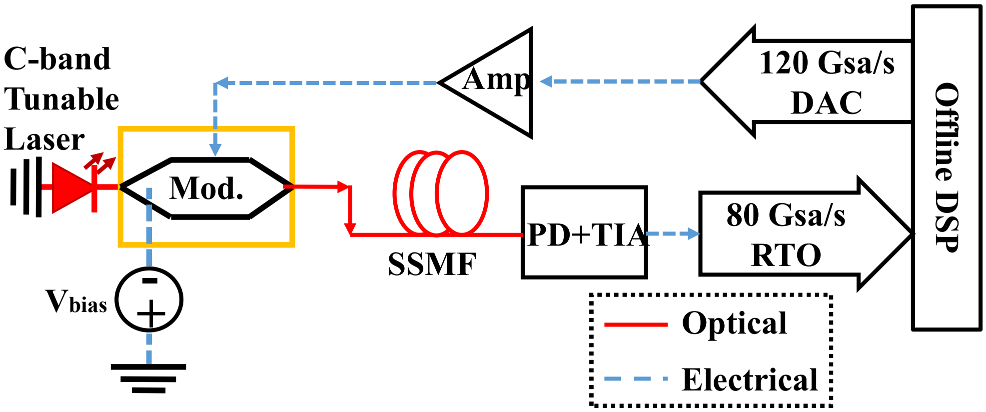

Fig. 5.17 Schematic of the transmission experiment setup. [1] (© Optica Publishing Group.)

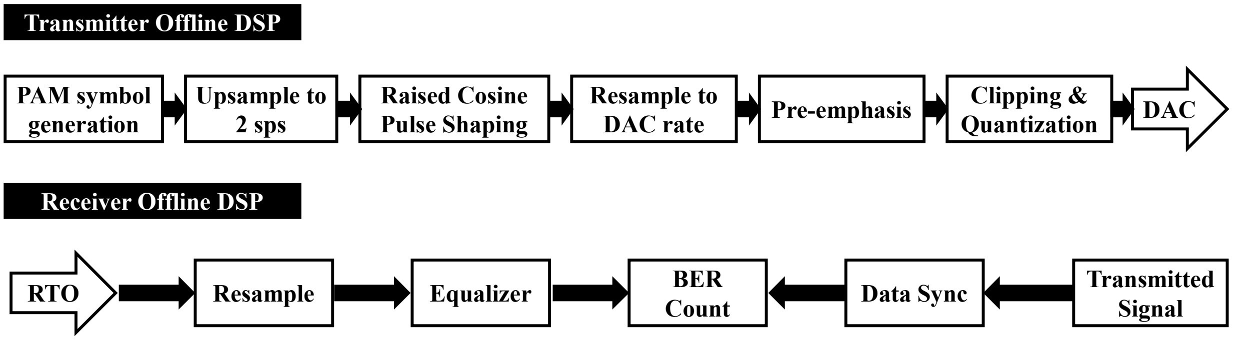

Fig. 5.18 Transmitter and receiver offline digital signal processing. [1] (© Optica Publishing Group.)

The applied RF driving voltage for the transmission experiment is 4.5 V_{pp} for PAM-2 and PAM-4 and 4 V_{pp} for PAM-8. Due to the high linearity requirement of the PAM-8 format, a smaller signal amplitude is used. The eye diagrams of the B2B transmission for different PAM orders with calculated BERs are shown in Figs. 5.19(a)-5.19(c). For different PAM orders, the BERs as functions of bitrates at B2B transmission at different bias voltages are displayed in Figs. 5.20(a)-5.20(c). The pre-FEC KP4 and soft-decision (SD) BER thresholds are 2.4×10^{-4} and 2×10^{-2}, respectively [21, 210]. When the reverse bias voltage is increased from 0 V to -0.5 V for all the PAM orders, the performance improves below specific symbol rates. At lower symbol rates, the performance is limited by the EO BW of the device. Therefore, with a higher reverse bias voltage, the EO BW increases and the performance is improved. However, the modulator's driving swing limits the performance at higher symbol rates. Therefore, the performance improvement is negligible beyond the specific symbol rate at -0.5 V bias. In addition, V_π also increases with higher reverse bias voltage. A higher driving voltage is required with higher V_π. Consequently, when the bias is increased to -1 V, the performance of all the modulation formats degrades with the same RF driving voltage. Hence, the reverse bias is set as -0.5 V for all the signal formats. The maximum measured bitrates with BER below the HD-FEC BER threshold for PAM-2, 4, and 8 are 70, 106, and 75 Gb/s, respectively. Therefore, PAM-4 is the optimal modulation format with such a modulator.

For PAM-4 signaling at B2B transmission, the maximum measured symbol rates below the KP4 and HD BER thresholds are 42 and 53 Gbaud, respectively. We transmitted PAM-4 signals at those two symbol rates over different distances, and the corresponding BER is calculated at different received optical powers (ROPs). Because of the insertion loss introduced by the GCs, the maximum received optical power is limited to -3 dBm. The minimum ROPs required for 42 and 53 Gbauds PAM-4 signal below the HD-FEC BER threshold of 3.8×10^{-3} is found to be -6 dBm and -3 dBm, respectively.

5.5 Energy consumption

The energy consumption of a modulator can be divided into three categories: power consumed by the junctions, the terminators, and the biasing circuitry. For lumped modulators and TWMZMs, most energy is consumed at the p-n junctions and terminators, respectively. Also, since the biasing of the proposed modulator is enabled by tuning the laser

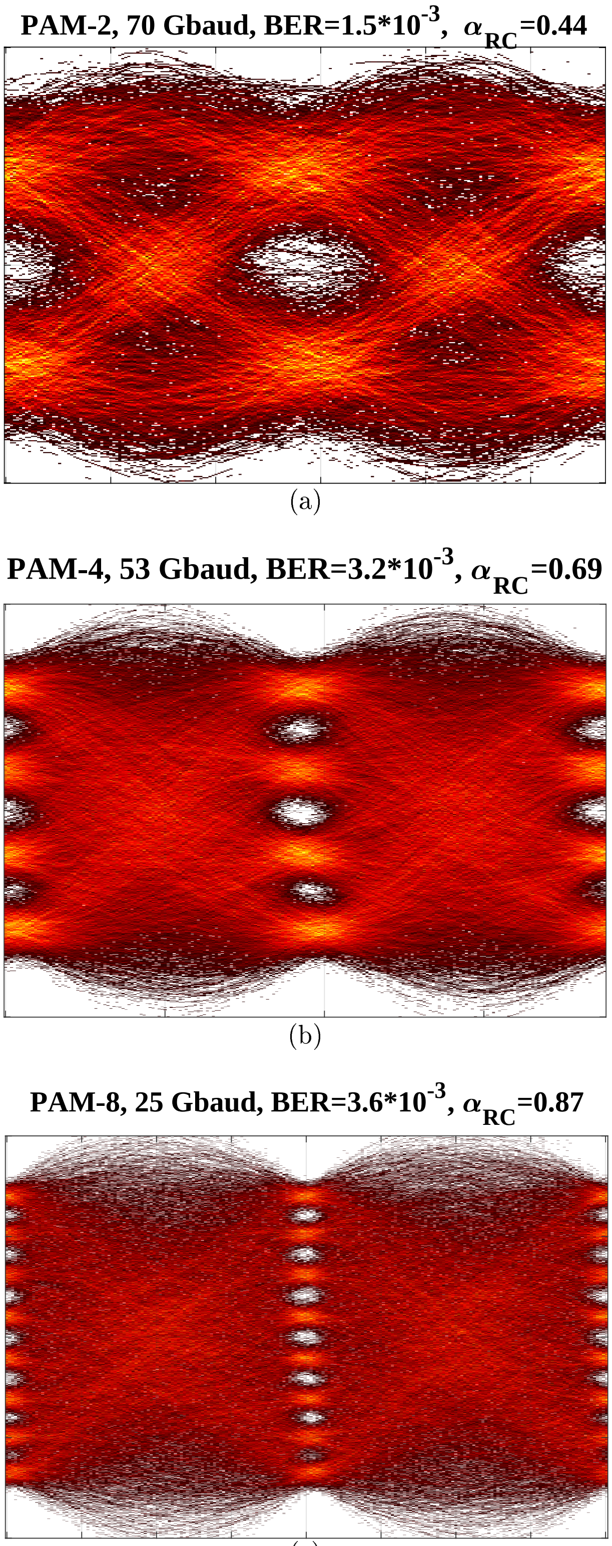

PAM-2, 70 Gbaud, BER=$1.5*10^{-3}$, α_{RC}=0.44

(a)

PAM-4, 53 Gbaud, BER=$3.2*10^{-3}$, α_{RC}=0.69

(b)

PAM-8, 25 Gbaud, BER=$3.6*10^{-3}$, α_{RC}=0.87

(c)

Fig. 5.19 Processed eye diagrams after receiver equalization at B2B for (a) PAM-2; (b) PAM-4; (c) PAM-8. [1] (© Optica Publishing Group.)

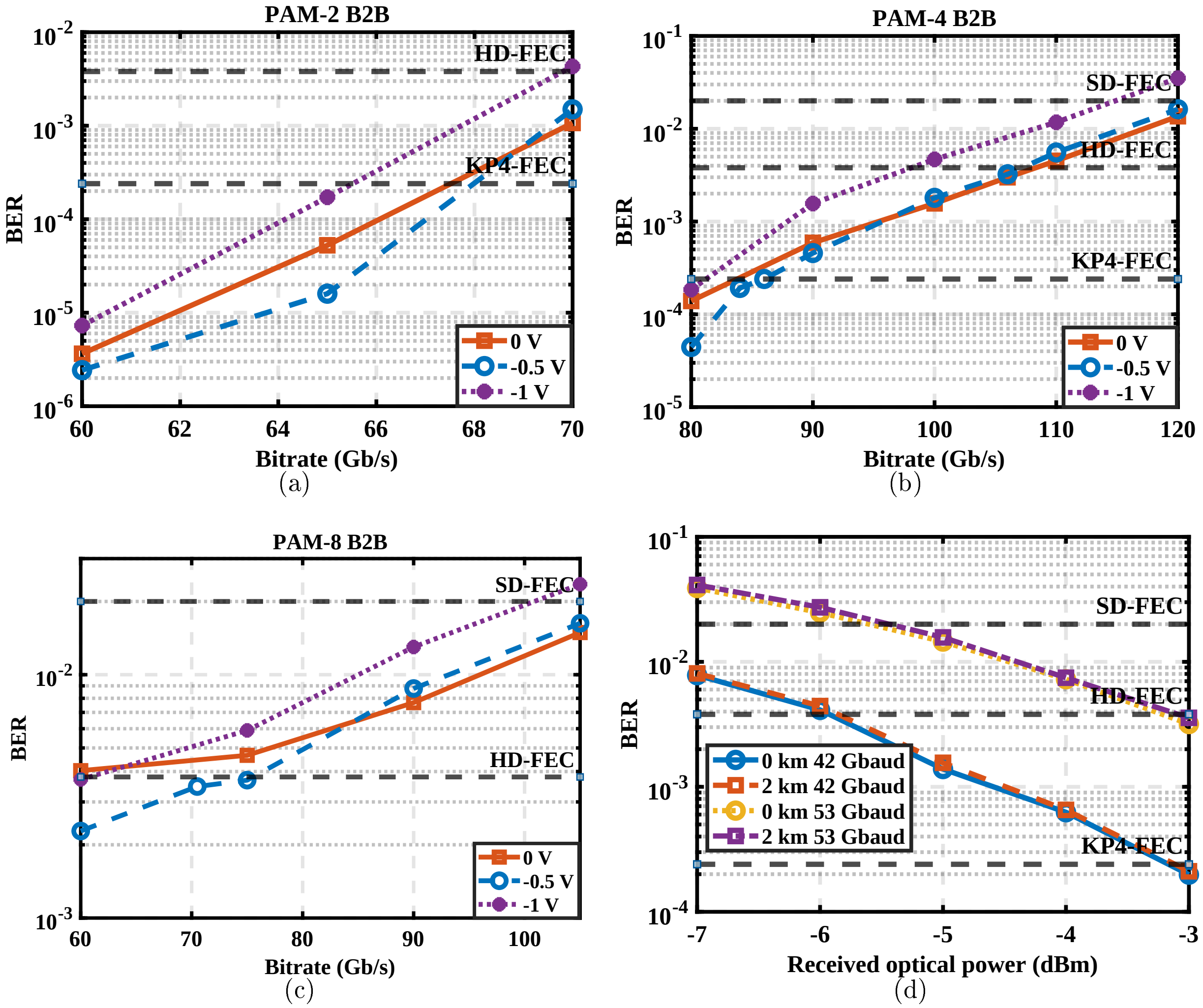

(a) (b) (c) (d)

Fig. 5.20 Bit error rate for different bias voltages at B2B transmission for (a) PAM-2; (b) PAM-4; (c) PAM-8. (d) Receiver sensitivity for PAM-4 signal at B2B and after 2 km of standard single-mode fiber propagation at two different symbol rates. [1] (© Optica Publishing Group.)

wavelength, the power consumed by the biasing circuitry is negligible. The following equation is applied to calculate the energy consumption per bit E_b for lumped modulators with PAM-M formats [195]:

$$E_{\mathrm{b,\ Lumped}} = \frac{CV_{\mathrm{pp}}^2}{M^2 \log_2 M} \sum_{i=0}^{M-1} (M-i)(\frac{i}{M-1})^2 \tag{5.20}$$

where C is the capacitance of the p-n junction. For a TWMZM with a 50 Ω terminator, the dynamic power consumption per bit is calculated with the following expression [195]:

$$E_{\mathrm{b,\ TWMZM}} = \frac{V_{\mathrm{rms}}^2}{50 \times \mathrm{Bitrate}} \tag{5.21}$$

where V_{rms} is the root mean square voltage.

To compare the energy consumption per bit for the maximum bit rates utilizing different PAM orders with BERs below the pre-HD-FEC BER threshold, we summarize the calculated values for various driving voltages in Table 5.4.

Table 5.4 Estimated energy consumption per bit for the junctions and terminator.

	PAM-2	PAM-4	PAM-8
Symbol rates (Gbaud)	35	53	25
Bit rates(Gb/s)	70	106	75
V_{pp} (V)	4.5	4.5	4
Junction (Fab) (pJ/bit)	7.59	2.10	0.86
Junction (Simulation) (pJ/bit)	1.01	0.28	0.11
Terminator (pJ/bit)	1.45	0.96	1.07

5.6 Conclusion

The design, simulation, and experimental characterization of a SPP-MMZM are presented in this Chapter. With a 432×260 $\mu\mathrm{m}^2$ footprint, this compact modulator demonstrates a small IL of 2.1 dB. The half-wave voltage (V_π) and 3-dB EO BW are found to be 6.4 V and 7.7 GHz at -0.5 V bias, respectively. We conclude that the modulation efficiency and EO BW could be improved with better fabrication accuracy. We have achieved 53 Gbaud

PAM-4 transmission (106 Gb/s) over 2 km of SSMF fiber with a calculated BER below the pre-FEC HD BER threshold of 3.8×10^{-3}. Such a compact modulator with low IL and high thermal stability is promising for low-cost transceiver design utilizing DWDM application.

Chapter 6

Conclusion

6.1 Overview

Numerous online communication and commercial activities, including video streaming, cloud-based storage and services, and machine-to-machine applications, have driven the rapid development of D-Cs and DCIs. To cope with the exponential increase in internet traffic, high-speed and low-cost transceivers with mass manufacturing capability are of great interest. Among many other materials, the SiP technology has rapidly matured as a large-scale PIC solution. The SiP technology can utilize the manufacturing process and tools used in the traditional and well-developed CMOS industry. The CMOS compatibility offers a short-cut to high-volume manufacture at low cost and the potential for EO co-package. Also, the high index contrast of the SiP platform enables tight bends and minor waveguide spacing, allowing PICs with high integration density. However, the high index contrast also makes the devices vulnerable to nanometer-scale variations in waveguide core width or thickness. Therefore, the fabrication process variability significantly impacts the device performance, reducing the durability and repeatability of the devices fabricated on this platform. Also, the refractive index of Si is sensitive to temperature change because of the material thermal property. To actively control the temperature on all the transceivers employed in the D-Cs will sharply increase the overall cost and complexity. Consequently, it is preferable to develop SiP devices that are compact in footprint, resistant to fabrication error and temperature change, and low in optical ILs.

Building on this motivation, we present the three key components used in the transmitters: power splitters, wavelength (de-)MUX, and modulator. We first explored the method to realize random SRs for the OACs. Then, a time-efficient simulation method is proposed to improve the performance of the OACs. The proposed OACs demonstrate superior resistance to temperature variation and fabrication error. Next, we report a CMOS-compactible and temperature-insensitive wavelength (de-)MUX design on the SOI platform. Despite the high thermal sensitivity of the Si material, the proposed wavelength (de-)MUX proves robust stability against temperature change. Finally, we exhibit a compact modulator on the SiP platform with low optical IL and robustness to thermal and fabrication variations.

6.2 Summary of original contributions

We present in Fig. 6.1 the summary of the original contributions demonstrated in this thesis. The details of our contributions to each Chapter are given below.

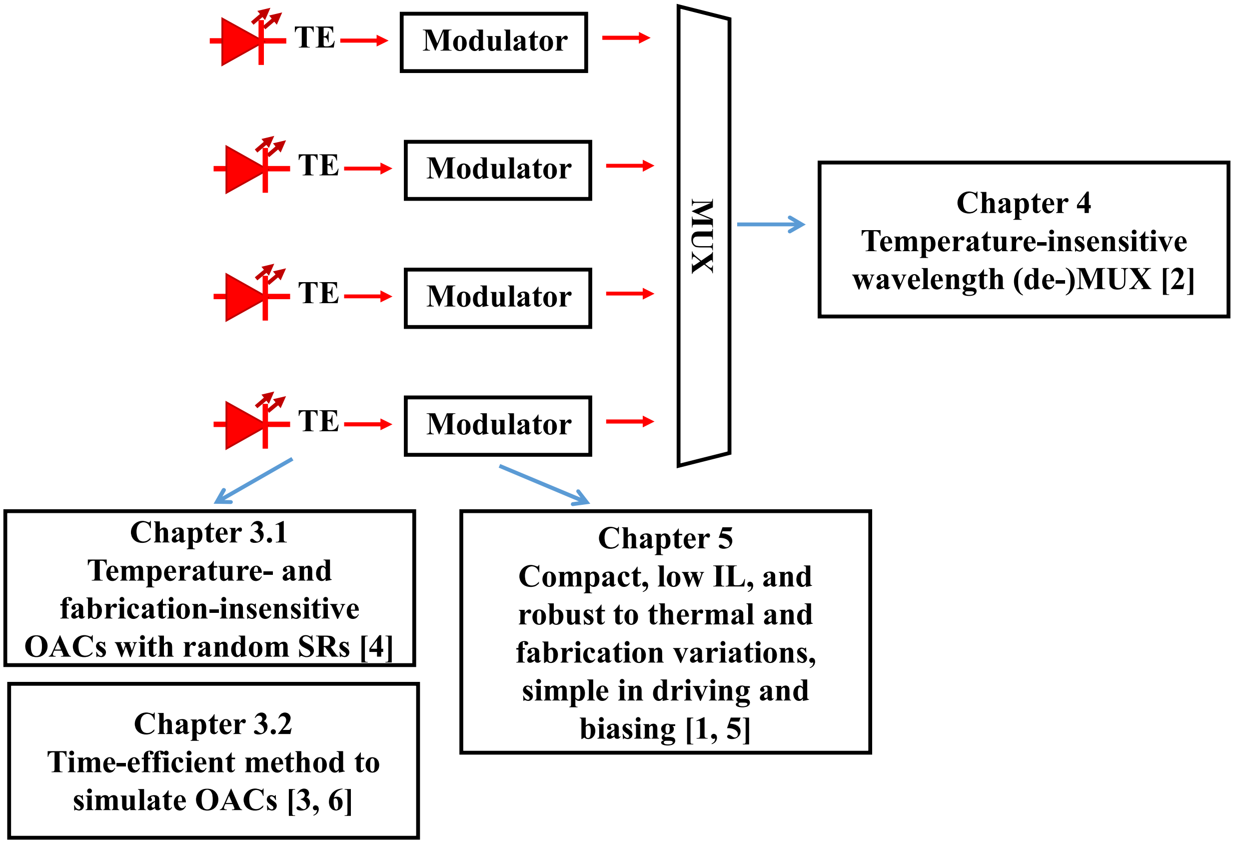

Fig. 6.1 Summary of the original contributions of this thesis.

Chapter 3

In Section 3.1, the broadband 2×2 OACs with random SRs are experimentally demonstrated on the SOI platform. The operational principle of the OAC is illustrated first. We theoretically analyze the sources of losses in each region and clarify how to reduce these losses. The expression of the IL in the mode-evolution region is also derived. We have theoretically demonstrated why such devices require long distances to reduce ILs. After analyzing the basic operating principle of the device, we derived the theoretical expression between the SR and the output waveguide of the device. We then verify our theory by comparing the analytical solution, numerical simulation software, and experimental results. The results obtained from both the analytical and soft solutions of the simulation agree with the experiment, indicating that our theoretical analysis is correct. Finally, we tested the device at different temperatures. The device demonstrates good thermal insensitivity in the temperature range that the experimental equipment can reach.

In Section 3.2, we propose a time-efficient method to improve the performance of the 2×2 OAC. This simulation reduces the simulation time from hours to minutes compared to the traditional software-based simulation. First, we obtain the expression for the adiabatic condition in the transmission direction, employing the mode-coupling theory's matrix expression. We then express the propagation constants and coupling coefficients in terms of waveguide width and spacing for the mode-evolution region of the device by first-order approximation. Substituting the approximate expressions for the waveguide constants into the previously obtained adiabatic conditions, we obtain the expressions for the adiabatic conditions with respect to the waveguide widths and spacings. By analyzing the relationship between the first-order derivative of the adiabatic constant and the waveguide width and spacing, we obtain a series of conditions for reducing the adiabatic constant. With these conditions, we choose the best waveguide evolution equation. We verified the feasibility of the theory through experiments. At the same time, we have improved the SR of the device in the 100 nm wavelength range and reduced the device's size.

Chapter 4

Chapter 4 demonstrates a 1×4 C-band MZI-based wavelength (de-)MUX with superior thermal stability on the SOI platform. We first design a 2×2 paired-interference-based MMI coupler with good thermal stability. Chapter 4 demonstrates a 1by4 C-band MZI-based wavelength (de-)MUX with superior thermal stability on the SOI platform. We first design a paired-interference-based MMI coupler with good thermal stability. Then we bring the S-parameters of the coupler obtained from the simulation into the transmission matrix and calculate the transmission spectrum of a conventional MZI-based MUX at different temperatures. From the calculated transmission spectrum, we can calculate the device's TOC. Next, we propose a scheme based on matching the length and width of the waveguide. By analyzing the FSR of the device, we obtain an expression for the waveguide dimensions that bring the TOC down to zero. For the parameters we selected, we also considered the manufacturing error. Our proposed design has a high tolerance for fabrication errors. We experimentally measured the transmission spectra of the device at different temperatures and calculated the TOCs. Compared to conventional MZI-based MUXs, our devices exhibit excellent temperature stability.

Chapter 5

Chapter 5 demonstrates a compact MZM with serpentine phase shifters and simplified driving and biasing circuitry. We first simulated the electrode characteristics of the modulator by the HFSS solver. Then by Keysight ADS, we fit the S-parameter calculated from the HFSS solver into an equivalent circuit. In the equivalent circuit, we include both the resistance and capacitance values of the p-n junction obtained from the CHARGE solver. Thus we acquired the EO BW simulation results considering electrodes and p-n junctions. Next, we consider the effect of optical transit time on the EO BW. We obtain the theoretical expression for the EO BW in the optical transit time limit by theoretical derivation. We then plot that theoretical expression using numerical simulation software. By comparison, we find that the EO BW is mainly limited by the optical transit time for this modulator. This EO co-simulation approach can be used to keep improving the performance of such devices. Next, we characterize the device's DC, small-signal, and large-signal performance. The insertion loss of the device is as low as 2.1 dB. With a -0.5 V reverse bias, the modulator demonstrates a V_π and 3-dB BW of 6.4 V and 7.7 GHz. A 53 Gbaud PAM-4 transmission over 2 km SSMF is achieved with a BER below the HD-FEC BER threshold.

6.3 Future work

The work of this thesis can be further extended. Section 6.3.1 presents some possible short-term improvements. In addition, we introduce some interesting long-term objectives in Section 6.3.2.

6.3.1 Short-term objectives

Power splitter

Over the past decades, there have been numerous power splitters designs with superior performance on the market. What is lacking is a stable and accurate model of device performance based on a particular process line. An accurate device performance model enables precise system-level design, which is the path the silicon-optics industry must take to align with electronic chip design.

Athermal wavelength (de-)MUX

Based on the proposed athermal wavelength (de-)MUX, there is still much room for improvement: the ILs, XTs, and flat-top response. The ILs of the couplers dominate the ILs of the wavelength (de-)MUX. The SRs of the couplers also determines the XTs of each channel. Therefore, we can keep improving the performance by optimizing the couplers employed in the MUX.

In the meantime, the side-wall roughness should be considered during the simulation to estimate the phase noise introduced along the delay path more accurately. The phase noise limits each channel's XT and breaks the athermal designs' phase-matching condition.

To realize a flat-top channel response for MZI-based MUXs, researchers often adopt multiple stages composed of various delay length differences and couplers with different SRs. The interference and FSR created by these stages should be carefully designed and matched for athermal operation.

Modulator

For the proposed MMZM, we could keep improving the modulation BW and efficiency. As pointed out in Chapter 5, the performance of the modulator is limited by the inaccurate p-n junction masking process. Therefore, we can update the design of the p-n junction by considering the fabrication limit. Also, we could use the same method to estimate the EO-BW for different designs in the future.

In a broader sense, to keep increasing the EO BW of integrated modulators without raising the cost unreasonably, bonded thin-film lithium niobate modulator on the SiP platform could be a promising solution.

6.3.2 Long-term objectives

It has been widely accepted that transceivers built on the SiP platform can be used on D-Cs and DCIs. These transceivers can be used in many other applications, including cryptography. With the development of online services, information security has become a critical issue for internet service providers. Cryptography is practicing and studying techniques for secure communication against adversarial behaviour. Classical cryptography utilizes multiple disciplines, including information theory, statistics, abstract algebra, and number theory, to create secure keys with significant computational complexities. However, with the introduction of supercomputers, which can serve as powerful ciphers, the security of classical cryptography is compromised. Thus, the idea of quantum cryptography has drawn significant attention recently. One of the most famous applications of quantum cryptography is quantum key distribution (QKD). There are two main categories of QKD systems: discrete variable QKD (DV-QKD) and constant variable (CV-QKD). Compared to the DV-QKD system, CV-QKD systems do not require single-photon sources and single-photon detectors, making them capable of being realized on existing telecom infrastructures.

Over the years, chip-level CV-QKD systems have been realized on different platforms, including indium phosphide and lithium niobate. CV-QKD system-based SiP platform is still worth exploring. There are three vital devices to realize an integrated CV-QKD system: modulators, hybrids, and balanced photodetectors (BPDs). Considering that the current integrated CV-QKD system is not limited by the BW of the modulator, a power-efficient and compact modulator with high efficiency is sufficient. The function of a hybrid is to separate the in-phase and quadrature signals of the received signal by adding a specific phase shift. The separated signal is then sent to BPDs to translate the optical phase and amplitude information into the electrical domain. Thus, the hybrid with precise phase response is crucial to the receiver. Also, since high-speed TIA is not available or very expensive on the market, developing a BPD without a TIA is cost-effective.

References

[1] D. Mao, M. S. Alam, M. Parvizi, E. El-Fiky, A. Abdo, N. Ben-Hamida, and D. V. Plant, “Design, analysis, and characterization of a compact silicon photonic modulator with meandered phase shifters,” *Optics Express*, vol. 30, no. 18, pp. 32 990–33 002, 2022.

[2] D. Mao, Y. Wang, L. Xu, J. Zhang, E. El-Fiky, M. S. Alam, Y. D’Mello, S. Lessard, and D. V. Plant, “CMOS-compatible and temperature insensitive C-band wavelength (de-)multiplexer,” *IEEE Photonics Technology Letters*, vol. 34, no. 14, pp. 769–772, 2022.

[3] D. Mao, Y. Wang, L. Xu, E. El-Fiky, M. Jacques, J. Zhang, M. S. Alam, A. Kumar, Y. D’Mello, and D. V. Plant, “Adiabatic coupler with nonlinearly tapered mode-evolution region,” *IEEE Photonics Technology Letters*, vol. 33, no. 16, pp. 840–843, 2021.

[4] D. Mao, Y. Wang, E. El-Fiky, L. Xu, A. Kumar, M. Jaques, A. Samani, O. Carpentier, S. Bernal, M. S. Alam, J. Zhang, M. Zhu, P.-C. Koh, and D. V. Plant, “Adiabatic coupler with design-intended splitting ratio,” *Journal of Lightwave Technology*, vol. 37, no. 24, pp. 6147–6155, 2019.

[5] D. Mao, M. S. Alam, M. Parvizi, E. El-Fiky, A. Abdo, N. Ben-Hamida, and D. V. Plant, “Compact silicon photonics meandered Mach-Zehnder modulator,” in *Conference on Lasers and Electro-Optics*, San Jose, CA, USA, 2022, pp. SF4M–3.

[6] D. Mao, Y. Wang, L. Xu, E. El-Fiky, M. Jacques, J. Zhang, Y. D’Mello, S. Lessard, and D. V. Plant, “Nonlinearly tapered 3-dB adiabatic coupler,” in *IEEE Photonics Conference*, 2020, pp. 1–2.

[7] D. Mao, M. Parvizi, M. S. Alam, A. Abdo, N. Ben-Hamida, E. El-Fiky, and D. V. Plant, “Electrode design for slow-light based Mach-Zehnder modulator in silicon photonics,” in *Advanced Photonics Congress*, 2021, pp. IW1B–4.

[8] J. Zhang, L. Xu, D. Mao, Z. Xing, Y. D’Mello, M. Jacques, Y. Wang, S. Lessard, and D. V. Plant, “High-extinction-ratio and compact 1310/1550 nm wavelength diplexer

on SOI platform based on an SWG-structured two-mode interference coupler," *IEEE Photonics Journal*, vol. 14, no. 2, pp. 1–6, 2022.

[9] J. Zhang, L. Xu, D. Mao, Y. D'Mello, W. Li, S. Lessard, and D. V. Plant, "All-silicon multi-band TM-pass polarizer on a 220 nm SOI enabled by multiplexing grating regimes," *Optics Express*, vol. 30, no. 1, pp. 326–335, 2022.

[10] M. G. Saber, L. Xu, R. H. Sagor, Y. Wang, A. Kumar, D. Mao, E. El-Fiky, D. Patel, A. Samani, Z. Xing, M. Jacques, Y. D'Mello, and D. V. Plant, "Integrated polarization handling devices," *IET Optoelectronics*, vol. 14, no. 3, pp. 109–119, 2020.

[11] L. Xu, Y. Wang, D. Mao, J. Zhang, Z. Xing, E. El-Fiky, M. G. Saber, A. Kumar, Y. D'Mello, M. Jacques, and D. V. Plant, "Ultra-broadband and compact two-mode multiplexer based on subwavelength-grating-slot-assisted adiabatic coupler for the silicon-on-insulator platform," *Journal of Lightwave Technology*, vol. 37, no. 23, pp. 5790–5800, 2019.

[12] L. Xu, Y. Wang, D. Mao, E. El-Fiky, Z. Xing, A. Kumar, M. G. Saber, M. Jacques, and D. V. Plant, "Broadband 1310/1550 nm wavelength demultiplexer based on a multimode interference coupler with tapered internal photonic crystal for the silicon-on-insulator platform," *Optics Letters*, vol. 44, no. 7, pp. 1770–1773, 2019.

[13] L. Xu, Y. Wang, E. El-Fiky, D. Mao, A. Kumar, Z. Xing, M. G. Saber, M. Jacques, and D. V. Plant, "Compact broadband polarization beam splitter based on multimode interference coupler with internal photonic crystal for the SOI platform," *Journal of Lightwave Technology*, vol. 37, no. 4, pp. 1231–1240, 2019.

[14] L. Xu, Y. Wang, A. Kumar, E. El-Fiky, D. Mao, H. Tamazin, M. Jacques, Z. Xing, M. G. Saber, and D. V. Plant, "Compact high-performance adiabatic 3-dB coupler enabled by subwavelength grating slot in the silicon-on-insulator platform," *Optics Express*, vol. 26, no. 23, pp. 29 873–29 885, 2018.

[15] L. Xu, D. Mao, J. Zhang, Y. Wang, Z. Xing, M. S. Alam, M. Jacques, Y. D'Mello, S. Bernal, and D. V. Plant, "Broadband polarization beam splitters based on MMI couplers with internal photonic crystals fabricated using 193 nm photolithography," in *Optical Fiber Communications Conference and Exhibition*, 2021, pp. 1–3.

[16] M. S. Alam, A. Abdo, D. Mao, M. Parvizi, N. Ben-Hamida, and D. V. Plant, "Timing phase recovery in digital multi-subcarrier coherent optical communication," in *Photonics North*, 2021, pp. 1–1.

[17] L. Xu, Y. Wang, D. Mao, J. Zhang, M. S. Alam, Z. Xing, M. Jacques, Y. D'Mello, S. Bernal, S. Lessard, and D. V. Plant, "Broadband 2×2 adiabatic 3-dB coupler

with inversely-tapered mode-evolution region for the silicon-on-insulator platform," in *IEEE Photonics Conference*, 2020, pp. 1–2.

[18] Cisco Annual Internet Report (2018-2023) white paper. [Online]. Available: https://www.cisco.com/c/en/us/solutions/collateral/executive-perspectives/annual-internet-report/white-paper-c11-741490.html

[19] X. Liu, *Optical Communications in the 5G Era.* Academic Press, 2021.

[20] L. Chrostowski and M. Hochberg, *Silicon Photonics Design: from devices to systems.* Cambridge University Press, 2015.

[21] E. El-Fiky, A. Samani, D. Patel, M. Jacques, M. Sowailem, and D. V. Plant, "400 Gb/s O-band silicon photonic transmitter for intra-datacenter optical interconnects," *Optics Express*, vol. 27, no. 7, pp. 10 258–10 268, 2019.

[22] D. Che, A. Li, X. Chen, Q. Hu, Y. Wang, and W. Shieh, "Stokes vector direct detection for short-reach optical communication," *Optics Letters*, vol. 39, no. 11, pp. 3110–3113, 2014.

[23] M. Morsy-Osman, M. Chagnon, M. Poulin, S. Lessard, and D. V. Plant, "$1\lambda\times224$ Gb/s 10 km transmission of polarization division multiplexed PAM-4 signals using 1.3 μm SiP intensity modulator and a direct-detection MIMO-based receiver," in *European Conference on Optical Communication*, 2014, pp. 1–3.

[24] M. A. Tran, C. Zhang, and J. E. Bowers, "A broadband optical switch based on adiabatic couplers," in *IEEE Photonics Conference*, 2016, pp. 755–756.

[25] D. Patel, S. Ghosh, M. Chagnon, A. Samani, V. Veerasubramanian, M. Osman, and D. V. Plant, "Design, analysis, and transmission system performance of a 41 GHz silicon photonic modulator," *Optics Express*, vol. 23, no. 11, pp. 14 263–14 287, 2015.

[26] A. N. Tait, T. F. De Lima, E. Zhou, A. X. Wu, M. A. Nahmias, B. J. Shastri, and P. R. Prucnal, "Neuromorphic photonic networks using silicon photonic weight banks," *Scientific Reports*, vol. 7, no. 1, pp. 1–10, 2017.

[27] D. Dai and S. Wang, "Asymmetric directional couplers based on silicon nanophotonic waveguides and applications," *Frontiers of Optoelectronics*, vol. 9, no. 3, pp. 450–465, 2016.

[28] D. Dai and J. E. Bowers, "Novel ultra-short and ultra-broadband polarization beam splitter based on a bent directional coupler," *Optics Express*, vol. 19, no. 19, pp. 18 614–18 620, 2011.

[29] D. Dai, Z. Wang, and J. E. Bowers, “Ultra-short broad-band polarization beam splitter based on an asymmetrical directional coupler,” *Optics Letters*, vol. 36, no. 13, pp. 2590–2592, 2011.

[30] Z. Lu, H. Yun, Y. Wang, Z. Chen, F. Zhang, N. A. F. Jaeger, and L. Chrostowski, “Broadband silicon photonic directional coupler using asymmetric-waveguide based phase control,” *Optics Express*, vol. 23, no. 3, pp. 3795–3808, 2015.

[31] Y. Wang, Z. Lu, M. Ma, H. Yun, F. Zhang, N. A. F. Jaeger, and L. Chrostowski, “Compact broadband directional couplers using subwavelength gratings,” *IEEE Photonics Journal*, vol. 8, no. 3, pp. 1–8, 2016.

[32] E. El-Fiky, Y. D’Mello, Y. Wang, J. Skoric, M. G. Saber, A. Kumar, A. Samani, L. Xu, R. Li, D. Patel, and D. V. Plant, “Ultra-broadband and compact asymmetrical beam splitter enabled by angled sub-wavelength grating MMI,” in *Conference on Lasers and Electro-Optics*, San Jose, CA, USA, 2018, pp. STh4A–7.

[33] T. Tamir, *Guided-wave optoelectronics.* Springer Berlin, Heidelberg, 1988.

[34] Y. Wang, L. Xu, H. Yun, M. Ma, A. Kumar, E. El-Fiky, R. Li, N. Abadíacalvo, L. Chrostowski, N. A. F. Jaeger, and D. V. Plant, “Polarization-independent mode-evolution-based coupler for the silicon-on-insulator platform,” *IEEE Photonics Journal*, vol. 10, no. 3, pp. 1–10, 2018.

[35] H. Yun, Y. Wang, F. Zhang, Z. Lu, S. Lin, L. Chrostowski, and N. A. F. Jaeger, “Broadband 2× 2 adiabatic 3 dB coupler using silicon-on-insulator sub-wavelength grating waveguides,” *Optics Letters*, vol. 41, no. 13, pp. 3041–3044, 2016.

[36] D. Dai and J. E. Bowers, “Silicon-based on-chip multiplexing technologies and devices for peta-bit optical interconnects,” *Nanophotonics*, vol. 3, no. 4-5, pp. 283–311, 2014.

[37] S. Park, K.-J. Kim, I.-G. Kim, and G. Kim, “Si micro-ring MUX/DeMUX WDM filters,” *Optics Express*, vol. 19, no. 14, pp. 13 531–13 539, 2011.

[38] D. Dai, J. Bauters, and J. E. Bowers, “Passive technologies for future large-scale photonic integrated circuits on silicon: polarization handling, light non-reciprocity and loss reduction,” *Light: Science & Applicatoins*, vol. 1, no. 3, pp. e1–e1, 2012.

[39] F. Horst, W. M. Green, S. Assefa, S. M. Shank, Y. A. Vlasov, and B. J. Offrein, “Cascaded Mach-Zehnder wavelength filters in silicon photonics for low loss and flat pass-band WDM (de-) multiplexing,” *Optics Express*, vol. 21, no. 10, pp. 11 652–11 658, 2013.

[40] H. Xu and Y. Shi, “Flat-top CWDM (de-)multiplexer based on MZI with bent directional couplers,” *IEEE Photonics Technology Letters*, vol. 30, no. 2, pp. 169–172, 2017.

[41] L. Chang, Y. Gong, L. Liu, Z. Li, and Y. Yu, “Low-loss broadband silicon-on-insulator demultiplexers in the O-band,” *IEEE Photonics Technology Letters*, vol. 29, no. 15, pp. 1237–1240, 2017.

[42] G. T. Reed, G. Mashanovich, F. Y. Gardes, and D. Thomson, “Silicon optical modulators,” *Nature Photonics*, vol. 4, no. 8, pp. 518–526, 2010.

[43] J. Sun, R. Kumar, M. Sakib, J. B. Driscoll, H. Jayatilleka, and H. Rong, “A 128 Gb/s PAM4 silicon microring modulator with integrated thermo-optic resonance tuning,” *Journal of Lightwave Technology*, vol. 37, no. 1, pp. 110–115, 2018.

[44] Y. Hinakura, D. Akiyama, H. Ito, and T. Baba, “Silicon photonic crystal modulators for high-speed transmission and wavelength division multiplexing,” *IEEE Journal of Selected Topics in Quantum Electronics*, vol. 27, no. 3, pp. 1–8, 2020.

[45] O. Jafari, H. Sepehrian, W. Shi, and S. LaRochelle, “High-efficiency silicon photonic modulator using coupled Bragg grating resonators,” *Journal of Lightwave Technology*, vol. 37, no. 9, pp. 2065–2075, 2019.

[46] G. Cong, Y. Maegami, M. Ohno, and K. Yamada, “Ultra-compact non-travelling-tave silicon carrier-depletion Mach-Zehnder modulators towards high channel density integration,” *IEEE Journal of Selected Topics in Quantum Electronics*, vol. 27, no. 3, pp. 1–11, 2020.

[47] D. Taillaert, H. Chong, P. Borel, L. Frandsen, R. De La Rue, and R. Baets, “A compact two-dimensional grating coupler used as a polarization splitter,” *IEEE Photonics Technology Letters*, vol. 15, no. 9, pp. 1249–1251, 2003.

[48] D.-X. Xu, J. H. Schmid, G. T. Reed, G. Z. Mashanovich, D. J. Thomson, M. Nedeljkovic, X. Chen, D. Van Thourhout, S. Keyvaninia, and S. K. Selvaraja, “Silicon photonic integration platform—have we found the sweet spot?” *IEEE Journal of Selected Topics in Quantum Electronics*, vol. 20, no. 4, pp. 189–205, 2014.

[49] K. E. Oughstun and N. A. Cartwright, “On the Lorentz-Lorenz formula and the Lorentz model of dielectric dispersion,” *Optics Express*, vol. 11, no. 13, pp. 1541–1546, 2003.

[50] C. Pollock and M. Lipson, *Integrated Photonics.* Springer, 2003, vol. 20, no. 25.

[51] A. Maese-Novo, R. Halir, S. Romero-García, D. Pérez-Galacho, L. Zavargo-Peche, A. Ortega-Moñux, I. Molina-Fernández, J. Wangüemert-Pérez, and P. Cheben, "Wavelength independent multimode interference coupler," *Optics Express*, vol. 21, no. 6, pp. 7033–7040, 2013.

[52] A. Ortega-Moñux, C. Alonso-Ramos, A. Maese-Novo, R. Halir, L. Zavargo-Peche, D. Pérez-Galacho, I. Molina-Fernández, J. G. Wangüemert-Pérez, P. Cheben, J. H. Schmid, J. Lapointe, D. Xu, and S. Janz, "An ultra-compact multimode interference coupler with a subwavelength grating slot," *Laser & Photonics Reviews*, vol. 7, no. 2, pp. L12–L15, 2013.

[53] R. Halir, P. Cheben, J. M. Luque-González, J. D. Sarmiento-Merenguel, J. H. Schmid, G. Wangüemert-Pérez, D.-X. Xu, S. Wang, A. Ortega-Moñux, and Í. Molina-Fernández, "Ultra-broadband nanophotonic beamsplitter using an anisotropic subwavelength metamaterial," *Laser & Photonics Reviews*, vol. 10, no. 6, pp. 1039–1046, 2016.

[54] P. Dumais, Y. Wei, M. Li, F. Zhao, X. Tu, J. Jiang, D. Celo, D. J. Goodwill, H. Fu, D. Geng, and E. Bernier, "2×2 Multimode interference coupler with low loss using 248 nm photolithography," in *Optical Fiber Communications Conference and Exhibition*, 2016, pp. W2A–19.

[55] D. Thomson, Y. Hu, G. Reed, and J.-M. Fedeli, "Low loss MMI couplers for high performance MZI modulators," *IEEE Photonics Technology Letters*, vol. 22, no. 20, pp. 1485–1487, 2010.

[56] A. Hosseini, D. N. Kwong, Y. Zhang, H. Subbaraman, X. Xu, and R. T. Chen, "1×N multimode interference beam splitter design techniques for on-chip optical interconnections," *IEEE Journal of Selected Topics in Quantum Electronics*, vol. 17, no. 3, pp. 510–515, 2011.

[57] Z. Sheng, Z. Wang, C. Qiu, L. Li, A. Pang, A. Wu, X. Wang, S. Zou, and F. Gan, "A compact and CMOS compatible MMI coupler with very low excess loss," in *Optical Fiber Communications Conference and Exhibition*, 2013, pp. 1–3.

[58] Q. Deng, L. Liu, X. Li, and Z. Zhou, "Arbitrary-ratio 1×2 power splitter based on asymmetric multimode interference," *Optics Letters*, vol. 39, no. 19, pp. 5590–5593, 2014.

[59] A. Zanzi, A. Brimont, A. Griol, P. Sanchis, and J. Marti, "Compact and low-loss asymmetrical multimode interference splitter for power monitoring applications," *Optics Letters*, vol. 41, no. 2, pp. 227–229, 2016.

[60] K. Voigt, L. Zimmermann, G. Winzer, K. Petermann, and C. Weinert, “Silicon-on-insulator 90º optical hybrid using 4×4 waveguide couplers with C-band operation,” in *European Conference on Optical Communication*, 2008, pp. 1–2.

[61] L. Zimmermann, K. Voigt, G. Winzer, K. Petermann, and C. M. Weinert, “C-band optical 90°-hybrids based on silicon-on-insulator 4×4 waveguide couplers,” *IEEE Photonics Technology Letters*, vol. 21, no. 3, pp. 143–145, 2009.

[62] R. Halir, G. Roelkens, A. O.-M. nux, and J. G. Wangüemert-Pérez, “High-performance 90° hybrid based on a silicon-on-insulator multimode interference coupler,” *Optics Letters*, vol. 36, no. 2, pp. 178–180, 2011.

[63] A. Ortega-Monux, L. Zavargo-Peche, A. Maese-Novo, I. Molina-Fernandez, R. Halir, J. G. Wanguemert-Perez, P. Cheben, and J. H. Schmid, “High-performance multimode interference coupler in silicon waveguides with subwavelength structures,” *IEEE Photonics Technology Letters*, vol. 23, no. 19, pp. 1406–1408, 2011.

[64] K. Voigt, L. Zimmermann, G. Winzer, H. Tian, B. Tillack, and K. Petermann, “C-band optical 90° hybrids in silicon nanowaveguide technology,” *IEEE Photonics Technology Letters*, vol. 23, no. 23, pp. 1769–1771, 2011.

[65] W. Yang, M. Yin, Y. Li, X. Wang, and Z. Wang, “Ultra-compact optical 90° hybrid based on a wedge-shaped 2 × 4 MMI coupler and a 2 × 2 MMI coupler in silicon-on-insulator,” *Optics Express*, vol. 21, no. 23, pp. 28 423–28 431, 2013.

[66] T. Föhn, W. Vogel, M. Schmidt, M. Berroth, J. Butschke, and F. Letzkus, “Optimized 90° hybrids with sidewall grating in silicon on insulator,” in *Optical Fiber Communications Conference and Exhibition*, 2014, p. Th3F.4.

[67] H. Guan, Y. Ma, R. Shi, X. Zhu, R. Younce, Y. Chen, J. Roman, N. Ophir, Y. Liu, R. Ding, T. Baehr-Jones, K. Bergman, and M. Hochberg, “Compact and low loss 90º optical hybrid on a silicon-on-insulator platform,” *Optics Express*, vol. 25, no. 23, pp. 28 957–28 968, 2017.

[68] L. Xu, Y. Wang, D. Patel, M. Morsy-Osman, R. Li, M. Hui, M. Parvizi, N. Ben-Hamida, and D. V. Plant, “Ultra-broadband and ultra-compact optical 90° hybrid based on 2×4 MMI coupler with subwavelength gratings on silicon-on-insulator,” in *Optical Fiber Communications Conference and Exhibition*, 2018, p. M3I.7.

[69] Y. Huang, Z. Tu, H. Yi, Y. Li, X. Wang, and W. Hu, “High extinction ratio polarization beam splitter with multimode interference coupler on SOI,” *Optics Communications*, vol. 307, no. 15, pp. 46–49, 2013.

[70] M. Yin, W. Yang, Y. Li, X. Wang, and H. Li, "CMOS-compatible and fabrication-tolerant MMI-based polarization beam splitter," *Optics Communications*, vol. 335, pp. 48–52, 2015.

[71] W. Yang, Y. Xu, Y. Li, X. Wang, and Z. Wang, "A compact and wide-band polarization beam splitter based on wedge-shaped MMI coupler in silicon-on-insulator," in *Optical Fiber Communications Conference and Exhibition*, 2015, p. W2A.12.

[72] E. El-Fiky, A. Samani, D. Patel, and D. V. Plant, "A high extinction ratio, broadband, and compact polarization beam splitter enabled by cascaded MMIs on silicon-on-insulator," in *Optical Fiber Communications Conference and Exhibition*, 2016, p. W2A.8.

[73] Y. D'Mello, E. El-Fiky, J. Skoric, A. Kumar, M. Hui, Y. Wang, L. Guenin, D. Patel, and D. V. Plant, "Compact, angled polarization splitter: Characterization of broadband performance and fabrication tolerance," *IEEE Photonics Journal*, vol. 10, no. 6, pp. 1–12, 2018.

[74] L. B. Soldano and E. C. Pennings, "Optical multi-mode interference devices based on self-imaging: principles and applications," *Journal of Lightwave Technology*, vol. 13, no. 4, pp. 615–627, 1995.

[75] O. Bryngdahl, "Image formation using self-imaging techniques," *Journal of the Optical Society of America*, vol. 63, no. 4, pp. 416–419, 1973.

[76] R. Ulrich, "Image formation by phase coincidences in optical waveguides," *Optics Communications*, vol. 13, no. 3, pp. 259–264, 1975.

[77] L. Cao, A. Elshaari, A. Aboketaf, and S. Preble, "Adiabatic couplers in SOI waveguides," in *Conference on Lasers and Electro-Optics*, 2010, p. CThAA2.

[78] H. Yun, W. Shi, Y. Wang, L. Chrostowski, and N. A. F. Jaeger, "2×2 adiabatic 3-dB coupler on silicon-on-insulator rib waveguides," in *Photonics North*, vol. 8915, Ottawa, ON, Canada, 2013, p. 89150V.

[79] J. Xing, K. Xiong, H. Xu, Z. Li, X. Xiao, J. Yu, and Y. Yu, "Silicon-on-insulator-based adiabatic splitter with simultaneous tapering of velocity and coupling," *Optics Letters*, vol. 38, no. 13, pp. 2221–2223, 2013.

[80] J. Xing, Z. Li, Y. Yu, and J. Yu, "Design of polarization-independent adiabatic splitters fabricated on silicon-on-insulator substrates," *Optics Express*, vol. 21, no. 22, pp. 26 729–26 734, 2013.

[81] H. Yun, Z. Lu, Y. Wang, W. Shi, L. Chrostowski, and N. A. F. Jaeger, "2×2 broadband adiabatic 3-dB couplers on SOI strip waveguides for TE and TM modes," in *Conference on Lasers and Electro-Optics*, San Jose, CA, USA, 2015, pp. STh1F–8.

[82] L. Xu, Y. Wang, D. Patel, E. El-Fiky, Z. Xing, R. Li, M. G. Saber, M. Jacques, and D. V. Plant, "Polarization independent adiabatic 3-dB coupler for silicon-on-insulator," in *Conference on Lasers and Electro-Optics*, 2017, pp. 1–2.

[83] H. Yun, L. Chrostowski, and N. A. F. Jaeger, "Ultra-broadband 2×2 adiabatic 3 dB coupler using subwavelength-grating-assisted silicon-on-insulator strip waveguides," *Optics Letters*, vol. 43, no. 8, pp. 1935–1938, 2018.

[84] D. Guo and T. Chu, "Compact broadband silicon 3 dB coupler based on shortcuts to adiabaticity," *Optics Letters*, vol. 43, no. 19, pp. 4795–4798, 2018.

[85] Y.-J. Hung, Z.-Y. Li, H.-C. Chung, F.-C. Liang, M.-Y. Jung, T.-H. Yen, and S.-Y. Tseng, "Mode-evolution-based silicon-on-insulator 3 dB coupler using fast quasiadiabatic dynamics," *Optics Letters*, vol. 44, no. 4, pp. 815–818, 2019.

[86] W. D. Sacher, T. Barwicz, and J. K. Poon, "Silicon-on-insulator polarization splitter-rotator based on $\mathrm{TM_0}$-$\mathrm{TE_1}$ mode conversion in a bi-level taper," in *Conference on Lasers and Electro-Optics*, 2013, pp. 1–2.

[87] W. D. Sacher, T. Barwicz, B. J. Taylor, and J. K. Poon, "Polarization rotator-splitters in standard active silicon photonics platforms," *Optics Express*, vol. 22, no. 4, pp. 3777–3786, 2014.

[88] W. D. Sacher, Y. Huang, L. Ding, T. Barwicz, J. C. Mikkelsen, B. J. Taylor, G.-Q. Lo, and J. K. Poon, "Polarization rotator-splitters and controllers in a $\mathrm{Si_3N_4}$-on-SOI integrated photonics platform," *Optics Express*, vol. 22, no. 9, pp. 11 167–11 174, 2014.

[89] W. D. Sacher, Y. Huang, D. Liang, T. Barwicz, J. C. Mikkelsen, B. J. Taylor, G.-Q. Lo, and J. K. Poon, "$\mathrm{Si_3N_4}$-on-SOI polarization rotator-splitter based on $\mathrm{TM_0}$-$\mathrm{TE_1}$ mode conversion," in *Optical Fiber Communications Conference and Exhibition*, 2014, pp. Th1A–3.

[90] L. Socci, V. Sorianello, and M. Romagnoli, "300 nm bandwidth adiabatic SOI polarization splitter-rotators exploiting continuous symmetry breaking," *Optics Express*, vol. 23, no. 15, pp. 19 261–19 271, 2015.

[91] X. Tu, M. Li, J. Xing, H. Fu, and D. Geng, "Compact PSR based on an asymmetric bi-level lateral taper in an adiabatic directional coupler," *Journal of Lightwave Technology*, vol. 34, no. 3, pp. 985–991, 2016.

[92] C. Sun, Y. Yu, G. Chen, and X. Zhang, "A low crosstalk and broadband polarization rotator and splitter based on adiabatic couplers," *IEEE Photonics Technology Letters*, vol. 28, no. 20, pp. 2253–2256, 2016.

[93] Y. Yin, Z. Li, and D. Dai, "Ultra-broadband polarization splitter-rotator based on the mode evolution in a dual-core adiabatic taper," *Journal of Lightwave Technology*, vol. 35, no. 11, pp. 2227–2233, 2017.

[94] H.-C. Chung and S.-Y. Tseng, "Ultrashort and broadband silicon polarization splitter-rotator using fast quasiadiabatic dynamics," *Optics Express*, vol. 26, no. 8, pp. 9655–9665, 2018.

[95] K. Yu, L. Wang, W. Wu, Y. Luo, and Y. Yu, "Demonstration of an on-chip broadband polarization splitter and rotator using counter-tapered coupler," *Optics Communications*, vol. 431, pp. 58–62, 2019.

[96] E. El-Fiky, Y. Wang, S. Bernal, C. Gamache, E. Panorel, A. Kumar, A. Samani, M. Jacques, P.-C. Koh, and D. V. Plant, "High extinction ratio and broadband O-band polarization splitter and rotator on silicon-on-insulator," in *Optical Fiber Communications Conference and Exhibition*, 2019, pp. 1–3.

[97] J. Xing, Z. Li, X. Xiao, J. Yu, and Y. Yu, "Two-mode multiplexer and demultiplexer based on adiabatic couplers," *Optics Letters*, vol. 38, no. 17, pp. 3468–3470, 2013.

[98] J. Wang, Y. Xuan, M. Qi, H. Huang, Y. Li, M. Li, X. Chen, Z. Sheng, A. Wu, W. Li, X. Wang, S. Zou, and F. Gan, "Broadband and fabrication-tolerant on-chip scalable mode-division multiplexing based on mode-evolution counter-tapered couplers," *Optics Letters*, vol. 40, no. 9, pp. 1956–1959, 2015.

[99] C. Sun, Y. Yu, G. Chen, and X. Zhang, "Silicon mode multiplexer processing dual-path mode-division multiplexing signals," *Optics Letters*, vol. 41, no. 23, pp. 5511–5514, 2016.

[100] C. Sun, Y. Yu, M. Ye, G. Chen, and X. Zhang, "An ultra-low crosstalk and broadband two-mode (de-)multiplexer based on adiabatic couplers," *Scientific Reports*, vol. 6, no. 1, pp. 1–6, 2016.

[101] Z. Zhang, Y. Yu, and S. Fu, "Broadband on-chip mode-division multiplexer based on adiabatic couplers and symmetric Y-junction," *IEEE Photonics Journal*, vol. 9, no. 2, pp. 1–6, 2017.

[102] D. Guo and T. Chu, "Silicon mode (de-)multiplexers with parameters optimized using shortcuts to adiabaticity," *Optics Express*, vol. 25, no. 8, pp. 9160–9170, 2017.

[103] Y. Tan, H. Wu, S. Wang, C. Li, and D. Dai, "Silicon-based hybrid demultiplexer for wavelength-and mode-division multiplexing," *Optics Letters*, vol. 43, no. 9, pp. 1962–1965, 2018.

[104] D. Dai, C. Li, S. Wang, H. Wu, Y. Shi, Z. Wu, S. Gao, T. Dai, H. Yu, and H.-K. Tsang, "10-Channel mode (de-)multiplexer with dual polarizations," *Laser & Photonics Reviews*, vol. 12, no. 1, p. 1700109, 2018.

[105] A. Syahriar, V. M. Schneider, and S. Al-Bader, "The design of mode evolution couplers," *Journal of Lightwave Technology*, vol. 16, no. 10, pp. 1907–1914, 1998.

[106] C.-P. Ho and S.-Y. Tseng, "Optimization of adiabaticity in coupled-waveguide devices using shortcuts to adiabaticity," *Optics Letters*, vol. 40, no. 21, pp. 4831–4834, 2015.

[107] D. Liu, H. Xu, Y. Tan, Y. Shi, and D. Dai, "Silicon photonic filters," *Microwave and Optical Technology Letters*, vol. 63, no. 9, pp. 2252–2268, 2021.

[108] W. Bogaerts, P. De Heyn, T. Van Vaerenbergh, K. De Vos, S. Kumar Selvaraja, T. Claes, P. Dumon, P. Bienstman, D. Van Thourhout, and R. Baets, "Silicon microring resonators," *Laser & Photonics Reviews*, vol. 6, no. 1, pp. 47–73, 2012.

[109] B. E. Little, S. T. Chu, H. A. Haus, J. Foresi, and J.-P. Laine, "Microring resonator channel dropping filters," *Journal of Lightwave Technology*, vol. 15, no. 6, pp. 998–1005, 1997.

[110] F. Xia, M. Rooks, L. Sekaric, and Y. Vlasov, "Ultra-compact high order ring resonator filters using submicron silicon photonic wires for on-chip optical interconnects," *Optics Express*, vol. 15, no. 19, pp. 11 934–11 941, 2007.

[111] P. Chen, S. Chen, X. Guan, Y. Shi, and D. Dai, "High-order microring resonators with bent couplers for a box-like filter response," *Optics Letters*, vol. 39, no. 21, pp. 6304–6307, 2014.

[112] M. S. Nawrocka, T. Liu, X. Wang, and R. R. Panepucci, "Tunable silicon microring resonator with wide free spectral range," *Applied Physics Letters*, vol. 89, no. 7, p. 071110, 2006.

[113] Q. Xu, D. Fattal, and R. G. Beausoleil, "Silicon microring resonators with 1.5-μm radius," *Optics Express*, vol. 16, no. 6, pp. 4309–4315, 2008.

[114] D. Liu, C. Zhang, D. Liang, and D. Dai, "Submicron-resonator-based add-drop optical filter with an ultra-large free spectral range," *Optics Express*, vol. 27, no. 2, pp. 416–422, 2019.

[115] A. D. Simard and S. LaRochelle, “Complex apodized Bragg grating filters without circulators in silicon-on-insulator,” *Optics Express*, vol. 23, no. 13, pp. 16 662–16 675, 2015.

[116] J. Wang and L. R. Chen, “Low crosstalk Bragg grating/Mach-Zehnder interferometer optical add-drop multiplexer in silicon photonics,” *Optics Express*, vol. 23, no. 20, pp. 26 450–26 459, 2015.

[117] W. Shi, X. Wang, C. Lin, H. Yun, Y. Liu, T. Baehr-Jones, M. Hochberg, N. A. Jaeger, and L. Chrostowski, “Silicon photonic grating-assisted, contra-directional couplers,” *Optics Express*, vol. 21, no. 3, pp. 3633–3650, 2013.

[118] J. Jiang, H. Qiu, G. Wang, Y. Li, T. Dai, D. Mu, H. Yu, J. Yang, and X. Jiang, “Silicon lateral-apodized add–drop filter for on-chip optical interconnection,” *Applied Optics*, vol. 56, no. 30, pp. 8425–8429, 2017.

[119] H. Qiu, J. Jiang, T. Hu, P. Yu, J. Yang, X. Jiang, and H. Yu, “Silicon add-drop filter based on multimode Bragg sidewall gratings and adiabatic couplers,” *Journal of Lightwave Technology*, vol. 35, no. 9, pp. 1705–1709, 2017.

[120] D. Liu, M. Zhang, Y. Shi, and D. Dai, “Four-channel CWDM (de-)multiplexers using cascaded multimode waveguide gratings,” *IEEE Photonics Technology Letters*, vol. 32, no. 4, pp. 192–195, 2020.

[121] W. Shi, H. Yun, C. Lin, M. Greenberg, X. Wang, Y. Wang, S. T. Fard, J. Flueckiger, N. A. F. Jaeger, and L. Chrostowski, “Ultra-compact, flat-top demultiplexer using anti-reflection contra-directional couplers for CWDM networks on silicon,” *Optics Express*, vol. 21, no. 6, pp. 6733–6738, 2013.

[122] S. Pathak, P. Dumon, D. Van Thourhout, and W. Bogaerts, “Comparison of AWGs and echelle gratings for wavelength division multiplexing on silicon-on-insulator,” *IEEE Photonics Journal*, vol. 6, no. 5, pp. 1–9, 2014.

[123] J. Zou, X. Jiang, X. Xia, T. Lang, and J.-J. He, “Ultra-compact birefringence-compensated arrayed waveguide grating triplexer based on silicon-on-insulator,” *Journal of Lightwave Technology*, vol. 31, no. 12, pp. 1935–1940, 2013.

[124] S. Chen, X. Fu, J. Wang, Y. Shi, S. He, and D. Dai, “Compact dense wavelength-division (de-)multiplexer utilizing a bidirectional arrayed-waveguide grating integrated with a Mach–Zehnder interferometer,” *Journal of Lightwave Technology*, vol. 33, no. 11, pp. 2279–2285, 2015.

[125] S. Chen, Y. Shi, S. He, and D. Dai, “Compact monolithically-integrated hybrid (de-)multiplexer based on silicon-on-insulator nanowires for PDM-WDM systems,” *Optics Express*, vol. 23, no. 10, pp. 12 840–12 849, 2015.

[126] D. Dai, X. Fu, Y. Shi, and S. He, “Experimental demonstration of an ultracompact Si-nanowire-based reflective arrayed-waveguide grating (de-)multiplexer with photonic crystal reflectors,” *Optics Letters*, vol. 35, no. 15, pp. 2594–2596, 2010.

[127] W. Bogaerts, P. Dumon, D. Van Thourhout, D. Taillaert, P. Jaenen, J. Wouters, S. Beckx, V. Wiaux, and R. G. Baets, “Compact wavelength-selective functions in silicon-on-insulator photonic wires,” *IEEE Journal of Selected Topics in Quantum Electronics*, vol. 12, no. 6, pp. 1394–1401, 2006.

[128] P. Xing and J. Viegas, “Broadband CMOS-compatible SOI temperature insensitive Mach-Zehnder interferometer,” *Optics Express*, vol. 23, no. 19, pp. 24 098–24 107, 2015.

[129] Q. Deng, L. Liu, R. Zhang, X. Li, J. Michel, and Z. Zhou, “Athermal and flat-topped silicon Mach-Zehnder filters,” *Optics Express*, vol. 24, no. 26, pp. 29 577–29 582, 2016.

[130] U. A. Korai, A. H. Bermello, M. J. Strain, I. Glesk, and A. V. Velasco, “Design of an athermal interferometer based on tailored subwavelength metamaterials for on-chip microspectrometry,” *IEEE Photonics Journal*, vol. 11, no. 6, pp. 1–11, 2019.

[131] S.-H. Jeong, D. Shimura, T. Simoyama, T. Horikawa, Y. Tanaka, and K. Morito, “Si-nanowire-based multistage delayed Mach–Zehnder interferometer optical MUX/DeMUX fabricated by an ArF-immersion lithography process on a 300 mm SOI wafer,” *Optics Letters*, vol. 39, no. 13, pp. 3702–3705, 2014.

[132] D. Munk, M. Katzman, Y. Kaganovskii, N. Inbar, A. Misra, M. Hen, M. Priel, M. Feldberg, M. Tkachev, A. Bergman, M. Vofsi, M. Rosenbluh, T. Schneider, and A. Zadok, “Eight-channel silicon-photonic wavelength division multiplexer with 17 GHz spacing,” *IEEE Journal of Selected Topics in Quantum Electronics*, vol. 25, no. 5, pp. 1–10, 2019.

[133] L. Zhang, H. Zhao, H. Wang, S. Shao, W. Tian, J. Ding, X. Fu, and L. Yang, “Cascading second-order microring resonators for a box-like filter response,” *Journal of Lightwave Technology*, vol. 35, no. 24, pp. 5347–5360, 2017.

[134] M. Huang, S. Li, M. Xue, L. Zhao, and S. Pan, “Flat-top optical resonance in a single-ring resonator based on manipulation of fast-and slow-light effects,” *Optics Express*, vol. 26, no. 18, pp. 23 215–23 220, 2018.

[135] G. Brunetti, F. Dell’Olio, D. Conteduca, M. N. Armenise, and C. Ciminelli, “Ultra-compact tunable notch filter using silicon photonic crystal ring resonator,” *Journal of Lightwave Technology*, vol. 37, no. 13, pp. 2970–2980, 2019.

[136] J. Wang and L. R. Chen, "Low crosstalk Bragg grating/Mach-Zehnder interferometer optical add-drop multiplexer in silicon photonics," *Optics Express*, vol. 23, no. 20, pp. 26 450–26 459, 2015.

[137] B. Naghdi and L. R. Chen, "Silicon photonic contradirectional couplers using subwavelength grating waveguides," *Optics Express*, vol. 24, no. 20, pp. 23 429–23 438, 2016.

[138] D. Dai, L. Liu, L. Wosinski, and S. He, "Design and fabrication of an ultrasmall overlapped AWG demultiplexers based on α-si nanowire waveguides," *Electronics Letters*, vol. 42, no. 7, pp. 400–402, 2006.

[139] A. Bernussi, L. G. de Peralta, V. Gorbounov, J. Linn, S. Frisbie, R. Gale, and H. Temkin, "Mirror quality and the performance of reflective arrayed-waveguide grating multiplexers," *Journal of Lightwave Technology*, vol. 22, no. 7, p. 1828, 2004.

[140] J. Brouckaert, W. Bogaerts, P. Dumon, D. Van Thourhout, and R. Baets, "Planar concave grating demultiplexer fabricated on a nanophotonic silicon-on-insulator platform," *Journal of Lightwave Technology*, vol. 25, no. 5, pp. 1269–1275, 2007.

[141] P. Dong, "Silicon photonic integrated circuits for wavelength-division multiplexing applications," *IEEE Journal of Selected Topics in Quantum Electronics*, vol. 22, no. 6, pp. 370–378, 2016.

[142] L. Chen, C. R. Doerr, and Y.-k. Chen, "Polarization-diversified DWDM receiver on silicon free of polarization-dependent wavelength shift," in *Optical Fiber Communications Conference and Exhibition*, 2012, pp. 1–3.

[143] C. K. Madsen and J. H. Zhao, *Optical filter design and analysis.* Wiley New York, 1999.

[144] V. Raghunathan, N. Y. Winnie, J. Hu, T. Izuhara, J. Michel, and L. Kimerling, "Athermal operation of silicon waveguides: spectral, second order and footprint dependencies," *Optics Express*, vol. 18, no. 17, pp. 17 631–17 639, 2010.

[145] G. Gao, D. Chen, S. Tao, Y. Zhang, S. Zhu, X. Xiao, and J. Xia, "Silicon nitride O-band (de-)multiplexers with low thermal sensitivity," *Optics Express*, vol. 25, no. 11, pp. 12 260–12 267, 2017.

[146] T. Akiyama, S. Oda, S.-H. Jeong, Y. Nakasha, A. Hayakawa, Y. Tanaka, and T. Hoshida, "An extremely low-crosstalk WDM demultiplexer with an automatic error-correction capability enabling temperature insensitivity and high-yield integration on low-end Si PICs," in *European Conference on Optical Communication*, 2019, pp. 1–4.

[147] S. Dwivedi, H. D'heer, and W. Bogaerts, "A compact all-silicon temperature insensitive filter for WDM and bio-sensing applications," *IEEE Photonics Technology Letters*, vol. 25, no. 22, pp. 2167–2170, Sept. 2013.

[148] P. Xing and J. Viegas, "Broadband CMOS-compatible SOI temperature insensitive Mach-Zehnder interferometer," *Optics Express*, vol. 23, no. 19, pp. 24 098–24 107, 2015.

[149] K. Hassan, C. Sciancalepore, J. Harduin, T. Ferrotti, S. Menezo, and B. B. Bakir, "Toward athermal silicon-on-insulator (de-)multiplexers in the O-band," *Optics Letters*, vol. 40, no. 11, pp. 2641–2644, June 2015.

[150] M. Uenuma and T. Motooka, "Temperature-independent silicon waveguide optical filter," *Optics Letters*, vol. 34, no. 5, pp. 599–601, 2009.

[151] B. Guha, A. Gondarenko, and M. Lipson, "Minimizing temperature sensitivity of silicon Mach-Zehnder interferometers," *Optics Express*, vol. 18, no. 3, pp. 1879–1887, 2010.

[152] R. Soref and B. Bennett, "Electrooptical effects in silicon," *IEEE Journal of Quantum Electronics*, vol. 23, no. 1, pp. 123–129, 1987.

[153] M. Nedeljkovic, R. Soref, and G. Z. Mashanovich, "Free-carrier electrorefraction and electroabsorption modulation predictions for silicon over the 1–14- µm infrared wavelength range," *IEEE Photonics Journal*, vol. 3, no. 6, pp. 1171–1180, 2011.

[154] R. F. Pierret and G. W. Neudeck, *Semiconductor fundamentals*. Addison-Wesley Reading, 1988.

[155] H. Yu, D. Patel, W. Liu, Y. Malinge, P. Doussiere, W. Lin, S. Gupta, K. Narayanan, I. Hoshino, M. Bresnehan, S. Sunkoju, D. Mantegazza, R. Herrick, R. Venables, H. Mahalingam, P. Seddighian, A. Fuerst, J. Davis, D. Gold, X. Pan, K. Al-hemyari, A. Agrawal, Y. Li, X. Zheng, M. Geethachar, M. Favaro, D. Zhu, A. Liu, and Y. Akulova, "800 Gbps fully integrated silicon photonics transmitter for data center applications," in *Optical Fiber Communications Conference and Exhibition*, 2022, p. M2D.7.

[156] W. M. Green, M. J. Rooks, L. Sekaric, and Y. A. Vlasov, "Ultra-compact, low RF power, 10 Gb/s silicon Mach-Zehnder modulator," *Optics Express*, vol. 15, no. 25, pp. 17 106–17 113, 2007.

[157] S. Tanaka, T. Simoyama, T. Aoki, T. Mori, S. Sekiguchi, S.-H. Jeong, T. Usuki, Y. Tanaka, and K. Morito, "Ultralow-power (1.59 mW/Gbps), 56-Gbps PAM4 operation of Si photonic transmitter integrating segmented PIN Mach–Zehnder modulator

and 28-nm CMOS driver," *Journal of Lightwave Technology*, vol. 36, no. 5, pp. 1275–1280, 2018.

[158] S. Tanaka and Y. Sobu, "High-speed silicon photonic modulator based on forward-biased PIN diodes and passive equalizers," in *European Conference on Optical Communication*, 2020, pp. 1–4.

[159] M. Jacques, Z. Xing, A. Samani, X. Li, E. El-Fiky, S. Alam, O. Carpentier, P.-C. Koh, and D. V. Plant, "Net 212.5 Gbit/s transmission in O-band with a SiP MZM, one driver and linear equalization," in *Optical Fiber Communications Conference and Exhibition*, 2020, pp. Th4A–3.

[160] D. Patel, *Design, analysis, and performance of a silicon photonic traveling wave Mach-Zehnder modulator.* Master's thesis, McGill University, 2015.

[161] M. Li, L. Wang, X. Li, X. Xiao, and S. Yu, "Silicon intensity Mach-Zehnder modulator for single lane 100 Gb/s applications," *Photonics Research*, vol. 6, no. 2, pp. 109–116, 2018.

[162] J. Witzens, "High-speed silicon photonics modulators," *Proceedings of the IEEE*, vol. 106, no. 12, pp. 2158–2182, 2018.

[163] A. Samani, M. Chagnon, D. Patel, V. Veerasubramanian, S. Ghosh, M. Osman, Q. Zhong, and D. V. Plant, "A low-voltage 35-GHz silicon photonic modulator-enabled 112-Gb/s transmission system," *IEEE Photonics Journal*, vol. 7, no. 3, pp. 1–13, 2015.

[164] H. Sepehrian, J. Lin, L. A. Rusch, and W. Shi, "Silicon photonic IQ modulators for 400 Gb/s and beyond," *Journal of Lightwave Technology*, vol. 37, no. 13, pp. 3078–3086, 2019.

[165] M. Chagnon, M. Osman, M. Poulin, C. Latrasse, J.-F. Gagné, Y. Painchaud, C. Paquet, S. Lessard, and D. Plant, "Experimental study of 112 Gb/s short reach transmission employing PAM formats and SiP intensity modulator at 1.3 μm," *Optics Express*, vol. 22, no. 17, pp. 21 018–21 036, 2014.

[166] A. Samani, E. El-Fiky, M. Morsy-Osman, R. Li, D. Patel, T. Hoang, M. Jacques, M. Chagnon, N. Abadía, and D. V. Plant, "Silicon photonic Mach–Zehnder modulator architectures for on chip PAM-4 signal generation," *Journal of Lightwave Technology*, vol. 37, no. 13, pp. 2989–2999, 2019.

[167] J. Lin, H. Sepehrian, L. A. Rusch, and W. Shi, "Single-carrier 72 Gbaud 32QAM and 84 Gbaud 16QAM transmission using a SiP IQ modulator with joint digital-optical pre-compensation," *Optics Express*, vol. 27, no. 4, pp. 5610–5619, 2019.

[168] D. Patel, A. Samani, V. Veerasubramanian, S. Ghosh, and D. V. Plant, "Silicon photonic segmented modulator-based electro-optic DAC for 100 Gb/s PAM-4 generation," *IEEE Photonics Technology Letters*, vol. 27, no. 23, pp. 2433–2436, 2015.

[169] A. Simard, B. Filion, D. Patel, D. Plant, and S. LaRochelle, "Segmented silicon MZM for PAM-8 transmissions at 114 Gb/s with binary signaling," *Optics Express*, vol. 24, no. 17, pp. 19 467–19 472, 2016.

[170] P. Dong, A. Melikyan, and K. Kim, "Commercializing silicon microring resonators: Technical challenges and potential solutions," in *Conference on Lasers and Electro-Optics*, 2018, pp. SM4B–3.

[171] R. Dubé-Demers, S. LaRochelle, and W. Shi, "Ultrafast pulse-amplitude modulation with a femtojoule silicon photonic modulator," *Optica*, vol. 3, no. 6, pp. 622–627, 2016.

[172] J. Sun, R. Kumar, M. Sakib, J. B. Driscoll, H. Jayatilleka, and H. Rong, "A 128 Gb/s PAM4 silicon microring modulator with integrated thermo-optic resonance tuning," *Journal of Lightwave Technology*, vol. 37, no. 1, pp. 110–115, 2019.

[173] H. Li, G. Balamurugan, M. Sakib, J. Sun, J. Driscoll, R. Kumar, H. Jayatilleka, H. Rong, J. Jaussi, and B. Casper, "A 112 Gb/s PAM4 transmitter with silicon photonics microring modulator and CMOS driver," in *Optical Fiber Communications Conference and Exhibition*, 2019, p. Th4A.4.

[174] R. Dubé-Demers, J. St-Yves, A. Bois, Q. Zhong, M. Caverley, Y. Wang, L. Chrostowski, S. LaRochelle, D. V. Plant, and W. Shi, "Analytical modeling of silicon microring and microdisk modulators with electrical and optical dynamics," *Journal of Lightwave Technology*, vol. 33, no. 20, pp. 4240–4252, 2015.

[175] J. Sun, M. Sakib, J. Driscoll, R. Kumar, H. Jayatilleka, Y. Chetrit, and H. Rong, "A 128 Gb/s PAM4 silicon microring modulator," in *Optical Fiber Communications Conference and Exhibition*, 2018, pp. Th4A–7.

[176] R. Li, D. Patel, A. Samani, E. El-Fiky, Y. Wang, Z. Xing, L. Xu, and D. V. Plant, "Analysis and experimental study of a silicon photonic single MRM-assisted MZI PAM-4 modulator," *IEEE Photonics Journal*, vol. 9, no. 6, pp. 1–7, 2017.

[177] R. Li, D. Patel, E. El-Fiky, A. Samani, Z. Xing, M. Morsy-Osman, and D. V. Plant, "High-speed low-chirp PAM-4 transmission based on push-pull silicon photonic microring modulators," *Optics Express*, vol. 25, no. 12, pp. 13 222–13 229, 2017.

[178] P. Dong, R. Gatdula, K. Kim, J. H. Sinsky, A. Melikyan, Y.-K. Chen, G. De Valicourt, and J. Lee, "Simultaneous wavelength locking of microring modulator array with a single monitoring signal," *Optics Express*, vol. 25, no. 14, pp. 16 040–16 046, 2017.

[179] X. Zheng, E. Chang, P. Amberg, I. Shubin, J. Lexau, F. Liu, H. Thacker, S. S. Djordjevic, S. Lin, Y. Luo *et al.*, “A high-speed, tunable silicon photonic ring modulator integrated with ultra-efficient active wavelength control,” *Optics Express*, vol. 22, no. 10, pp. 12 628–12 633, 2014.

[180] K. Padmaraju, D. F. Logan, T. Shiraishi, J. J. Ackert, A. P. Knights, and K. Bergman, “Wavelength locking and thermally stabilizing microring resonators using dithering signals,” *Journal of Lightwave Technology*, vol. 32, no. 3, pp. 505–512, 2013.

[181] H.-C. Kim, K. Ikeda, and Y. Fainman, “Tunable transmission resonant filter and modulator with vertical gratings,” *Journal of Lightwave Technology*, vol. 25, no. 5, pp. 1147–1151, 2007.

[182] X. Wang, M. Caverley, J. Flueckiger, Y. Wang, N. A. F. Jaeger, and L. Chrostowski, “Silicon photonic Bragg grating modulators,” in *IEEE Photonics Conference*, 2014, pp. 190–191.

[183] A. Brimont, D. Thomson, P. Sanchis, J. Herrera, F. Gardes, J. Fedeli, G. Reed, and J. Martí, “High speed silicon electro-optical modulators enhanced via slow light propagation,” *Optics Express*, vol. 19, no. 21, pp. 20 876–20 885, 2011.

[184] A. Brimont, D. Thomson, F. Gardes, J. Fedeli, G. Reed, J. Martí, and P. Sanchis, “High-contrast 40 Gb/s operation of a 500 µm long silicon carrier-depletion slow wave modulator,” *Optics Letters*, vol. 37, no. 17, pp. 3504–3506, 2012.

[185] A. D. Simard and S. LaRochelle, “A dynamic model of silicon Bragg grating modulators,” *IEEE Journal of Selected Topics in Quantum Electronics*, vol. 22, no. 6, pp. 107–115, 2016.

[186] K. Bédard, A. D. Simard, B. Filion, Y. Painchaud, L. A. Rusch, and S. LaRochelle, “Dual phase-shift Bragg grating silicon photonic modulator operating up to 60 Gb/s,” *Optics Express*, vol. 24, no. 3, pp. 2413–2419, 2016.

[187] M. Caverley, X. Wang, K. Murray, N. A. F. Jaeger, and L. Chrostowski, “Silicon-on-insulator modulators using a quarter-wave phase-shifted Bragg grating,” *IEEE Photonics Technology Letters*, vol. 27, no. 22, pp. 2331–2334, 2015.

[188] S. LaRochelle and A. D. Simard, “Silicon photonic Bragg grating devices,” in *Optical Fiber Communications Conference and Exhibition*, 2017, pp. 1–3.

[189] C. Han, M. Jin, Y. Tao, B. Shen, H. Shu, and X. Wang, “Ultra-compact silicon modulator with 110 GHz bandwidth,” in *Optical Fiber Communications Conference and Exhibition*, 2022, pp. Th4C–5.

[190] O. Jafari, H. Sepehrian, W. Shi, and S. LaRochelle, “Silicon photonic modulator based on coupled Bragg grating resonators used as phase shifters,” in *Optical Fiber Communications Conference and Exhibition*, 2018, pp. Th2A–20.

[191] R. Hosseini, L. Mirzoyan, and K. Jamshidi, “Energy consumption enhancement of reverse-biased silicon-based Mach–Zehnder modulators using corrugated slow light waveguides,” *IEEE Photonics Journal*, vol. 10, no. 1, pp. 1–7, 2018.

[192] G. Cong, M. Ohno, Y. Maegami, M. Okano, R. Kou, N. Yamamoto, and K. Yamada, “Ultra-compact non-travelling-wave silicon Mach-Zehnder modulator,” in *European Conference on Optical Communication*, 2019, pp. 1–3.

[193] S. S. Azadeh, J. Nojić, A. Moscoso-Mártir, F. Merget, and J. Witzens, “Power-efficient lumped-element meandered silicon Mach-Zehnder modulators,” in *Silicon Photonics XV*, vol. 11285, 2020, pp. 65–75.

[194] S. Amiralizadeh, W. Lin, D. Patel, Y. Malinge, S. Burmeister, K. Al-hemyari, H. Yu, J. Park, C. Malouin, K. Li, P. Wen, X. Zheng, S. Gupta, R. Narayan, A. Liu, D. Zhu, B. Xie, Y. Akulova, S. Priyadarshi, C. Wang, and J. Hong, “System optimization of high-efficiency 400 Gb/s PAM4 silicon photonics transmitter for data center applications,” in *Optical Fiber Communications Conference and Exhibition*, 2021, p. M3A.4.

[195] W. Shi, Y. Xu, H. Sepehrian, S. LaRochelle, and L. A. Rusch, “Silicon photonic modulators for PAM transmissions,” *Journal of Optics*, vol. 20, no. 8, p. 083002, 2018.

[196] T. A. Ramadan and R. M. Osgood, “Adiabatic couplers: design rules and optimization,” *Journal of Lightwave Technology*, vol. 16, no. 2, p. 277, 1998.

[197] A. Milton and W. Burns, “Tapered velocity couplers for integrated optics: Design,” *Applied Optics*, vol. 14, no. 5, pp. 1207–1212, 1975.

[198] W. Louisell, “Analysis of the single tapered mode coupler,” *The Bell System Technical Journal*, vol. 34, no. 4, pp. 853–870, 1955.

[199] J. Flueckiger, *Enhancing the performance of silicon photonic biosensors.* PhD thesis, University of British Columbia, 2017.

[200] J. Zhou, H. Shen, R. Jia, H. Liu, Y. Tang, C. Yang, C. Xue, and X. Liu, “Uneven splitting-ratio 1×2 multimode interference splitters based on silicon wire waveguides,” *Chinese Optics Letters*, vol. 9, no. 8, pp. 082 303–082 303, 2011.

[201] J. D. Doménech, J. S. Fandino, B. Gargallo, and P. Munoz, "Arbitrary coupling ratio multimode interference couplers in silicon-on-insulator," *Journal of Lightwave Technology*, vol. 32, no. 14, pp. 2536–2543, 2014.

[202] K. Okamoto, *Fundamentals of optical waveguides.* Elsevier, 2021.

[203] K. Bergmann, H. Theuer, and B. Shore, "Coherent population transfer among quantum states of atoms and molecules," *Reviews of Modern Physics*, vol. 70, no. 3, p. 1003, 1998.

[204] J. Cho, B. Park, and Y. Jeong, "Thermal performance evaluation of a data center cooling system under fault conditions," *Energies*, vol. 12, no. 15, p. 2996, 2019.

[205] D. Patel, V. Veerasubramanian, S. Ghosh, A. Samani, Q. Zhong, and D. V. Plant, "High-speed compact silicon photonic Michelson interferometric modulator," *Optics Express*, vol. 22, no. 22, pp. 26 788–26 802, 2014.

[206] A. Novack, Y. Liu, R. Ding, M. Gould, T. Baehr-Jones, Q. Li, Y. Yang, Y. Ma, Y. Zhang, K. Padmaraju, K. Bergmen, A. E.-J. Lim, G.-Q. Lo, and M. Hochberg, "A 30 GHz silicon photonic platform," in *International Conference on Group IV Photonics*, 2013, pp. 7–8.

[207] M. S. Alam, X. Li, M. Jacques, Z. Xing, A. Samani, E. El-Fiky, P.-C. Koh, and D. V. Plant, "Net 220 Gbps/λ IM/DD transmission in O-band and C-band with silicon photonic traveling-wave MZM," *Journal of Lightwave Technology*, vol. 39, no. 13, pp. 4270–4278, 2021.

[208] M. Poulin, C. Latrasse, J.-F. Gagne, Y. Painchaud, M. Cyr, C. Paquet, M. Morsy-Osman, M. Chagnon, S. Lessard, and D. V. Plant, "107 Gb/s PAM-4 transmission over 10 km using a SiP series push-pull modulator at 1310 nm," in *European Conference on Optical Communication*, 2014, pp. 1–3.

[209] J. Armstrong, "OFDM for optical communications," *Journal of Lightwave Technology*, vol. 27, no. 3, pp. 189–204, 2009.

[210] M. Jacques, Z. Xing, A. Samani, E. El-Fiky, X. Li, M. Xiang, S. Lessard, and D. V. Plant, "240 Gbit/s silicon photonic Mach-Zehnder modulator enabled by two 2.3-Vpp drivers," *Journal of Lightwave Technology*, vol. 38, no. 11, pp. 2877–2885, 2020.